POLITECNICO
MILANO 1863

SCUOLA DI INGEGNERIA INDUSTRIALE
E DELL'INFORMAZIONE

Executive Summary of the Thesis

Erosion and migration properties of helium plasmas in linear machines: a coupled SOLPS-ITER and ERO2.0 investigation

Laurea Magistrale in Nuclear Engineering - Ingegneria Nucleare

Author: Paolo Carminati

Advisor: Prof. Matteo Passoni

Co-advisors: Ing. Gabriele Alberti, Ing. Elena Tonello

Academic year: 2020-2021

1. Introduction and aim of the work

In the next future, in order to achieve the production of energy by means of magnetically confined nuclear fusion in tokamaks, one of the fundamental aspects to understand and control is the plasma-wall interaction. The name of plasma-wall interaction refers to a very wide range of physical processes and consequently there are many areas of research that deal with specific aspects of this vast topic.
One of these is certainly the study of plasma exposures in fusion like conditions by using linear plasma machines. These machines allow to generate plasmas with characteristics similar to those of the future reactors. Thanks to their versatility, relative low costs and greater simplicity of design than tokamaks, they play a significant role in the experimental research of plasma-wall interaction. To study the interaction of materials with plasma, for example, it is possible to generate in linear machines thermonuclear fusion plasmas, then directed on samples of material whose behavior is to be tested. In particular, there is great interest in the research of materials such as tungsten, which can constitute the divertor of fusion reactors. [1]
Another direction of plasma-wall interaction research, which takes place in parallel with the experimental activity, is the coding activity. Each numerical code is written for the purposes of modeling the research field in which it is placed and each code has been developed with specific purposes and intentions. Each code has specific strengths but it is necessary to keep in mind the application limits. The application of numerical codes to the context of tokamaks is certainly the common approach in the literature, but recently the option of applying numerical codes for linear machine studies has also been evaluated. In fact, a method has recently been implemented for the application of the SOLPS-ITER plasma edge code, to the context of the simpler cylindrical geometry of the linear machine [5]. This adaptation made it possible to combine the coding activity of SOLPS-ITER with the experimental one also in the field of linear machines [4].
The motivations and aims of this thesis work arose in this framework. The final goal was to couple the SOLPS-ITER plasma edge code with the ERO2.0 code for the study of erosion and eroded impurities transport in the plasma, in the

context of helium plasmas in the GyM linear machine. We remark that a coupled simulation of this type in the context of linear plasma devices has not yet been published in the literature.
The reason for the choice of helium as the main species of plasma is certainly linked to the increasing use that is and will be made in the near future. Suffice it to say that all the first plasma discharges of ITER will be done with helium, for example. This is linked both to radio-protection reasons and to the simplifications it allows for the validation of plasma codes.

2. The methods

Two numerical codes have been used in this work, the first is SOLPS-ITER while the second is ERO2.0. SOLPS-ITER is the latest version of the SOLPS, or *scrape-off layer plasma simulator*, plasma edge code [6]. In the panorama of plasma edge codes it certainly stands as a point of reference. It consists of two parts, one that solves the multifluid equations for plasma particles, while the second is a *Monte Carlo* code for modeling both the transport of neutral atoms and molecular species and their reactions with plasma. This type of coupled approach is certainly one of the greatest strengths of the code.
The second code, ERO2.0, is also a code based on a Monte Carlo method. [3] The code allows to calculate the erosion due to plasma exposure of certain surfaces, to trace the eroded particles and to model both their trajectories and the interactions with the plasma. ERO2.0 is unable to calculate the background plasma. In order to function, the code relies on numerical codes capable of supplying this plasma data to the interfaces with solid walls.

3. Analyzing reactions and their contributions in the helium plasma

This work was divided into three steps. In the first, presented in *Chapter 3*, the standard reaction setup implemented by the Monte Carlo code part of SOLPS-ITER for helium plasmas was studied. Reaction setup is usually not modified by the user when using the code. During this work, however, it was done, because the default code implemented for helium only the reactions of interest to the tokamak context. In order to understand if this type of configuration was the most suitable choice for our application, some analyzes was carried out.
First of all, it was verified whether the choice of the database for the ionization of neutral particles by electrons reactions modeling, was sufficiently suitable for our purposes. In fact the code, for the calculation of the reaction rate, used data interpolated on the electronic temperature only. More up-to-date databases, on the other hand, make it possible to calculate the reaction rate also taking into account the effects of the density of the plasma species considered, in addition to the electronic temperature. Analyzing the results, it was found that the database chosen by default by the code returned results that differed from those provided by two most recent databases, which instead agree with each other.
In the second part of this step, other two things has been worked out, regarding the reactions to be included in the balance. Firstly, effects of the reactions that were *already implemented* by default by the code were analyzed, to understand if they made a significant contribution to the results. Then various reactions were identified which could be relevant in the operating conditions and which *had not been included yet* in the balance. The reactions that were investigated were elastic scattering, charge exchange and excitation of neutral atoms following ionization by electron impact.
For the elastic scattering reactions, it was found that they do not play a significant role in the balance because we are in a too low temperature situation. The charge exchange reactions instead play a significant role in determining the results. Charge exchange reactions between neutral and ion populations has the effect of activating a collisional drag for the ions and this has a particularly relevant effect on the plasma. So it is recommended to include this reaction in the balance. The effect of including in the balance the excitations of neutral atoms has also a significant repercussions on the behavior of the system: it activates an exchange of energy between the plasma populations and also this reaction must be included in the balance.
The results of this work were reported to the SOLPS-ITER developers and included in subsequent code updates.

4. The coupling: setup of the ERO2.0 simulation with SOLPS-ITER background plasma

In the second step, in *Chapter 4*, a job was done to convert the SOLPS-ITER data into the format readable by the ERO2.0 code. We used routines and scripts already used in the tokamak framework, then appropriately modified during this work for linear geometry. Particular attention was paid to all the inputs required by the second code, properly analyzed. Due to how the SOLPS-ITER and ERO2.0 meshes are constructed, in some points they overlap, while in other areas near the walls, the SOLPS-ITER mesh is narrower than that of ERO2.0. Consequently, particular attention has been paid to the method of extrapolation of the data between the SOLPS-ITER mesh and that of ERO2.0, because extrapolation can greatly affect the results, as can be seen for example in [2].
In the second part of this step, other issues concerning purely the ERO2.0 side has been addressed, in order to understand how to build a suitable setup for our *macroscopic* simulation. One of these aspect was to justify the choice of copper as the material with which to simulate the GyM chamber. A second issue was the identification of the most important parameters for the construction of a simulation with ERO2.0 that would satisfy our analysis needs.
In this sense was highlighted the importance of using a sufficiently refined mesh, on the internal surfaces of GyM which are of greatest interest for the study of phenomena such as erosion and deposition. The refinement of the mesh is also associated with a computational cost linked to the need to increase the number of test particles used by the Monte Carlo model on which the code is based. In our case, it was observed that the computational cost associated with refining the mesh was not a problem. The increase in computational time is not unreasonable in the face of the better quality of the result obtained. This result, however, required some strong assumptions, which have been appropriately dealt with in the rest of the chapter. Issues related to the number of computational time steps used in the simulation and to the representation statistics of the test particles had to be properly addressed.
The number of time steps is the parameter that most affects the maximum simulation time. In fact, the total computational time of the simulation can be roughly estimated as the time needed to perform a time step multiplied by the number of time steps chosen. By increasing the number of test particles, the time of the single time step increases, consequently it has an ever greater incidence on the total simulation time as the number of time steps chosen increases. In our work, the number of time steps has been set at one. It was verified that this choice had no influence on the simulation results, observing that even the first step alone allows the achievement of a situation of stationarity of the results.
Furthermore, the number of test particles chosen was verified to be sufficient to guarantee a good statistical representation of the real particles. An analysis was then carried out about which logics can be used by the code to optimize the statistical representation of the simulations even in situations of limited availability of test particles.

5. Coupled Simulation Analysis

In the third and last step, in *Chapter 5*, a first coupled simulation was carried out, with the aim of simulating a particular operating condition of the GyM linear machine, to study phenomena such as erosion and transport of eroded particles. The chosen operating condition of GyM was one sufficiently representative of the experimental activities that are carried out with the machine. After analyzing the results of the simulations on the plasma side, some aspects of the phenomena of erosion and transport of the eroded particles inside the linear machine were analyzed.
The total result of the analyzed helium reactions was observed. Up to now contributions had only been observed individually in the reaction setup preparation work. It was possible to analyze quantities as the heat and particle fluxes impinging on the internal surfaces of the GyM structure. Consequently, an estimate of the overall erosion was achieved and an analysis of the erosion pattern of the internal surfaces was made, starting from the bases of the GyM chamber. Finally, the behavior of the eroded impurities was observed. An estimate of the density

of the impurities in the areas of greatest concentration was given and the energy and incidence angle distributions at the impact of the eroded particles with the surfaces were analyzed.
A helium plasma in which charge exchange reactions were not included was also used as a sensitivity analysis. It has been observed how even small variations in electron temperature cause the erosion results obtained to vary significantly. This highlighted the importance of having a set of reactions that are as precise as possible.
With respect to this first part of the work, we can conclude that the presence of the phenomenon of erosion of the machine bases due to plasma has been highlighted and that the eroded particles give a negligible contribution of erosion. However, the simulation presents modeling limits due to the absence of steel erosion data and the conclusions that can be drawn from the results therefore have no absolute value.
Continuing with the work, some of the further modeling possibilities made available by the ERO2.0 code were explored. Among these, we explored the possibility of applying a bias potential to some internal surfaces of the structure, or when changing the material of which it is made. The materials used for comparison are carbon and tungsten, because materials connected in some way to the experimental activities that are carried out in the field of plasma-wall interaction research. Here too we analyzed the features of erosion and transport of eroded impurities.
It has been observed that the application of a bias potential has the effect of enhance the overall erosion of the surfaces to which it is applied. It increases the presence of impurities and lowers the degree of ionization. We hypothesize this is due to the fact that, being sputtered with greater energy, they redeposit faster, decreasing the probability of being ionized. The application of the bias potential also changes the energy distributions of the particles incident with the GyM structure. The effect of the varying bias is visible both on the energy distributions at the start, affecting the maximum energy they can reach, and on arrival, suitably shifting and creating peaks.
On the materials side, it was then observed how the different properties of the materials affected the results. The ionization energy thresholds, together with the mass of the atom which constitutes the material of the structure of the GyM chamber, determine in an important way the behavior of the eroded particles. In the case of carbon, the greater ionization energy is reflected in the greater presence of neutral charge states. In the case of tungsten, the presence of ionized charge states following the magnetic field lines is observed. Comparisons were made between the different situations, looking at these issues from different perspectives.
Finally, to conclude the work, we addressed the issue of understanding how much the different extrapolation methods, of the plasma data coming from SOLPS-ITER, influenced the results of the simulations made with ERO2.0. A different helium plasma from the one used in the previous coupling was constructed with SOLPS-ITER, more restricted, so that the extrapolated area was larger than in the previous case. This choice was made not only in the service of its usefulness at the computational level, but also because it has a certain relevance from the physical point of view. In fact it also represents another way to approach the SOLPS-ITER simulations when there are protrusions entering the plasma. By coupling the SOLPS-ITER data once again with the ERO2.0 code, it was possible to observe how the variation of the extrapolation model affected the boundary conditions of the problem. In our case, however, the effect of the variation of the extrapolation model did not produce appreciable results in terms of erosion in our chosen operating condition. This is due to the fact that the temperature variations due to the variation of the extrapolation pattern are too small to cause a variation of the erosion, even if we said it is a very sensitive phenomena. The evaluation of this parameter was made in the most sensitive case observed, namely that of carbon. This ensures that even if we changed the extrapolation model in the case of copper or tungsten, even here there would be no appreciable impact on the results.

6. Perspectives

In light of these results future developments with respect to this work can go in different directions:

- Understand a strategy to generate databases of materials such as stainless steel with ERO2.0, which can represent

materials more used in constructing linear machines.

- Understand from both the modelling and the experimental point of view which is the best approach if we want to include in the simulations with SOLPS-ITER three-dimensional objects such as the protrusions that enter the plasma and disturb its behavior.
- Understand how much the presence of eroded impurities can modify the background plasma, both from an experimental and modeling point of view.
- Achieve the simulation of the presence of a sample holder inside the GyM chamber. The presence of the sample holder is certainly a disturbing element for the plasma, as well as the particles eroded by the walls or the structure of the sample holder. It would be interesting to evaluate the influence that the particles eroded from the chamber walls have on the plasma-surface interaction experiments.

References

[1] Gabriele Alberti. Exposure of nanostructured tungsten coatings to helium-plasmas in the gym linear device. Master's thesis, Politecncico di Milano, Milano, 2019.

[2] J Romazanov, S Brezinsek, RA Pitts, A Kirschner, A Eksaeva, D Borodin, E Veshchev, VS Neverov, AB Kukushkin, AG Alekseev, et al. A sensitivity analysis of numerical predictions for beryllium erosion and migration in iter. *Nuclear Materials and Energy*, 26:100904, 2021.

[3] Juri Romazanov. *3D simulation of impurity transport in a fusion edge plasma using a massively parallel Monte-Carlo code*. Number FZJ-2019-01018. Plasmaphysik, 2018.

[4] Michele Sala, Elena Tonello, Andrea Uccello, Xavier Bonnin, Daria Ricci, David Dellasega, Gustavo Granucci, and Matteo Passoni. Simulations of argon plasmas in the linear plasma device gym with the solps-iter code. *Plasma Physics and Controlled Fusion*, 62(5):055005, 2020.

[5] Elena Tonello. Numerical investigation of nuclear fusion relevant plasmas in linear devices through the solps-iter code. Master's thesis, Politecncico di Milano, Milano, 2018.

[6] S. Wiesen, D. Reiter, V. Kotov, M. Baelmans, W. Dekeyser, A.S. Kukushkin, S.W. Lisgo, R.A. Pitts, V. Rozhansky, G. Saibene, I. Veselova, and S. Voskoboynikov. The new solps-iter code package. *Journal of Nuclear Materials*, 463:480–484, 2015. PLASMA-SURFACE INTERACTIONS 21.

POLITECNICO DI MILANO
Department of Energy - CeSNEF
M.Sc. in Nuclear Engineering

Erosion and migration properties of helium plasmas in linear machines: a coupled SOLPS-ITER and ERO2.0 investigation

Supervisor
Prof. Matteo Passoni

Co-Advisors
Ing. Elena Tonello
Ing. Gabriele Alberti

Candidate
Paolo Carminati
Matr. 906004

Academic year 2020-2021

Contents

Contents iii

1 Nuclear Fusion 1
- 1.1 Nuclear Energy: a safe and clean solution . . . 1
  - 1.1.1 Fission and Fusion: two different approaches . . . 3
- 1.2 Fusion Physics and Principles . . . 5
  - 1.2.1 Fusion reactions . . . 5
  - 1.2.2 Plasma: the 4^{th} state of matter to exploit fusion . . . 6
  - 1.2.3 Energy balances in the system . . . 8
  - 1.2.4 Lawson criterion . . . 9
  - 1.2.5 Burning plasma and criticality condition . . . 9
  - 1.2.6 Through the construction of a fusion machine: engineering figure of merit and the blanket . . . 10
  - 1.2.7 Confinement approaches: inertial and magnetic confined fusion . . . 12
- 1.3 Magnetically Confined Nuclear Fusion . . . 13
  - 1.3.1 Motion of a charged particle due to an external magnetic field . . . 14
  - 1.3.2 Magnetic configurations to confine the plasma: tokamak and stellarator . . . 16
  - 1.3.3 An example of tokamak: ITER . . . 18
  - 1.3.4 An unavoidable touch: limiters and divertors . . . 19
  - 1.3.5 One piece of the puzzle: the importance of managing the plasma surface interaction and the role of linear plasma devices . . . 20
- 1.4 An example of a linear plasma device: GyM . . . 21
  - 1.4.1 Magnetic field configuration and diagnostics in GyM . . . 22
  - 1.4.2 Plasma generation: the radiofrequency source . . . 22

2 Plasma-Wall Interaction and Impurity Transport 24
- 2.1 Relevant physics in the scrape-off layer . . . 24
  - 2.1.1 Formation of the plasma sheath . . . 25
  - 2.1.2 Interaction of atomic species in edge plasma . . . 27
  - 2.1.3 Sputtering and erosion . . . 28
  - 2.1.4 Transport and re-deposition . . . 29
- 2.2 Modelling the plasma edge with SOLPS-ITER . . . 29
  - 2.2.1 Kinetic models for plasma . . . 30
  - 2.2.2 Fluid models for plasma . . . 32
  - 2.2.3 SOLPS-ITER: structure of the code . . . 35
  - 2.2.4 Inputs and workflow of the code . . . 36
  - 2.2.5 Rate coefficients and databases . . . 38
- 2.3 Modelling the plasma-wall interaction and impurity transport with ERO2.0 . . . 39
  - 2.3.1 Erosion . . . 40
  - 2.3.2 Impurity transport . . . 41
  - 2.3.3 ERO2.0: inputs and workflow of the code . . . 43
- 2.4 Overview on the reference literature context . . . 43
  - 2.4.1 Experimental investigations of plasma edge physics and plasma-wall interaction . . . 44
  - 2.4.2 Modelling activities related to the experimental ones . . . 44
- 2.5 Motivations and aim of the work . . . 46

3 Analyzing helium plasma reactions and their contributions with SOLPS-ITER 47
- 3.1 Adapting SOLPS-ITER to the linear plasma device GyM . . . 47
  - 3.1.1 Coordinate systems . . . 47
  - 3.1.2 Building 2D meshes from the magnetic field . . . 48

3.1.3 Setting up the configuration with DivGeo . . . 49
3.1.4 Limits of the standard setup and the need to improve helium reactions . . . 50
3.2 Updating the choice of the databases . . . 51
3.3 Analyzing the reactions and their contributions . . . 53
3.3.1 The effect of elastic collisions . . . 54
3.3.2 The effect of charge exchange . . . 55
3.3.3 Including neutral excitations in the electron impact ionization process . . . 57
3.4 Summary . . . 60

4 The coupling: set up of the ERO2.0 simulation with SOLPS-ITER background plasma 62
4.1 Converting SOLPS-ITER outputs into ERO2.0 inputs . . . 62
4.1.1 Workflow of the procedure . . . 62
4.1.2 Required SOLPS-ITER outputs . . . 63
4.1.3 Interpolating and extrapolating the data with MATLAB routines . . . 64
4.1.4 Running heroin and ERO2.0 inputs . . . 65
4.2 Set up of the global simulation of GyM with ERO2.0 . . . 66
4.2.1 The choice of copper as the wall material . . . 66
4.2.2 Building 3D geometry and mesh refining . . . 66
4.2.3 Presence of other impurities: including the Cu^{2+} . . . 69
4.2.4 Time evolution: reaching the equilibrium . . . 70
4.2.5 Statistics optimization strategies with refined mesh . . . 70
4.2.6 Wall reflections and analytical sheath tracing models . . . 72
4.3 Summary . . . 72

5 Coupled Simulations Analysis 73
5.1 Helium plasma on a GyM made of copper . . . 73
5.1.1 Data on the helium plasma in working conditions . . . 73
5.1.2 Plasma fluxes and temperatures on the surfaces . . . 75
5.1.3 Erosion analysis of helium plasma on copper . . . 77
5.1.4 Impurity transport: trajectories, densities and redeposition . . . 78
5.1.5 Impacts of the impurities with the wall: energy and angle distributions . . . 79
5.1.6 Sensitivity analysis neglecting charge exchange reactions . . . 80
5.2 Enhancing the erosion: applying the bias to the surfaces . . . 81
5.2.1 Erosion analysis: beyond thresholds on basis and bushings . . . 81
5.2.2 Decreasing ionizations . . . 82
5.2.3 Effects on the incident angle distribution of the impurities . . . 83
5.2.4 Effects on energy distributions of the impurities . . . 84
5.3 Changing the material of the chamber: tungsten and carbon . . . 85
5.3.1 Motivations to the choice of the two materials and some relevant physical quantities . . . 85
5.3.2 Global erosion analysis: inspecting thresholds and presence of charged particles . . . 86
5.3.3 Erosion angle pattern: the case of the bushings . . . 87
5.3.4 Erosion and deposition fractions of the impurities . . . 88
5.3.5 Plasma-wall collisions: broadening energy peaks of the impurity energy distributions 89
5.3.6 Angle distributions of the impurities: bending the charged particles increasing the bias 90
5.4 Restricting the plasma: varying the extrapolation . . . 90
5.4.1 Comparison with extended case: radial profiles of relevant physical quantities . . . 91
5.4.2 Effects of the extrapolation on the results in the most sensitive case: carbon . . . 92
5.5 Limits of this modelling . . . 93
5.6 Summary . . . 94

6 Conclusions and Perspectives 96

Appendix 99

Bibliography 100

List of Figures

1.1 Global primary energy consumption by source in TWh . . . 2
1.2 List of the safest and cleanest power production technologies . . . 4
1.3 Binding energy per nucleon as the mass number A varies . . . 4
1.4 Nuclear fission cross sections for the fissile ^{235}U and the ^{239}Pu . . . 5
1.5 Nuclear fusion cross sections . . . 6
1.6 $\langle\sigma(v)v\rangle$ for some fusion reactions . . . 7
1.7 Schematic diagram of a fusion power station . . . 11
1.8 Example of a fuel pellet for Inertial Confinement Fusion . . . 13
1.9 Direct and Indirect drive schemes . . . 13
1.10 The mirror machine: an example of linear geometry . . . 15
1.11 An example of toroidal configuration for plasma confinement. . . . 15
1.12 The mirror effect . . . 15
1.13 Outward pressure expansion force in both linear and toroidal configurations . . . 16
1.14 Outward force due to toroidicity . . . 16
1.15 Qualitative picture of the hoop force . . . 16
1.18 Coils' scheme in a tokamak . . . 17
1.16 Qualitative picture of the tire tube force . . . 17
1.17 Qualitative picture of the 1/R force . . . 17
1.19 Scheme representation of the stellarator Weldstein 7-X . . . 17
1.20 Construction scheme of ITER . . . 19
1.21 Qualitative schemes of the limiter and the divertor configurations . . . 19
1.22 Constructive design of the ITER divertor . . . 20
1.23 Schematic drawing of GyM linear machine with the magnetic field coils and the vacuum chamber. 21
1.24 Contour lines of the stream-function ψ for GyM standard coil configuration at 600 A . . . 22
1.25 ECR location for different values of B . . . 23
2.1 The SOL the region . . . 24

2.2 Summary of the most relevant physical processes in the plasma-wall interaction . . . 25
2.3 Schematic of the variation in 1D of plasma pressure, electric potential, plasma velocity and ion/electron densities in the plasma between two semi-infinite planes . . . 25
2.4 SOLPS-ITER workflow . . . 37
2.5 Definition of the projectile incidence angle θ_{in} relative to the surface normal $\vec{n}$ . . . 40
2.6 Example of workflow: illustration of the general workflow of the ERO2.0 code . . . 43
3.1 Illustration of the dynamical and geometrical reference frame in toroidal geometry . . . 47
3.2 Example of the construction of the mesh in a poloidal section in the geometrical reference frame . 47

3.3 Example of the construction of the mesh in the geometrical reference frame in GyM . . . 48
3.4 Generated 64x12 SOLPS-ITER mesh used in this work . . . 49
3.5 Mean volume temperature and density plots, database comparison . . . 51
3.6 Heat fluxes at the West target, database comparison . . . 51
3.7 Ion particle flux at the West target, database comparison . . . 51
3.9 Neutral He density 2D contour plot: the effect of the choice of the database . . . 52
3.10 Ion He^{+} density 2D contour plot: the effect of the choice of the database . . . 52
3.11 Ion He^{2+} density 2D contour plot: the effect of the choice of the database . . . 52
3.8 Rate coefficients from ADAS and HYDHEL databases . . . 52
3.12 Mean volume temperature and density plots, elastic scattering effect . . . 54

3.13 Heat fluxes at the West target, elastic scattering effect . . . 54
3.14 Ion particle flux at the West target . . . 54
3.15 Neutral He density 2D contour plot: the effect of elastic scattering . . . 55
3.16 Mean volume temperature and density plots, effect of charge exchange . . . 56
3.17 Heat fluxes at the West target, effect of charge exchange . . . 56
3.18 Ion particle flux at the West target, effect of charge exchange . . . 56
3.19 Neutral He density and temperature 2D contour plot. Effect of the charge exchange . . . 56
3.20 He^+ and He^{2+} density 2D contour plots. Effect of the charge exchange . . . 57
3.21 Total radiation from neutrals . . . 59
3.22 Electron temperature 2D contour plot, effect of neutral excitation. . . . 59
3.23 Mean volume temperature and density plots, effect of neutral excitation . . . 59
3.26 He^+ density 2D contour plot, effect of neutral excitation . . . 60
3.27 He^{2+} density 2D contour plot, effect of neutral excitation . . . 60
3.24 Heat fluxes at the West target, effect of neutral excitation . . . 60
3.25 Ion particle flux at the West target, effect of neutral excitation . . . 61

4.1 Workflow of the converting procedure . . . 63
4.2 Energy dependence of the sputtering yield of Cu with ^{4}He ions . . . 67
4.4 Representation of the mesh constructed for GyM bases . . . 67
4.5 Representation of the mesh constructed for GyM lateral wall, part I . . . 67
4.6 Representation of the mesh constructed for GyM lateral wall, part II . . . 67
4.3 Section of the GyM's internal surfaces, simplified for modelling . . . 67
4.7 Representation of the mesh constructed for GyM internal bushings . . . 68
4.8 Total erosion rate of the bases . . . 68
4.9 Total erosion rate of the bushings . . . 68
4.10 Plasma ion particle flux impinging on the bushings . . . 69
4.11 Representation of the refined mesh for GyM bases . . . 69
4.12 Representation of the refined mesh for GyM internal bushings . . . 69
5.1 Mean volume temperature and density plots . . . 73

5.2 Radial profiles of the electron and ion temperatures . . . 74
5.3 Neutral He, electron e^-, He^+ and He^{2+} density 2D contour plots . . . 74
5.4 Electron e^-, He^+ and He^{2+} temperature 2D contour plots . . . 74
5.5 Ion particle flux density ($\#atm m^2 s^{-1}$) on the reference mesh . . . 75
5.6 Ion particle flux *flux* n_i at the West target and at the East target . . . 76
5.7 Thermal energy fluxes at the West and East targets . . . 76
5.8 Electron thermal energy flux density at the GyM bases . . . 76
5.9 Ion particle flux density and electron temperature on the GyM bases . . . 77
5.11 Comparison between erosion rate due to plasma and due to self-sputtering . . . 77
5.10 Ion particle flux density and electron temperature on the bushings . . . 77
5.12 Erosion rate on GyM lateral walls . . . 78
5.13 Erosion rate on GyM bases and bushings . . . 78
5.14 Neutral Cu, Cu^+ and Cu^{2+} density 2D contour plots . . . 79
5.15 3D trajectories of some of the traced impurities . . . 79
5.17 Deposition rate of the impurities on GyM bases and bushings . . . 79
5.18 Angle and energy distributions of the impurities . . . 80
5.16 Deposition rate of the impurities on GyM lateral walls . . . 80
5.19 Erosion rate on GyM bases and bushings, sensitivity analysis neglecting the charge exchanges . . . 81
5.20 Erosion rate on GyM bases, effects of the increasing bias . . . 82
5.21 Incidence angle distributions, effect of varying the bias . . . 83
5.22 Energy distribution of the incident impurity particles, applied bias to bases and bushing of $100V$ 84

5.23 Energy distribution of the impurity particles at the release from GyM internal structure 84
5.24 Carbon and tungsten Eckstein sputtering yield 86
5.25 Erosion rate on GyM bases and bushings using carbon as structure material 86
5.26 Angle pattern of the erosion rate due to plasma on GyM bushings, comparison among the three different materials 87
5.27 Erosion fraction, surfaces comparison. Comparison among the three material varying the bias . . 88
5.28 Re-deposition fraction, surfaces comparison. Comparison among the three material varying the bias 88
5.29 Energy distribution of the incident impurity particles with GyM internal structure. Comparison among the three materials 89
5.30 Incidence angle distribution of the impurity particles at the impact with GyM internal structure. Comparison among the two materials 90
5.31 Radial profiles of the electron and ion temperatures, comparison between restricted and extended plasmas 92
5.32 Electron temperature on the GyM bases, comparison among four different extrapolations 93
5.33 Erosion rate on GyM bases using carbon as structure material and the restricted plasma 93

List of Tables

1.1 Comparison of power densities between the most used today different energy production technologies 3
1.2 Total cost of electrical energy production in € cents per kWh 3
1.3 σ_m and relative T_m of the fusion reactions 6
1.4 Examples of Q and Q_{eng} when typical values of η_e of current fusion approaches are adopted . . . 11
1.5 Main parameters of GyM. 21

3.1 Summary of the main input parameters set in the DivGeo program 49
3.2 Summary of the reactions implemented in run 0.S, run 1.S and run 2. 51
3.3 Summary of the charge exchange simulations 55
3.4 Summary of the electron ionization simulations 58

4.1 Summary of the computational cost of the simulations, adding elements to the 3D mesh 68
4.2 Summary of the setup using the refined mesh 69
4.3 Summary of the statistics with refined mesh 70
4.4 Summary of the statistic optimization results 71

5.1 Contribution of self-sputtering and plasma sputtering to the total erosion rates, effect of the bias . 82
5.2 Population fractions, effect of the application of the bias 83
5.3 Population fractions of the particles, for different materials with applied bias to bases and bushings of $200V$ 87

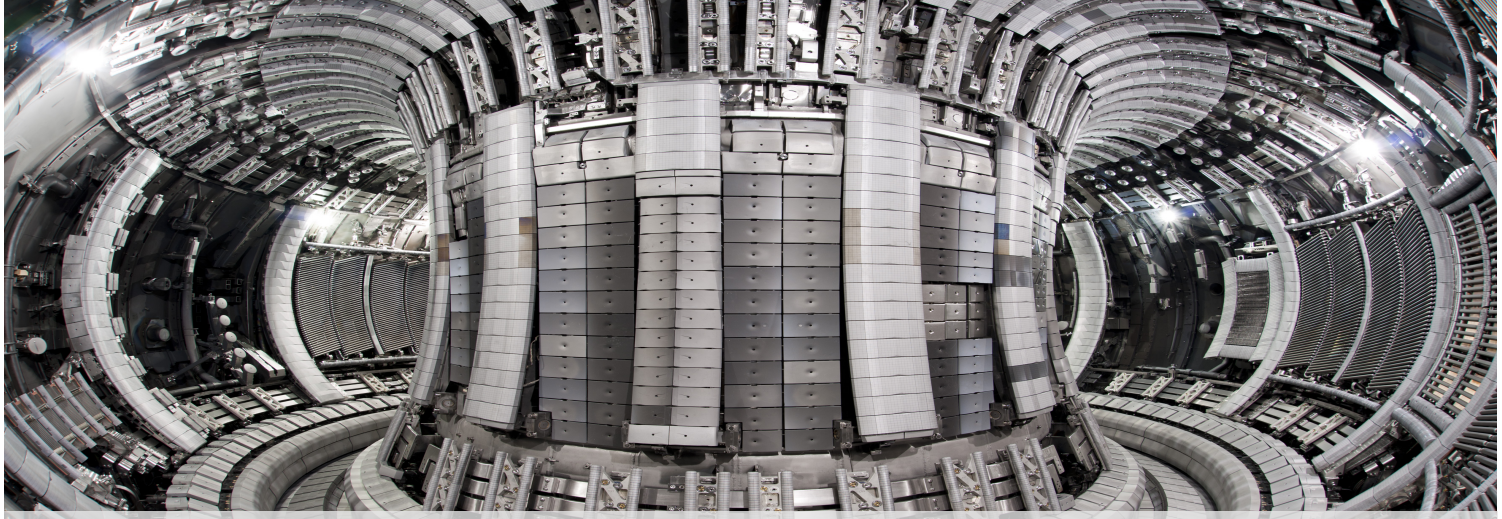

1 Nuclear Fusion

In this chapter thermonuclear fusion as a source of energy is presented. In Section 1.1 the nuclear solution to the problem of the growing demand for energy in the world is presented, together with the two main approaches to extract energy from atoms: fission and fusion. In Section 1.2 a more detailed overview on thermonuclear fusion is given. The first part of Section 1.3 is dedicated to the most promising of the methods of producing energy through nuclear fusion: fusion by means of a magnetically confined plasma; the second part is focused on the role of linear plasma devices (*LPDs*) in the context of plasma-wall interaction research (*PWI*). Finally, in Section 1.4, the linear plasma device designed and built by ISTP (Istituto per la Scienza e Tecnologia dei Plasmi) - CNR (Centro Nazionale delle Ricerche) in Milan which is the object of the analysis carried out in this work: the Gyrotron Machine (*GyM*).

1.1 Nuclear Energy: a safe and clean solution 1
1.2 Fusion Physics and Principles 5
1.3 Magnetically Confined Nuclear Fusion 13
1.4 An example of a linear plasma device: GyM 21

1.1 Nuclear Energy: a safe and clean solution

The increasing trend of energy consumption by human activities on a global scale over the years is a fact, and, in order to quantify this phenomenon, the global primary energy consumption by source is reported in Figure 1.1. In this study [1] primary energy is calculated based on the *substitution method*, which takes account of the inefficiencies in fossil fuel production by converting non-fossil energy into the energy inputs required if they had the same conversion losses as fossil fuels. From the graph it can be observed that the trend is tremendously increased in the last 50 years so that the growth in energy demand has almost doubled in the last 25 years.

Energy consumption and human activities are strongly related: on the one hand the availability of energy constitutes a very important resource for people's lives; on the other hand it is equally important that it is produced in such a way as not to cause long-term damages, even more deleterious than the unavailability of power. Therefore, a completely natural consequence of this consideration is that finding a clean, safe, cheap and sustainable energy source for human activities is one of the most challenging problems for mankind today.

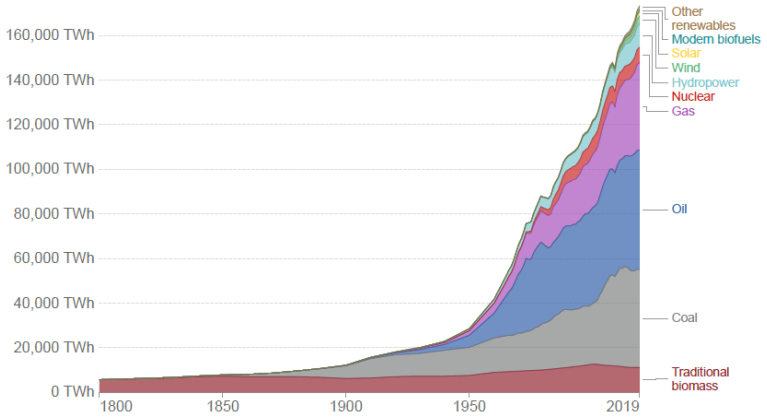

Figure 1.1: Global primary energy consumption by source in TWh: primary energy is calculated based on the 'substitution method' which takes account of the inefficiencies in fossil fuel production by converting non-fossil energy into the energy inputs required if they had the same conversion losses as fossil fuels. *Source: Vaclav Smil (2017) & BP Statistical Review of World Energy*

Looking at the graph it can be observed that coal and oil contribute to more than 50% of the global energy requirement and this energy mix has remained almost unchanged along years, and no policy has been implemented to replace technology with something more environmentally sustainable. In this direction, despite political divergences, there is a solid scientific basis to support that nuclear energy can represent a reliable technology to overcome traditional non-renewable energy sources like coal, oil, gas and traditional biomass. Fossil fuels, relying on the combustion of organic material, are the major cause of production of CO_2, nitrogen and sulfur oxides in the atmosphere, which has been identified as one of the most important causes of the ozone hole, global warming and greenhouse effect [2]. Nuclear energy is not based on combustion, is almost CO_2-free in the whole production chain [3] and it does not represent a source of atmospheric pollution, something that cannot be said of former technologies.

A second peculiar advantage of exploiting nuclear energy is its enormous intrinsic power density of the fuel with respect to other sources. As an example, in traditional chemical combustion processes the energy produced per event of combustion of the molecules involved in the process is of the order of their binding energy and has a magnitude of few eV. The energy extraction methodologies of nuclear technologies are based on nuclear reactions, which are of the order of tens of MeV per single reaction. This leads to one of the most appealing advantages of nuclear, namely the possibility of consuming less fuel for the same amount of power.

A third advantage which derives from the consideration just made is on the plant itself. Three important factor have to be considered: the lifetime of the plant, the power density and the cost of the kWh. It is clear that the desired condition is longer operational life of the plant, a denser energy production, lower costs of the plant and the best use of resources.

Regarding the lifetime of the plant, nuclear power plants are designed to have a life of at least 40 years, the high safety margins adopted have also allowed them to operate for another 10, 20 and 40 years. Gas plants see turbines change every few months or at most a year because they are used in extreme conditions (temperature and cycles to follow the grid load), coal plants have an expected life of 30 years, as well as solar panels and wind farms.

Regarding power densities, we look at the following (Table 1.1) taken from [4].

Energy Density		
Technology	Power [MWe]	Surface [km^2]
Nuclear	3000	1.5
Gas	3000	1.5
Oil	3000	3
Coal	3000	3
Water power	1000	a few
Solar	1000	20-50
Wind	1000	50-100
Biomass plantation	1000	4000

Table 1.1: Comparison of power densities between the most used today different energy production technologies: nuclear, gas, oil, coal, water power, solar, wind and biomass plantation.

From this table it is evident that nuclear plants, together with gas ones, have the highest power densities.The lower the power density, the greater the quantity of materials to be repaired, dismantled and recycled at the end of their life (if possible, for example the blades of wind turbines are made of non-recyclable composite materials).

Regarding the costs of the energy, Table 1.2 taken from [5] shows the costs of the kWh produced with the different technologies. Also in this table, it can be observed that nuclear power it is competitive with other power production technologies also from the cost point of view.

Energy Cost in € cents per kWh			
	Operation, amortization and financial costs	External costs*	Total
Coal	5.0	2.0	7.0
Oil	4.5	1.6	6.0
Natural Gas	3.5	0.36	3.9
Wind	6.0	0.22	6.2
Hydroelectric	4.5	0.22	4.7
Nuclear	3.5	0.04	3.5

Table 1.2: Total cost of electrical energy production in € cents per kWh
*15€/tonn CO_2.

Finally, once cleared that nuclear energy is one of the best options in terms of the plant optimization, the last and most important topic is faced: safety. In order to compare the technologies and to make a summary from a safety and cleanliness point of view, Figure 1.2 taken from [1], is reported, which shows once again that nuclear power generation is one of the safest and cleanest sources of energy we have nowadays.

1.1.1 Fission and Fusion: two different approaches

As mentioned above, the extraction of energy from matter by means of nuclear technologies is done not by working with the chemical bonds that exist between molecules but by exploring inter-atomic reactions. When a reaction among two atoms like this:

$$a + b \longrightarrow c + d$$

is exploited, and if rest mass is conserved and also kinetic energies, the only way to extract energy from the system is to vary its *binding energy* in

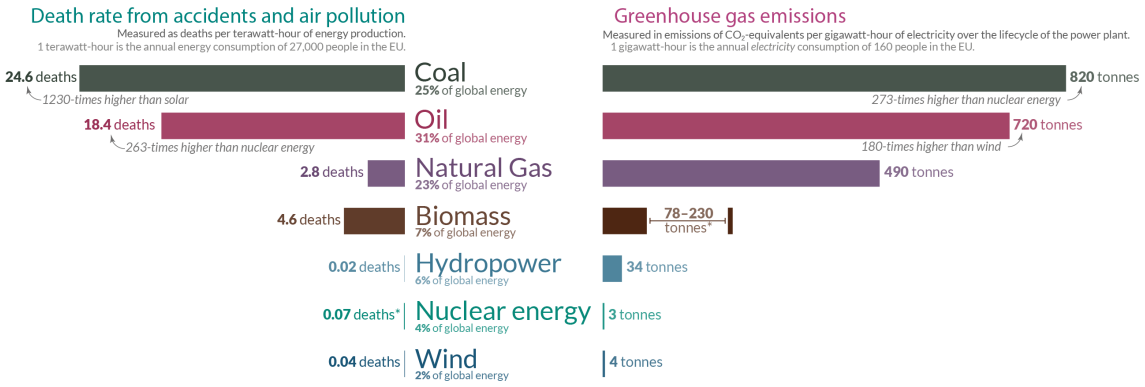

Figure 1.2: List of the safest and cleanest power production technologies.
* Life-cycle emissions from biomass vary significantly depending on fuel and the treatment of biogenic sources. The death rate for nuclear energy includes Fukushima and Chernobyl disasters as well as the death from occupational accidents (largely mining and milling).
Sources: Death rates from Markandaya & Wilkinson (2007) in The Lancet, and Sovacool et al. (2006) in Journal of Cleaner Production; Greenhouse gas emission factors from IPCC AR5 (2014) and Pehl et al. (2017) in Nature; Energy shares from BP (2019) and Smil (2017).

order to have a positive difference between the products and the reagents. This is because binding energy acts as the inverse of a potential energy: if the system, for some reason (nuclear physics arguments are needed in order to understand this) can exist, in a bounded state with a less energy effort, the binding energy increases. So, if in some way we can produce an increase in the binding energy of the system, we can extract energy from that nuclear reaction.

Now, looking at the following graph in Figure 1.3, which shows the binding energy per nucleon as the atomic number A varies, it can be seen that it presents a maximum of about $9MeV$ in correspondence of $A = 60$. This value therefore represents the situation where nucleons are more efficiently cohesive than smaller or larger atomic numbers.

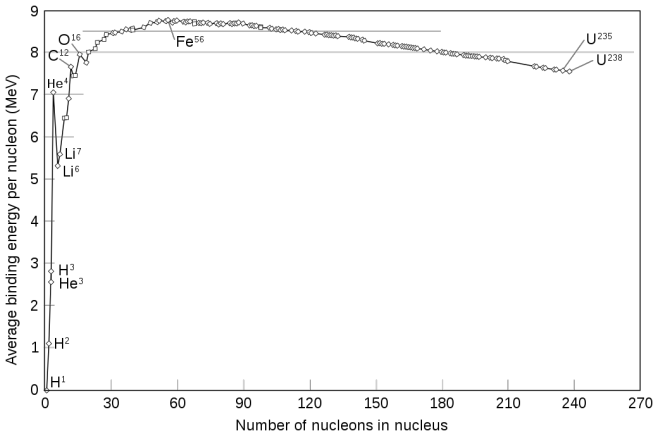

Figure 1.3: Binding energy per nucleon as the mass number A varies.

At this point, understanding the principle underlying all nuclear power plants is very simple: all atomic reactions that somehow transform nuclei that are not at the maximum point into nuclei closer to it, will be exothermic reactions. Looking at the Figure 1.3 and following this reasoning, it can be seen that the most efficient reactions are those of division of nuclei of heavy atoms or union of nuclei of light atoms. These two methods are known as *thermonuclear fission* and *fusion*.

Let us now briefly analyze nuclear fission main feature, while nuclear fusion will be analyzed in more detail in the next Section 1.2. Nuclear fission has been the first method exploited. On December 2^{nd}, 1942, a group of scientists, led by Enrico Fermi, began and kept under control a nuclear chain reaction within an atomic pile formed by graphite and uranium (metal and oxide). In the experimental facility CP-1 (Chicago Pile No.1), a controlled fission chain reaction of uranium-235 nuclei based on slowed-down neutrons was obtained and it was sustained for approximately 28 minutes.

Up to now, all the commercial electrical power produced by nuclear reactions has been obtained exploiting the fission induced by neutrons of heavy elements, mainly uranium.

Let us consider also the *cross section* of the fission reaction, a very important quantity in nuclear physics because, in the framework of nuclear reactions, it represents the probability with which a given reaction can occur. The fission cross section for ^{235}U and ^{239}Pu as a function of neutron energy is reported in Figure 1.4. We can clearly see the $\approx \frac{1}{v}$ behaviour of the cross section in the thermal energy region, below $0.1eV$ and the resonant behaviour for higher neutron energies. Nowadays there are two types of technology available: one that exploits the higher cross section value at low energy of the incident neutrons, which are called *thermal neutrons*, and the other that exploits fission resonance peaks at higher energies of the incident (*fast*) neutrons: these two technologies are referred to as *thermal reactors* and *fast reactors*.

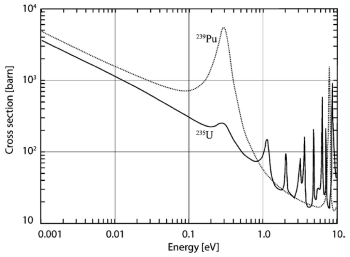

Figure 1.4: Nuclear fission cross sections for the fissile ^{235}U and the ^{239}Pu.

The key feature of nuclear fission reactor is the possibility of self-sustain a chain reaction, so that no external power supply is needed once the reaction has been started. This is possible providing a balance among the neutrons needed to fission a given mass of fuel, the neutrons produced by the fission reactions and the neutron losses, both from absorption and leakage from the reactor. Once this balance is reached, the reactor is said to be *critical*, the produced power is stationary and no external energy source is needed.

1.2 Fusion Physics and Principles

Let us now explore the second possibility of extracting energy by means of nuclear technology: the nuclear fusion. We start presenting the physics of the reaction.

1.2.1 Fusion reactions

Returning to Figure 1.3, if on the one side we try to divide a heavy nucleus, on the other side we try to fuse two light nuclei to obtain another in the direction of maximizing the binding energy. In this sense ^4He is very interesting because, compared to neighboring nuclei with similar mass numbers, it has a much higher binding energy. Here we have three interesting fusion reactions, the most energetic produce in fact ^4He:

$$D + D \longrightarrow T + {}^{1}H + 4.03\,MeV \qquad b.r.\ 0.5 \qquad (1.1a)$$
$$D + D \longrightarrow {}^{3}He + n + 3.27\,MeV \qquad b.r.\ 0.5 \qquad (1.1b)$$

$$D + {}^{3}He \longrightarrow {}^{4}He + {}^{1}H + 18.3\,MeV \qquad (1.2)$$

$$D + T \longrightarrow {}^{4}He + n + 17.6\,MeV \qquad (1.3)$$

There are many fusion reactions that we could consider, but only a few are interesting because the higher Q-value does not mean that the reaction is easily achievable: the cross section must be considered. A typical analytical trend for the fusion cross section is given by the Breit Wigner formula (1.4):

$$\sigma(E) = \frac{1}{E} S(E) e^{-(G_E/E)^{\frac{1}{2}}} \qquad (1.4)$$

Where $S(E)$ is the so-called astrophysical S-factor and, for most of the reaction of interest, is slowly varying with E, while G_E is the Gamow energy and it is proportional to the square of the nuclear charges. The Gamow factor is representative of the need to overcame the potential barrier given by the Coulomb repulsive force that exists between two nuclei charged with the same sign by tunneling effect. The energy must be high enough that the particles can approach and feel the attractive effect of the strong interaction between nucleons.

In fission there is no potential energy barrier that must be overcome, so the reaction is easily self-sustained by the neutrons produced. In this case it is different because there is nothing among the products that can be reused to catalyze subsequent reactions. The conditions to overcome the Coulomb barrier must always be satisfied, or in any case for a period of time long enough to allow the production of electricity.

Let us now see in Figure 1.5 the cross sections for the reactions listed above, just below the values in Table 1.3 of the maximum cross-section σ_m for the reaction at the temperature T_m are reported.

D-T is the most interesting for our purposes, attractive both for large cross section and for the Q-value. Moreover, compared to the (1.2), the charges of the same sign to approach are only two. But now a question arises: in what condition must the reactants be kept in order for them to come together to merge? The answer is given by the fourth state of aggregation of matter: *plasma*.

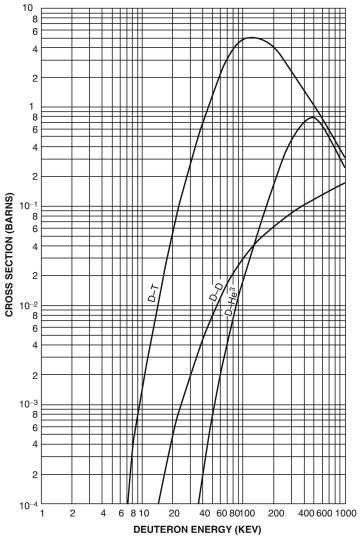

Figure 1.5: Nuclear fusion cross sections.

1.2.2 Plasma: the 4^{th} state of matter to exploit fusion

Plasma is defined as one of the four states of matter. It consists of a gas of ions, electrons and neutral atoms, exhibiting a *collective behaviour* [6]. A plasma is said to be fully or weakly ionized according to its content of neutral atoms. We will not enter further in the details of what a plasma is, but what we want to emphasize here is that in order for the atoms to approach each other quite likely, the electron cloud around

Table 1.3: σ_m and relative T_m of the fusion reactions represented in the graph above.

Nuclear fusion cross sections		
	σ_m [barn]	T_m [keV]
D-T	5	296
D-^{3}*He*	0.5	1970
D-D	0.03	246

the nuclei must be removed in some way and this is the main reason why plasmas are used for the production of energy from thermonuclear fusion. To achieve this, it is necessary to bring the plasmas to very high temperatures: estimating the temperature for fusion purposes, it must be of the order of keV and therefore tens of millions of degrees.

Since knowing the fusion reaction rate per unit of volume is the first step to begin to understand how fusion plants are built, let us therefore try to derive this quantity. Reaction rate is defined as the number of reactions of a certain type per unit of volume and time and one typical expression in nuclear physics is:

$$R = n_1 n_2 \sigma(v) v$$

n_1 and n_2 are the densities of the species and σ is the cross section. Energy released by one event of fusion W_{12} is the sum of the alpha particle kinetic energy ($W_3 = 3,5MeV$) and the neutron kinetic energy (($W_4 = 14,1MeV$)). In the context of plasmas, we need to introduce velocity distributions for the two populations $f_1(\vec{v}_1)$, $f_2(\vec{v}_2)$ and introduce a *kinetic average* on distributions. $\sigma(v)v$ is a function of relative speed $v = |\vec{v}_1 - \vec{v}_2|$ between two particles. The reaction rate becomes:

$$R = n_1 n_2 \langle \sigma v \rangle$$

with

$$\langle \sigma v \rangle = \frac{1}{n_1 n_2} \int \sigma(v) v f_1(\vec{v}_1) f_2(\vec{v}_2) \mathrm{d}^3 v_1 \mathrm{d}^3 v_2$$

If we take a velocity distribution that is for example a Maxwell-Boltzmann distribution function for the a-th plasma population:

$$f_a(\vec{v}) = f^{MAX}(\vec{v}) = n_a \left(\frac{m_a}{2\pi T_a} \right)^{\frac{3}{2}} e^{-\frac{\frac{1}{2} m_a}{T_a}(v_x^2 + v_y^2 + v_z^2)}$$

which depends on the temperature, defined as:

$$\frac{3}{2} n_a T_a = \frac{1}{2} m_a \int (v_x^2 + v_y^2 + v_z^2) f_a(\vec{v}) \mathrm{d}^3 v$$

we can write a reaction rate which depends on the densities and the temperature.

If we now do the calculations using the formula for the cross section reported in (1.4), we can obtain $\langle \sigma(v)v \rangle$ as a function of T_m and σ_m, which is the quantity represented in Figure 1.6. $\langle \sigma(v)v \rangle$ that is directly proportional to the fusion power S per unit volume: $S_f = n_1 n_2 \langle \sigma v \rangle_{1,2} W_{12}$, where W_{12} is the energy produced by one fusion event, $W_{12} = W_3 + W_4 = 3.5MeV + 14.1MeV$.

Finally, if we substitute the values of deuterium and tritium, we see that it is the most feasible of all the others, by order of magnitudes, and it is:

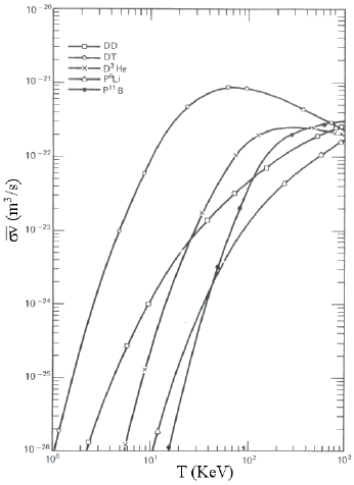

Figure 1.6: $\langle \sigma(v)v \rangle$ for some fusion reactions.

$$\langle \sigma v \rangle_{DT} \approx \frac{3.7 \cdot 10^{-12}}{T^{2/3}} e^{-\frac{20}{T^{1/3}}} \quad \left[\frac{cm^3}{s}\right]$$

1.2.3 Energy balances in the system

Let us take another step towards building a nuclear fusion power generation system: let us make now a power density balance for the plasma. We will assume that the power density coming from fusion is

$$S_f = S_\alpha + S_n$$

If we assume equal density, thermal equilibrium, global system neutrality and hydrogenic plasma, we can write the pressure $p = p_e + p_i = nT + nT = 2nT$. And so, from the fluid energy balance (see Section 2.2):

$$\frac{\partial}{\partial t}\left(\frac{3}{2}nT\right) = -p\nabla \cdot \vec{V} - \nabla \cdot \vec{q} + \eta j^2 + S$$

The variation over time of the internal energy is equal to the variation of pressure work ($p\nabla \cdot \vec{V}$), heat fluxes ($\nabla \cdot \vec{q}$), joule heating (ηj^2) and net possible energy source in the plasma $S = S_{ext} + S_f - S_r$ with $S_f = S_\alpha + S_n$ energy generated by fusion and S_r losses, for example due to Bremsstrahlung radiation.

Let us move in the direction of understanding, in a very simple and quantitative way, which requirements are needed to be able to extract energy from a plasma. We assume that we are in a stationary equilibrium situation ($\mathrm{d}T/\mathrm{d}t = 0$) and we include in S_{ext} the quantity ηJ^2. This can be done because it can be seen as externally supplied. Then we neglect the term $p\nabla \cdot \vec{u}$ related to the convection of energy, for example by thinking for each instant of time to make a volume integral and then divide by the considered volume. We model the heat fluxes as:

$$\nabla \cdot \vec{q} \triangleq S_q \triangleq \frac{\frac{3}{2}(n_i + n_e)T}{\tau_E} \triangleq \frac{\frac{3}{2}p}{\tau_E}$$

Where τ_E is the time related to the confinement of thermal energy in the system. Finally, we assume the neutrons to leave the plasma without interacting with it and so the only energy that can be considered as a source for the system is that one coming from alpha particles. So what we obtain is:

$$S_\alpha + S_{ext} = S_q + S_r \tag{1.5}$$

Energy that comes from fusion, summed up with the external energy is equal to thermal losses plus the radiation losses. This balance must lead to a self-sustaining situation and therefore to a situation where an external power is no longer needed to maintain the energy balance, i.e. a situation where $S_{ext} = 0$. This situation is called *plasma ignition*.

1.2.4 Lawson criterion

Let us now make some considerations that lead us in the direction of further simplifying the formula to arrive at a very simple and summary condition to say whether a physical system of this type can supply energy. We take

$$S_f = \frac{n^2}{4}\langle\sigma v\rangle W_f \rightarrow S_\alpha = K_\alpha \frac{\langle\sigma v\rangle}{T^2} p^2 \qquad K_\alpha \approx 1.4$$

approximate losses with Bremsstrahlung losses with

$$S_B = K_B \frac{p^2}{T^{\frac{3}{2}}} \qquad K_B \approx 5.3 \cdot 10^{-2}$$

and we substitute in the (1.5) at the ignition, we obtain

$$S_\alpha \geq S_q + S_B \rightarrow p\tau_E \geq \frac{\frac{3}{2}T^2}{K_\alpha\langle\sigma v\rangle - K_B T^{\frac{1}{2}}} \tag{1.6}$$

Now, if we put in the plasma ignition condition at a sufficiently high temperature to neglect the losses for Bremsstrahlung ($32keV$ for D-D reaction, $4.4keV$ for D-T), we obtain the so called *Lawson Criterion* (1.7):

$$p\tau_E \geq K_{ign} \frac{T^2}{\langle\sigma v\rangle} \tag{1.7}$$

The product between the pressure and the confinement time must be greater than a function of the temperature, that is minimized at a precise value. For D-T this is approximately $15keV$. Fixing the temperature at this value, we can find the value of the product between the pressure (or the temperature, since they are related) and the energy confinement time at the ignition:

$$(p\tau_E)_{ign} \approx 8.3 \text{ bar } s \qquad \rightarrow \qquad nT\tau_E \approx 2 \cdot 10^{14} s\ cm^{-3} \tag{1.8}$$

This (1.8) is known as the *triple product* and since the temperature is fixed, we can vary the density n and the time of confinement of the energy τ_E. This relationship sets the plasma conditions, which in turn define the best technological approach to follow.

1.2.5 Burning plasma and criticality condition

Let us introduce now two quantities, figures of merit of the system. The first one is the ratio between the net power produced in the system and the energy provided to the system Q and the second one is the net electrical power produced by the system divided by the electrical power input of the system Q_{eng}:

$$Q \triangleq \frac{S_f}{S_{ext}} \qquad Q_{eng} \triangleq \frac{P^{E_{out}} - P^{E_{in}}}{P^{E_{in}}}$$

The aim is now to find Q and Q_{eng} as a function of the quantities of the system that we know in order to maximize Q_{eng}, which includes the energy conversion efficiencies of the system.

If we want to consider the situation in which we must also supply energy from outside, it is useful to define $f_{ext}^{\alpha} \triangleq \frac{S_\alpha}{S_\alpha + S_{ext}}$ as the relative importance of the alpha particle contribution with respect to the whole source of energy. Then we can express Q as a function of f_{ext}^{α}. If we are above the ignition temperature:

$$Q = \frac{S_f}{S_{ext}} = \left(1 + \frac{W_n}{W_\alpha}\right) \frac{p\tau_E}{(p\tau_E)_{ign} - p\tau_E} = \left(1 + \frac{W_n}{W_\alpha}\right) \frac{f_{ext}^{\alpha}}{1 - f_{ext}^{\alpha}} \tag{1.9}$$

And also it can be expressed f_{ext}^{α} as a function of Q:

$$f_{ext}^{\alpha} = \frac{Q}{\left(1 + \frac{W_n}{W_\alpha}\right) + Q} \tag{1.10}$$

The first observation is that to have Q = 10, for a D-T plasma we have $f_{ext}^{\alpha} = \frac{2}{3}$. The second is that to have a fraction of injected power in the system that is equal to the net power produced by the system, so $f_{ext}^{\alpha} = \frac{1}{2}$, the corresponding Q is 5 and this situation is named as the *burning plasma* condition. To conclude we make the last observation: to have a system that does not require the injection of external energy, namely the ignition, the required Q is $Q \to +\infty$. This situation is the fusion analogue to the fission criticality condition, so the situation in which the number of neutrons produced by fission chain is the same as the number of neutrons that are lost by the system.

1.2.6 Through the construction of a fusion machine: engineering figure of merit and the blanket

Let us move to the construction of a fusion machine. Let us first define the conversion efficiencies, that link Q and Q_{eng}: η_e is the fraction of input electric power that can be transformed into thermal power for the plasma; η_a represents the efficiency of the plasma in absorbing this thermal power introduced in the system; η_{th} stands for the efficiency in the thermal-to-electric power conversion at the output and the most reliable choice consists in exploiting a thermodynamic cycle.

As said, the fuel is constituted by deuterium and tritium that must be provided to the system. Obtaining deuterium is not a problem, water is plenty of deuterium because this nucleus is stable. This can not be said about tritium, that is a radioactive isotope of hydrogen, with half life of 12.33 y. For this reason it is extremely rare on Earth and it has to be produced in some way to be used as fuel. To make matters worse, it must be produced with an energy cost that is low enough not to compromise the net positive balance of the electrical energy produced. Moreover it is extremely permeable and so radiation protection limits on the concentration of this isotope are imposed by the Nuclear Regulatory Commission [7].

The tritium problem can be solved thanks to the following reasoning. The power per unit volume that we have at the output is the sum of these contributions:

$$S_n + S_q + S_B + S_{ext}^{th}$$

where S_{ext}^{th} is the fraction of the energy injected in the plasma that is not absorbed by the plasma itself but can be recovered in some way. The main interest is set on the neutron power S_n: it has to be introduced an element that can absorb neutrons' kinetic energy, converting it into thermal energy.

One of the best choices is to use lithium, exploiting the reactions of the ^6Li (isotope percentage is 7.5%) and ^7Li (isotope percentage is 92.5%):

$$^6\text{Li} + \text{n} \longrightarrow \text{T} + {}^4\text{He} + 4.8\,\text{MeV}$$

$$^7\text{Li} + \text{n} \longrightarrow \text{T} + {}^4\text{He} + \text{n} - 2.5\,\text{MeV}$$

where the first reaction being exothermic while the second is endothermic. Using this material, therefore, also the problem of tritium production seems to be solved. Moreover, the ^6Li will effectively provide the neutron capture and give $4,8MeV$ of extra energy per neutron capture, this contribution will be indicated with W_{BL}. The remaining 93.5% of ^7Li acts as a moderator for neutron, to maximize the microscopic absorption cross section of the 6-isotope.

Now that we have solved the problem of the fuel, we have all the elements to look at the following Figure 1.7 and understand why a fusion plant is made in such a way.

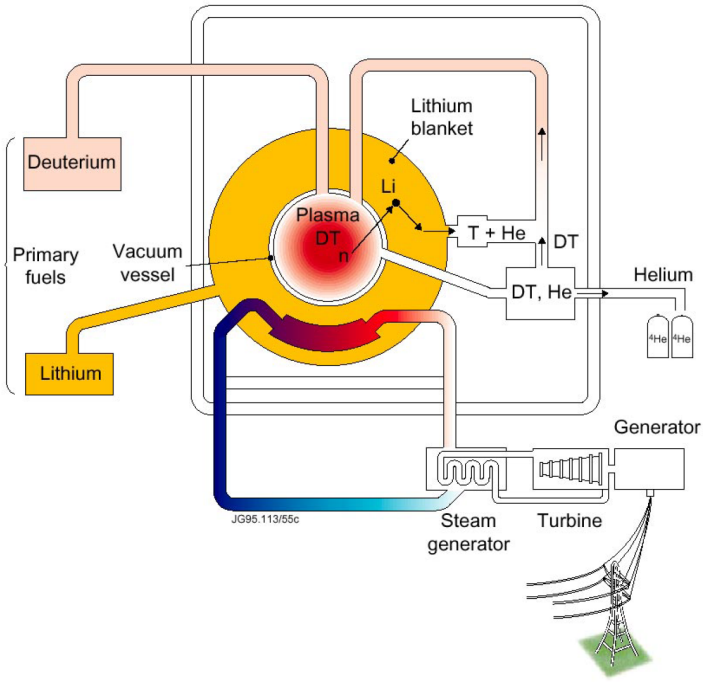

Figure 1.7: Schematic diagram of a fusion power station.

Looking at the scheme, we can see at the center the deuterium-tritium plasma, surrounded by the lithium blanket. On the left, then, we have

Table 1.4: Examples of Q and Q_{eng} when typical values of η_e of current fusion approaches are adopted.

Examples of Q and Q_{eng}		
Q_{eng}	η_e	
	0.7	0.1
0	≈ 3	≈ 30
1	≈ 7	≈ 55
5	≈ 25	≈ 170
10	≈ 45	≈ 300

the two fuels: deuterium and lithium. Tritium is considered as a product, not a fuel for the system, even if it is one of the two reagent of the fusion reaction. At the bottom we see the thermodynamic cycle, from which to extract the energy from the hot water steam and produce the electric power. At the top right the tritium cycle is reported: it has the function to separate the tritium produced in the blanket and to refill the core plasma.

Last thing we have to do in order to conclude the chapter is to write down the expression of Q_{eng} as a function of the other parameters and give an example of the required Q to reach some values of Q_{eng}. The expression is reported below and numeric examples have been resumed in the lateral Table 1.4, using different values of η_e.

$$Q_{eng} = \frac{(p\tau_E)_{ign}}{(p\tau_E)_{ign} - p\tau_E} \left(\frac{p\tau_E}{(p\tau_E)_{ign}} \left(\left(\frac{W_f + W_{BL}}{W_\alpha} \right) \eta_{th}\eta_e\eta_a + (1 - \eta_{th}\eta_e) \right) - (1 - \eta_{th}\eta_e) \right) \tag{1.11}$$

The values of the electrical energy conversion efficiency η_e included in the table were not randomly chosen: they are representative of the two main approaches to use thermonuclear fusion energy for large-scale electricity generation: inertial confined fusion (ICF) and magnetic confined fusion (MCF). These two methods will be explored in the next subsection. In any case, before explaining what these two approaches consist of, to have an idea about the Q_{eng} of nowadays fusion research, we say that the the most advanced facilities, the National Ignition Facility (NIF) for inertial confined fusion and ITER [8] for the magnetically confined fusion, are forseen to provide Q that would correspond to a $Q_{eng} \approx$ 0-1. We say "would" meaning that these systems are note able to convert the energy produced in electric energy: the target is not the electric power production but to build a plant that can reproduce the physics of the future reactor in all its facets and to represent a way to a standard fusion reactor.

1.2.7 Confinement approaches: inertial and magnetic confined fusion

The intent of this subsection is not to give a full explanation of the two technologies, but only to provide a brief introduction to the two schemes and some general estimates. Starting with the Lawson criterion that we have obtained in the former Section 1.2, we can reason about how to reach that value that fulfills the relation. That is

$$p\tau_E \rightarrow n\tau_E \approx 2 \cdot 10^{14} s cm^{-3}$$

We can work on τ_E or on the density n. If we try to maximize the energy confinement time and to reach a value of the order of the second, so $\tau_E \approx 1s$ we must have a density that is $n \approx 10^{14-15} cm^{-3}$. This approach leads to what is known as the *magnetic confinement fusion* (MCF) and this technology is covered extensively in the next Section 1.3. A different approach, in which we give up the aim to maximize the confinement time, consists in the *inertial confinement fusion* (ICF).

The idea is to compress a target with high-power lasers to bring thermonuclear fuel to ignition conditions: the confinement, once the Lawson criterion is met, is generated through the inertia of the external plasma, that confines the plasma density for a sufficient time to have a large number of fusion reactions in the target. The confinement time will be that time that is required by the system to disintegrate after it is brought to the pressure required for reaching those values of density given by the Lawson criterion. Since the energy density of the fuel is very high, in fact the rest energy characterizing 1 mg of DT-mixture can be evaluated to be 350 MJ, it means that no more than few milligrams of fuel can be used. The time to disgregate for a system with dimensions of about a fraction of a centimeter can be estimated to be of the order of nanoseconds, so to reach a large density, of $n \approx 10^{25}$, is required.

The target is spherical in shape, a schematic representation of it can be seen in the Figure 1.8. The laser beam hits the external surface of the target, which is ablated, and compresses the innermost layers. This type of mechanism can generate fluid dynamics instability, known as *Rayleigh-Taylor instability* and affects the efficiency of the target compression, which must be as isotropic as possible. For this reason, two different types of target geometry have been developed. One is named *direct drive* and the other is *indirect drive* (see Figure 1.9).

In the former, the laser beam is directed onto the surface of the fuel pellet and the goal is to reach isotropic implosion pressure through the laser configuration, while in the latter, the symmetry problem is overcome by placing the target inside a cylinder, made of high-Z and high density materials, so that it has high opacity to X-ray radiation to maximize the isotropicity of the incident laser beam. Direct drive, by virtue of its overall better coupling, might hold some advantage over indirect drive. However for direct drive, hydrodynamic instabilities are a constraint, leading to lower hydrodynamic efficiencies, and perhaps the need to pay a price in gain by purposefully ruining the isentrope. Ways to do so and not take a big penalty in gain is an area of active current research [10]. Efforts to study laser driven inertial confinement has been made in particular by the U.S. where the National Ignition Facility - NIF has been constructed at the Lawrence Livermore National Laboratory (LLNL) in California [9].

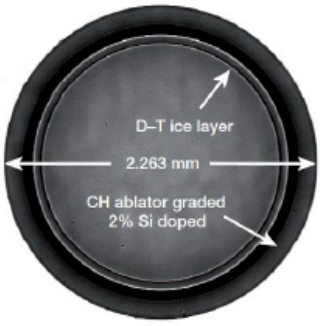

Figure 1.8: Example of a fuel pellet for Inertial Confinement Fusion.

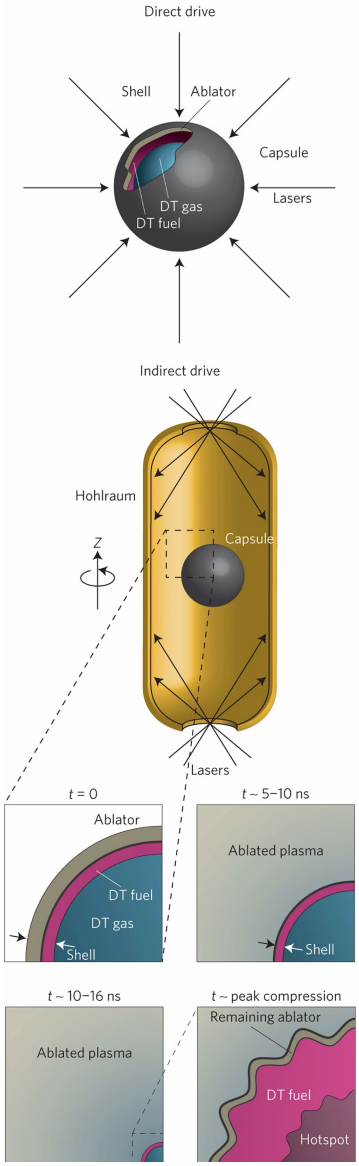

Figure 1.9: Direct and Indirect drive schemes [9]

1.3 Magnetically Confined Nuclear Fusion

In this section *magnetic confinement fusion*(MCF) is described in more details, in order to better understand the context in which this thesis work has been developed. In this second confinement approach, as we have already said before, the idea is to maximize τ_E until reaching plasma confinement times of the order of second. The strategy adopted is to use externally generated magnetic fields to be able to confine the plasma particles, which, being charged, are affected by the effect of external electromagnetic fields. It therefore seems useful to begin to illustrate this technology by explaining how charged particles behave when subjected to external electromagnetic fields. Before doing this, it must be emphasized that, taking confinement times such as those just stated, the plasma density to be reached will be much lower than that required by the ICF,

although there are also limits related to pressure instability in the system. In fact the maximum density for which these instabilities are controllable are expected to be around $n \approx 10^{14} cm^{-3}$ for a $10keV$ plasma.

1.3.1 Motion of a charged particle due to an external magnetic field

As previously said, the idea of magnetic fusion is basically to confine a sufficiently dense plasma for a sufficient time by means of magnetic fields. Therefore, it is fundamental to understand how plasma particles behave in presence of magnetic fields, in order to increase as much as possible the confinement time. The theory that exploits this phenomena is named as the *orbit theory*. The starting point for the development of the theory is the exact equations of motion as determined from Newton's law. For plasma physics applications only the magnetic and electric forces, given by the Lorentz force are required. Gravity plays a very small effect and can be neglected. The equations to be solved are thus:

$$m\frac{\mathrm{d}\vec{v}}{\mathrm{d}t} = q(\vec{E} + \frac{\vec{v}}{c} \times \vec{B}) \tag{1.12a}$$

$$\frac{\mathrm{d}\vec{r}}{\mathrm{d}t} = \vec{v} \tag{1.12b}$$

In general, $\vec{B} = \vec{B}(\vec{r}, t)$ and $\vec{E} = \vec{E}(\vec{r}, t)$ are functions of the three spatial dimensions plus time. Several general conservation relations can be derived from (1.12), like the conservation of energy and momentum. When applicable the conservation relations lead to "exact constants of the motion," which strongly constrain the particle's trajectory.

From the analysis of simple cases, such as the motion of a particle in a constant magnetic field and with no electric field, it can be understood that charged particles, like those in the plasma, perform an helical orbit named *gyration motion* around the axis parallel to the local direction of the magnetic field with a characteristic frequency Ω_L and a characteristic radius ρ_L around its axis, called respectively the *Larmor frequency* and the *Larmor radius* given by:

$$\Omega_L = \frac{eZB}{mc} \qquad \rho_L = \frac{v_\perp}{\Omega_L} \tag{1.13}$$

Where e is the electron charge, Z is the charge of the particle, c is the light velocity in vacuum and $v_\perp$ is the velocity of the particle perpendicular to the magnetic field $\vec{B}$. The helical trajectory is modeled through the decomposition of the motion around the center of the circular orbit (motion perpendicular to $\vec{B}$) and the motion of the center of the circular orbit, the so called *guiding center* that follows the magnetic field.

By exploiting this approach, it is possible to achieve confinement in the transverse direction but not in the one parallel with respect to the magnetic field.

Confinement in this direction can be obtained by two classes of device: open confinement systems and closed confinement systems. The definition refers to the topology of the externally generated field lines, which can be respectively open, usually starting from one solid surface of the vessel and ending on the other one, or closed, endlessly wrapped in a toroidal confinement region.

Typical devices belonging to the former category are linear plasma machines with specific magnetic field configuration that exploits the so called *mirror effect*, and typical devices belonging to the latter category are *tokamaks* and *stellarators* that we are going to describe in the next section. These two geometries are represented in these Figure 1.10 and Figure 1.11.

The phenomenon of mirroring can be understood qualitatively by examining Figure 1.12: it represents the trajectory of a particle moving into a region of increasing magnetic field. From the orbit theory it can be shown that, in the context of slowly varying magnetic fields, the quantity $\mu = \frac{mv_\perp^2}{2B}$ is an adiabatic invariant of the motion. As the particle gyrates and moves parallel to $\vec{B}$ into the high-field region, the value of $\vec{B}$ along the guiding center increases. $\mu = const.$ implies that $v_\perp$ must also increase. Next, recalling that in a static magnetic field the kinetic energy of a particle is an exact constant of the motion: $E = m(v_\perp^2 + v_\parallel^2)/2 = const.$ Consequently, an increase in $v_\perp$ must be accompanied by a decrease in $v_\parallel$. If the increase in B is sufficiently large, the particle eventually reaches a point along its trajectory where $v_\parallel = 0$.

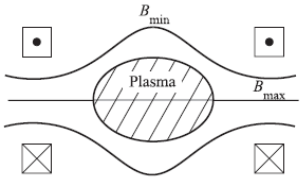

Figure 1.10: The mirror machine: an example of linear geometry

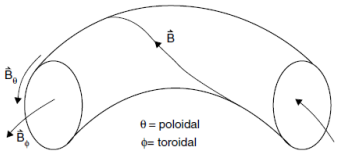

Figure 1.11: An example of toroidal configuration for plasma confinement.

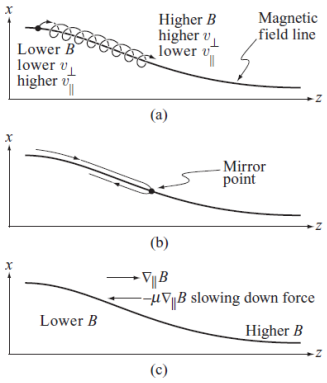

Figure 1.12: The mirror effect (a) as a particle moves into a region of higher B, $\vec{v_\perp}$ increases and $\vec{v_\parallel}$ decreases; (b) parallel guiding center velocity reflected at the mirror point where $\vec{v_\parallel} = 0$; (c) the parallel guiding center force.

In reality, linear machines are not suitable for confining a thermonuclear plasma for the production of electrical energy. In fact, these machines are mainly used for plasma-wall interaction experiments. The toroidal geometry is the one that certainly allows a better confinement because it does not have plasma losses at the ends.

To be able to talk about the motion of a particle in an exhaustive way, certainly several aspects are still missing. Here we will try to mention those strictly necessary for our purposes. In a non-constant but slowly variable magnetic field, where an electric field also exists, the particle trajectory is not simply directed along $\vec{B}$, but drifts arise in the $\vec{B} \times \nabla \vec{B}$ and $\vec{E} \times \vec{B}$ directions. Moreover, orbit theory is strictly valid only when we are considering single particle dynamics in a magnetic field. Things clearly become more complicate when a macroscopic system of interacting particles, like a plasma, is considered.

One instrument in this sense consists in a simplified model, the in which plasma is represented by a single fluid with infinite electrical conductivity and zero ion gyro radius. This model is the so called ideal *magneto hydrodynamics* (MHD) and is used when magnetic equilibrium configuration for magnetically confined plasmas has to be computed.

Ideal MHD equations can be derived from the guiding center theory or from a *fluid* description of the plasma. This second model will be described in more detail in Section 2.3.

The only thing worth saying now, in order to conclude this section, is that these MHD equations are derived assuming quasi-neutrality $n_e \approx n_i \approx n$ of the plasma and neglecting electron inertia. If then one

assumes stationarity $\mathrm{d}/\mathrm{d}t = 0$ and static condition, i. e. null plasma velocity, the ideal MHD equilibrium equations (1.14) are found:

$$\nabla p = \frac{\vec{j}}{c} \times \vec{B} \tag{1.14a}$$

$$\nabla \cdot \vec{B} = 0 \tag{1.14b}$$

$$\nabla \times \vec{B} = \frac{4\pi}{c}\vec{j} \tag{1.14c}$$

1.3.2 Magnetic configurations to confine the plasma: tokamak and stellarator

In a qualitative sense, MHD equilibrium in a toroidal geometry separates into two pieces: radial pressure balance and toroidal force balance. The first is due to the fact that plasma is a hot core of gas that tends to expand uniformly along the minor radius r and is also present in the linear configuration. The second equilibrium balance problem arises solely because of the toroidal geometry. Forces are generated by both the toroidal and poloidal magnetic fields that tend to push the plasma horizontally outwards along the direction of the major radius R. These two components are illustrated in the Figure 1.13 and Figure 1.14.

The toroidal force can be divided in three contributions: the *hoop force*, the *tire tube force* and the *1/R force*. The hoop force is analogous to the outward expansion force generated by the current flowing in a circular loop of wire. In the present case the current corresponds to the toroidal current flowing in the plasma. The tire tube force is so named because it is analogous to the situation in which the internal air pressure stretches the outside surface area of an inflated rubber tire tube more tightly than the inner surface area. Finally, the 1/R force arises because of the 1/R dependence of the toroidal field resulting from the toroidal geometry. All these affects are represented in Figure 1.15, Figure 1.16, Figure 1.17.

In addition to this effects due to the equilibrium configuration, there is also another aspect that can be derived from a stability requirement in the MHD context: if the section of the torus has a slight elongation and triangularity, it can be shown that a more effective stability can be reached. To do so, external currents are added to give the so called *D-shape* to the plasma section.

Without entering too much in describing all these phenomena, we say that the need to balance all these forces and effects presented leads to a specific configuration of the external magnetic field coils and the concept of the *tokamak*.

The tokamak was first proposed by two Russian physicists, Igor Tamm and Andrei Sakharov in 1952 [11]. The name is a Russian acronym *TO(roidalnaya) KA(mera) MA(gnitnaya) K(atushka)* which stands for toroidal chamber with magnetic coils.

One example of the coils' scheme is given in Figure 1.18. The toroidal magnetic field B_θ, which is the dominant component of $\vec{B}$ in this kind of machines, is generated by current flowing in external poloidal coils, while the poloidal component B_ϕ is produced by the toroidal current flowing in

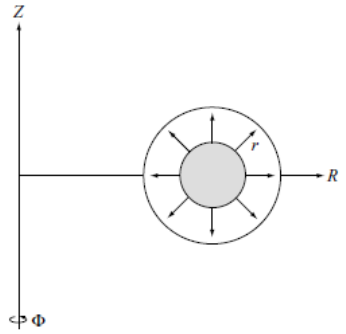

Figure 1.13: Outward pressure expansion force along r in both linear and toroidal configurations

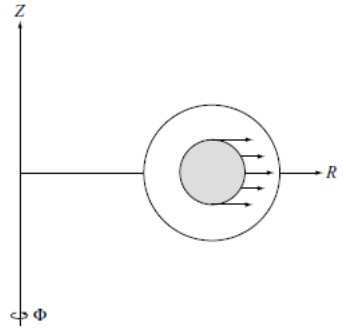

Figure 1.14: Outward force along R due to toroidicity

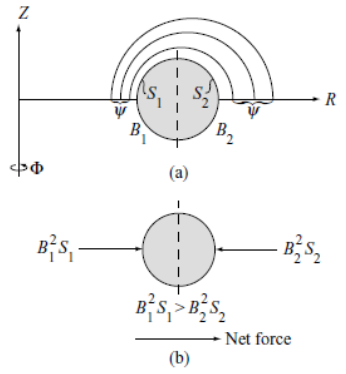

Figure 1.15: Qualitative picture of the hoop force: (a) conservation of flux showing that $B_1 > B_2$; (b) toroidal force balance showing a net outward force along R.

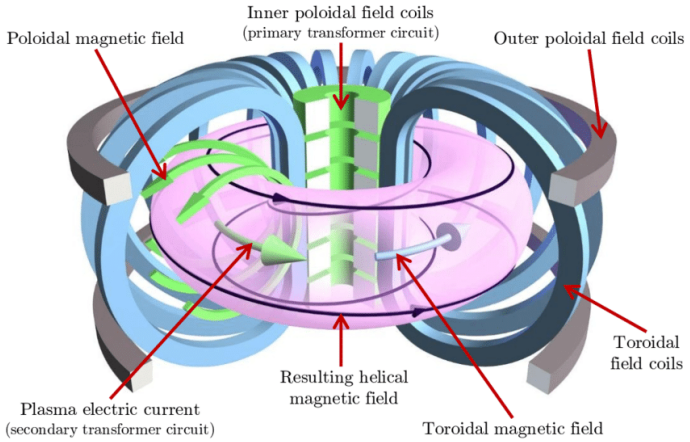

Figure 1.18: Coils' scheme in a tokamak.

the plasma itself. In tokamaks, this plasma current is induced exploiting the phenomenon of *electromagnetic induction*, generated by the current flowing in a central *Ohmic transformer*. Plasma current, moreover, allows the exploitation of Ohmic heating to increase the plasma temperature. Finally, coils in the toroidal direction are present, with the main objective of controlling the shape and the equilibrium of the plasma.

A peculiar characteristic of tokamaks, connected precisely to the fact that the plasma current is generated thanks to the phenomenon of magnetic induction, is their *pulsed* functioning. In fact, only the variations of electric current generates magnetic fields and vice versa, so a stationary operation is not possible. On the other hand, a device that can operate continuously is the *stellarator* scheme, which we see in Figure 1.19.

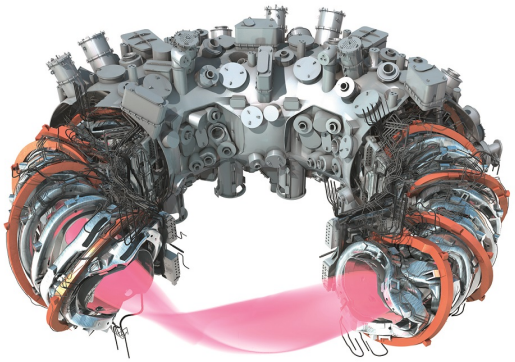

Figure 1.19: Scheme representation of the stellarator Weldstein 7-X.

The main feature of the stellarator scheme is that, to balance the forces arising from the toroidal geometry, it does not exploit the use of the central solenoid, but exploits the technique of wrapping the D-section on itself. It can be proven that this configuration provides a stationary functioning of the machine, but the cost of this advantage is the considerable complexity added to the construction of the machine.

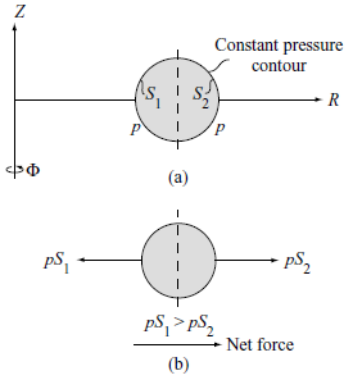

Figure 1.16: Qualitative picture of the tire tube force: (a) constant pressure with $S_2 > S_1$; (b) toroidal force balance showing a net outward force along R.

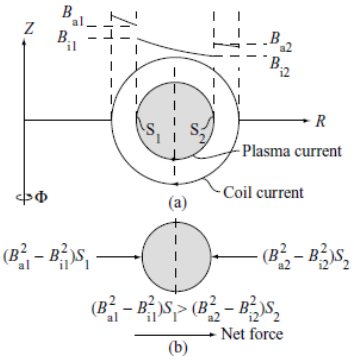

Figure 1.17: Qualitative picture of the $1/R$ force: (a) surface current model showing the $1/R$ dependence of B_Φ along the mid plane $Z = 0$; (b) toroidal force balance showing a net outward force along R

1.3.3 An example of tokamak: ITER

To understand the complexity of a magnetic confinement machine for thermonuclear fusion, we observe as an example a scheme of tokamak, which is the least complex between the two previous solutions (and this, as we will see, is certainly not synonymous of simple) and also the more promising from the perspective of large-scale electricity generation.

Let us analyze the most relevant tokamak in the contest of magnetically confined thermonuclear fusion: ITER [12]. It takes the name from latin and its meaning is "The Way". The reason under this name is that the experimental campaign that will be carried out at ITER is crucial to advance fusion science and pave the way for the fusion power plants of tomorrow.

It is under construction in southern France, at Cadarache, and 35 nations are collaborating to build the world's largest tokamak. With ten times the plasma volume of the largest machine operating today, ITER will be the first fusion device to maintain fusion for long periods of time, the first fusion device to test the integrated technologies, materials, and physics regimes necessary for the commercial production of fusion-based electricity.

The machine has been designed specifically to produce 500 MW of fusion power from 50 MW of input heating power (Q=10): ITER will not convert the energy it produces as electricity; demonstrate the integrated operation of technologies for a fusion power plant; Achieve a deuterium-tritium plasma in which the reaction is sustained through internal heating; test tritium breeding, so to demonstrate the feasibility of producing tritium within the vacuum vessel; demonstrate the safety characteristics of a fusion device.

All the initial experimental activity of ITER will be done using helium plasmas [12]. The choice of this gas as the primary plasma species rather than a mixture of D − T or even just of D is mainly due to issues of a radioprotection nature (in the first case) and to simplifications of the plasma behaviour for the validation of the codes, in fact D forms molecular compounds such as D_2 which complicate the physics of the problem.

Let us see an ITER picture in the next Figure 1.20 with the aim both to understand the technological complexity of the development of such an engineering work and to better frame the research work connected to the plasma-wall interaction, which is the framework of this thesis.

The tokamak weights 23.000 tons, and the plasma temperature is designed to reach the temperature of 150 million K. The surface of the tokamak is sized to absorb neutron power that is approximately $4 - 5 MW/m^2$ being careful, however, not to increase the volume of the vacuum chamber too much, which would put the pumping system in difficulty.

Superconducting materials are necessary for high currents in the magnets, of the order of 10^4 ampere, and another constraint is the maximum value of the magnetic fields achievable nowadays: $B_{max} \approx 12 - 15T$. Irradiation of these superconducting coils has to be avoided, in order to save them. Another complication is due to the fact that these superconducting

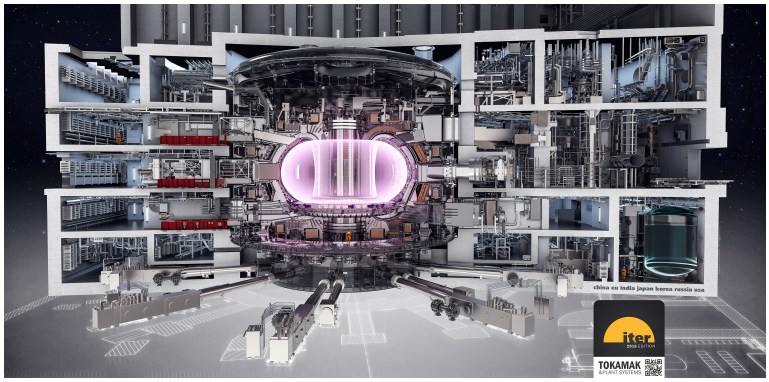

Figure 1.20: Construction scheme of ITER.

materials work at temperatures that are of the order of $5K$, while at the center of the core we have the thermonuclear plasma.

Reaching a value of the ratio between thermodinamic pressure and the magnetic pressure of the order of 5-10% is a good challenge. This ratio is important because it represents a sort of efficiency with which the plasma is confined by the magnetic field. But however it must be suitably tuned, because if the magnetic field is too large and the ratio becomes lower than a certain value, fixed by the so called *Trojon limit*, we start having MHD instabilities in the system.

Plasma-heating devices, diagnostics, control, cryogenics, remote maintenance, pumps, etc. must be integrated into the machine design and function properly in such extreme conditions. We could go on about technology issues, but now we want to face one of the problems: the plasma-wall interaction in the context of magnetic confined fusion. Next subsection is dedicated to this topic.

1.3.4 An unavoidable touch: limiters and divertors

In reality, despite the presence of all the magnetic fields listed above for the balance of forces in toroidal geometry, the plasma still tends to diffuse beyond the magnetic field lines. This means that if a bare vacuum chamber were maintained, the magnetic field lines would come very close to the chamber wall. Thus the plasma would inevitably come into direct contact with the chamber wall, damaging it.

Magnetic field lines which lie on flux surfaces that never make contact with a solid surface are termed *closed*, while those which pass through a solid surface are termed *open*. A key role is played by the last closed (magnetic) flux surface, LCFS. The LCFS is the last flux surface, going outwards from the main plasma, that does not touch a solid surface. Surfaces radially further in are all closed while those further out are all open.

The solutions that are adopted, therefore, are mainly two and they are both in the direction of limiting the last closed surface of the magnetic field to a smaller radius than the internal one of the chamber section. The plasma will therefore remain confined to a narrow region with respect to the wall of the vacuum chamber.

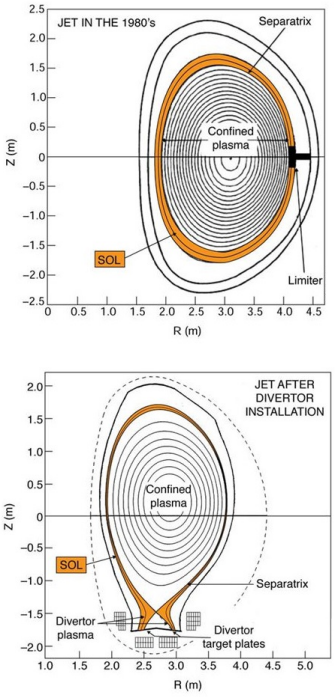

Figure 1.21: Qualitative schemes of the limiter and the divertor configurations.

The two methods are called *limiter configuration* and *divertor configuration*, represented in Figure 1.21. The limiter solution consists in inserting an element inside the plasma that interrupts one of the magnetic field surfaces, making it open. Basically, an element is voluntarily introduced where the plasma collides, in order to preserve the rest of the internal wall of the chamber.

The divertor configuration, on the other hand, is obtained by means of one or more external electric currents which are made to flow outside the chamber. They generate an open magnetic field to make the plasma collide on a specific area of the chamber. This is usually placed at the bottom of the chamber and this area is called divertor. As an example, we show the ITER divertor in Figure 1.22.

The original motivation for introducing divertors in magnetic confinement devices was to reduce the main plasma contamination due to the plasma erosion of solid surfaces by moving the solid surfaces away from the core [13].

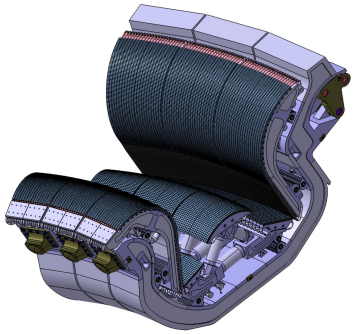

Figure 1.22: Constructive design of the ITER divertor.

Moving away the source of impurity from the core plasma opens also the possibility to dissipate the power reaching the edge by volumetric processes such as radiation, which can be obtained thanks to impurity atoms emitted from the wall due to sputtering or by seeding of neutral gases such as neon or nitrogen. This is of course beneficial since it allows to spread the power over larger areas [14].

In principle, this can be achieved also in limiter configurations, however, due to their proximity with the core plasma, injection of gas impurities can increase the risk of core plasma contamination.

We will not go into the merits of on-board plasma physics, this will be done in the following Chapter 2. Let us say that in general, when a thermonuclear plasma is in contact with a solid surface, various phenomena take place. The branch of research that deals with them is the so-called plasma-wall interaction.

1.3.5 One piece of the puzzle: the importance of managing the plasma surface interaction and the role of linear plasma devices

At this point we say that the context in which the research is inserted is clear, some of the problems associated with plasma edge physics have also been mentioned and will be analyzed specifically in the next Chapter 2. Before concluding the chapter, it is necessary to mention the role that linear plasma devices play in the research of plasma-wall interaction.

At the moment, there is no tokamak able to reproduce the conditions expected in ITER [15], in particular the ion flux of about $10^{24} m^{-2} s^{-1}$ in the divertor region. Tokamaks are fundamental to study the impact of the plasma-wall interaction (PWI) on the overall performances of the machine, e.g. plasma confinement capability, but are not able to fully assess plasma-facing components' materials modifications of future experiments or power plants. Moreover, PWI in tokamaks is usually the sum of the results of numerous plasma discharges, which can differ for the parameters used. Therefore, it is quite complicated to correlate the

modifications obtained and the plasma conditions to achieve them. Linear machines are thus built in order to try to overcome these problems.

As we have already seen, in the case of linear machines, the magnetic field lines are open and directed perpendicular to the side walls of the chamber. The fact that the plasma moves longitudinally towards these can be exploited to place samples inside the chamber, therefore exposed directly to the plasma, for the study of their morphological modifications.

Linear machines are quite diffused all over the world and each one of these machines has its own characteristics. They can work either in a pulsed or in a continuous way, their common goal is to reach at least some of the ITER expected exposure parameters in a specific area of the first wall, e.g. the divertor region or the vacuum chamber. We have for example: Magnum-PSI at the Dutch Institute for Fundamental Energy Research (DIFFER) in Eindhoven [16]; PSI-2 at the Forschungzentrum Julich [17]; NAGDIS I and II at the Nagoya University [18]; PISCES A and B at the University of California in San Diego [19]; MAGPIE at the Australian National University [20]; GyM at the Istituto per la Scienza e Tecnologia dei Plasmi (ISTP) of the Consiglio Nazionale delle Ricerche (CNR) in Milan [21].

This last machine, is the one that has been simulated in the context of this thesis and with the aim both of further clarifying the constructive scheme of a linear machine and of understanding the object of this thesis work, we are going to present the linear plasma device in Section 1.4.

1.4 An example of a linear plasma device: GyM

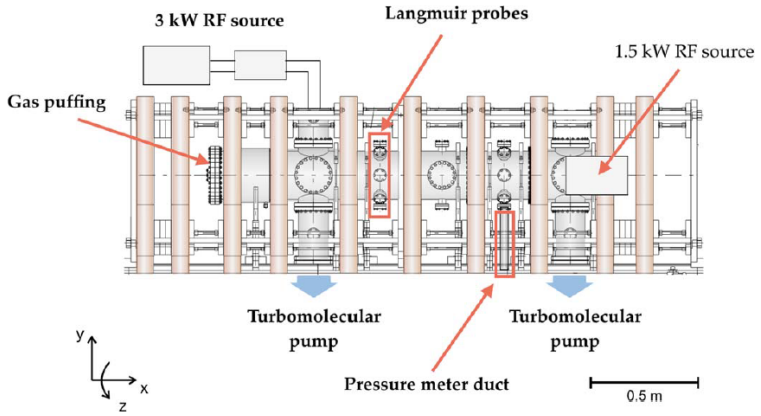

Figure 1.23: Schematic drawing of GyM linear machine with the magnetic field coils and the vacuum chamber. The Langmuir Probe (LP) location, the RF sources at $2.45GHz$ capable of delivering up to $4.5kW$ and the gas nozzle located at one end of the cylindrical vacuum vessel are shown. The $1.5kW$ RF source is reported in figure, but it will not be considered in the following. [22], [21]

GyM (acronym for *Gyrotron Machine*) in Figure 1.23 is a linear machine designed and built in the *Istituto di Fisica del Plasma "Piero Caldirola" (IFP)* that in 2019 became *Istituto per la Scienza e Tecnologia dei Plasmi (ISTP)*. The main chamber consists of a cylindrical stainless steel vacuum vessel of $0.25m$ diameter and $2.11m$ length surrounded by 10 magnetic coils and equipped with 32 access flanges for diagnostics, pumping systems and sample insertion to be exposed to plasma.

The experimentation covers various aspects and phenomenologies, such as turbulence studies and coherent structures typical of the tokamak

Table 1.5: The table shows the main parameters of GyM.

GyM main parameters	
diameter	$0.25m$
length	$2.11m$
n_e	$10^{15} - 10^{17}m^{-3}$
T_e	$10eV$
B	$0.1T$
plasma sec. a	$10cm$
plasma	H_2, D_2, He, Ar, N_2

plasmas, instabilities associated with drift waves and studies of the electron velocity distribution function.

With high-density plasmas the study of the interaction between energy ions and the surfaces of materials can be performed, opening up the possibility of characterizing processes of high technological interest, particularly in the fusion field.

1.4.1 Magnetic field configuration and diagnostics in GyM

The standard magnetic configuration in GyM is obtained connecting in series all the 10 coils, so that the same electric current flows in each of them. The resulting magnetic field is directed along the axis of the cylinder and its intensity is tuned by changing the axial coil distance. The magnetic field can reach the maximum value of about $0.13T$. The magnetic field is obtained by solving the Grad–Shafranov equation [22]

$$\Delta^* \psi = -\frac{4\pi}{c} R J_z \tag{1.15}$$

where ψ is the flux function, R is the radial coordinate, J_z is the azimuthal current density, it includes the contributions coming from the external magnetic field coils. The stream-function ψ results from the solution of (1.15) for GyM. If considering a coil current of $600A$ the solution is shown in the Figure 1.24.

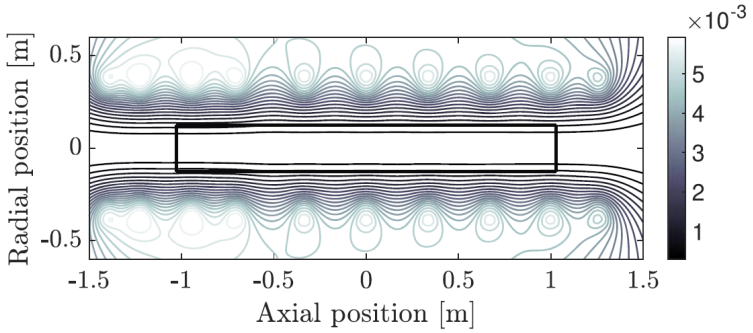

Figure 1.24: Contour lines of the stream-function ψ in $[Tm^2]$ for GyM standard coil configuration at 600 A. The solid black lines mark the GyM vacuum vessel.

GyM is equipped with diagnostic systems for the measurement of fundamental plasma parameters. The main diagnostics include Langmuir probes (fixed and mobile), optical emission spectroscopy, a fast video camera (250 kframes /s) with image intensifier and mass spectrometry.

1.4.2 Plasma generation: the radiofrequency source

The plasma in GyM is generated and sustained exploiting the *electron cyclotron resonance* (ECR) heating mechanism at 2.45 GHz. Inside the vessel, the wave interacts withe the plasma in the region where the resonance condition in satisfied. This mechanisms directly heats only the electron population and brings an electron temperature of up to 10 eV. This, in combination with the relatively low plasma density (electron density $\approx 10^{15} - 10^{17} m^{-3}$), results in a cold ion population ($\approx 0.1eV$) in the plasma. Plasma is highly reproducible and it can be H_2, D_2, He, Ar, N_2.

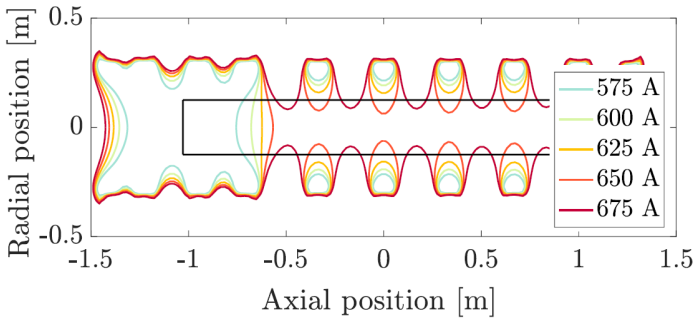

Figure 1.25: ECR location for different values of B or, equivalently, current in the coils.

From Figure 1.23, we can see the location of the two *radiofrequency* (RF) sources delivering up to $3.0kW$ and $1.5kW$, capable of delivering up to $4.5kW$ of continuous power, and 8 kW in pulsed mode, the *Langmuir Probe* (LP), the gas injection nozzle, the two turbomolecular pumps and the pressure gauge. Among the two RF sources installed on the machine, here we will consider only the one which can deliver up to $3.0kW$.

As shown in Figure 1.23, this is connected to the vessel through a waveguide. In Figure 1.25, we show the location on the (Z, R) plane of the ECR region in GyM for different values of the coil current or, equivalently, for different values of B.

In this work we will consider the magnetic field configuration corresponding to $600A$, for which the ECR is located around a very narrow axial region. Additional resonances might be present in the machine, related to the upper-hybrid branch of the dispersion relation. Their location in the machine is, however, difficult to predict, since they depend on the local plasma density, which is not known a priori. For this reason, in this work we neglect the presence of such additional resonances. Furthermore, direct measurements of the EC absorbed power are not available at present for the plasma of GyM.

Plasma-Wall Interaction and Impurity Transport

2

2.1 Relevant physics in the scrape-off layer 24
2.2 Modelling the plasma edge with SOLPS-ITER 29
2.3 Modelling the plasma-wall interaction and impurity transport with ERO2.0 39
2.4 Overview on the reference literature context 43
2.5 Motivations and aim of the work 46

The name of plasma-wall interaction in the context of magnetic confinement thermonuclear fusion refers to a very wide range of physical processes and consequently there are many areas of research that deal with specific aspects of this vast topic. In this chapter the intent is, first of all, to analyze some of the phenomena related to the physics of the plasma-wall interaction from a theoretical point of view. Such as the formation of the *plasma sheath*, the interaction of atomic particles with the plasma, the mechanism of particle *sputtering* and the transport of the eroded particles. These aspects will be presented in Section 2.1. In Section 2.2 and Section 2.3 the models that are developed to model the physical phenomena described in Section 2.1 are explained with direct references to the codes that solve the associated equations to the aforementioned models and that have been used in this thesis work. In particular, in Section 2.2 we focus on plasma models, on the fluid model and on the interactions of the neutral particles coming from the walls with the plasma in the framework of the SOLPS-ITER code. The Section 2.3 instead describes the erosion and transport models of the eroded particles, modeled using the ERO2.0 code. To conclude, in Section 2.4 we come to an overview of the state of the art both from the experimental and modelling point of view of this thesis work, and in light of this section, in Section 2.5 motivations and aims of the thesis work are presented.

2.1 Relevant physics in the scrape-off layer

This section analyzes the main phenomena that occur when a plasma comes into contact with a solid surface. We have already said that it cannot simply be confined by some magnetic configuration. In fact, even if trying to perfectly balance the forces that originate from having a toroidal geometry, the plasma tends to diffuse, due to collisional diffusion and turbulence phenomena. We have also already talked about the two possible solutions to control the position of the last closed magnetic field surface: the limiter and divertor configuration. The two configurations allow us to limit the interaction between the very hot plasma and a solid surface in a well-defined region of the tokamak. The region of space that extends from the last closed magnetic field line (LCFS) to the solid wall is indicated by the name of *scrape-off layer* (SOL), see Figure 2.1.

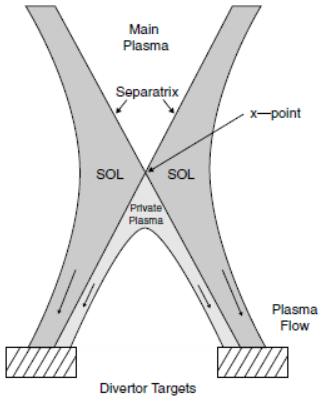

Figure 2.1: The SOL is the region of space that extends from the last closed magnetic field line (LCFS) to the solid wall

The first and fourth states of matter do not coexist easily. To get an idea of the huge variety of processes that take place in the context of the plasma-wall interaction we will refer to the following Figure 2.2 taken from [23].

For example, the plasma tends to erode the surface where it collides, due to the great energy of the particles that are contained in it. If the plasma contains radioactive materials also the fuel retention must be considered. Formation of helium bubbles due to the diffusion can be also observed,

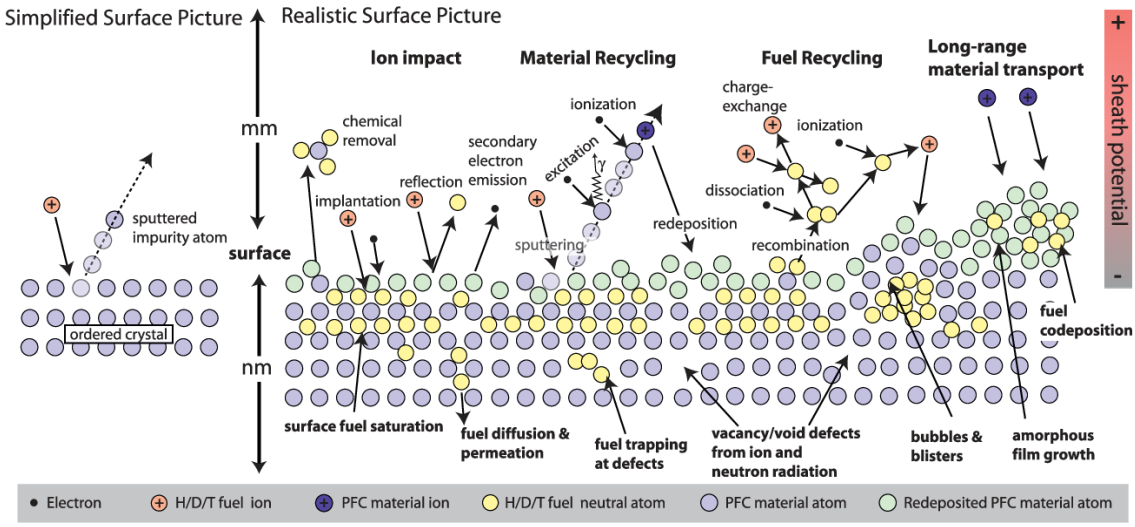

Figure 2.2: Summary of the most relevant physical processes in the plasma-wall interaction [24].

together with vacancies and voids defects formation due to neutron irradiation. In the plasma charge exchange reactions between eroded particles and the plasma can happen, ionizations, elastic collisions, etc. The eroded particle disturb the plasma, if they reach the core plasma they dissipate energy through Bremsstrahlung radiation, which we remember to be much more effective if the particles have a high atomic number Z.

Surface erosion is mainly due the establishment of what is called *plasma sheath*, which consists in the formation of an electric potential (*sheath potential*) which slows down the electrons but accelerates the ions in the direction of the wall and makes the collisions of these with the wall considerably more effective. Let us therefore analyze all the main physical processes related to this thesis work, addressing as a first question the formation of plasma sheath from a quantitative point of view.

2.1.1 Formation of the plasma sheath

Plasma sheath was one of the first described phenomena related to plasma-wall interaction (Tonks and Langmuir, 1929 [25]). Immediately after the plasma condition is achieved, due to their higher mobility, electrons reach more rapidly the walls with respect to ions. As a consequence, the solid surface gains a negative charge, counterbalanced by a region of net positive charge inside the plasma in the proximity of the wall, while the plasma far from the wall remains almost neutral. Due to this charge imbalance, an electrostatic potential ϕ arises, with the effect of accelerating ions towards the wall, until an equilibrium situation is reached. This region is particularly important for plasma-wall interaction and takes the name of *plasma sheath*. In Figure 2.3 the sheath features are summarized.

A simple 1D model can be used to estimate the dimension of the sheath. Its dimensions can be easily estimated in the 1D case starting from the hypothesis that plasma is quasi-neutral far from the sheath, electrons can be considered in thermal equilibrium according to a Maxwellian

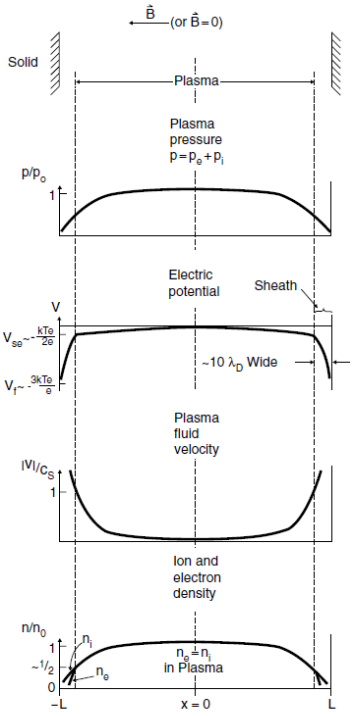

Figure 2.3: Schematic of the variation in 1D of plasma pressure, electric potential, plasma velocity and ion/electron densities in the plasma between two semi-infinite planes. The thickness of the sheath is exaggerated for clarity. The total length is 2L. Image taken from [13]

distribution, ions can be considered as drifting cold particles ($T_i = 0$) like a monoenergetic beam of particles. Taking the electron density as:

$$n_e(x) = n_0 e^{\frac{e\phi}{k_B T_e}} \tag{2.1}$$

with ϕ being the electrostatic potential and n_0 the density in the upstream plasma, and the ion density from the conservation of energy and momentum:

$$n_i(x) = n_0 \left(1 - \frac{2e\phi}{m_i v_{se}^2}\right)^{-\frac{1}{2}} \tag{2.2}$$

Where v_{se} is the cold ion velocity upstream, at the sheath edge. Substituting in the Poisson equation [26][13]:

$$\frac{\mathrm{d}^2\phi}{\mathrm{d}x^2} = 4\pi n_0 e \left[e^{\frac{e\phi}{k_B T_e}} - \left(1 - \frac{2e\phi}{m_i v_{se}}\right)^{-\frac{1}{2}}\right] \tag{2.3}$$

From this equation then one can find:

$$\lambda_{se} \approx \sqrt{\frac{T}{4\pi e^2 n_e}} \triangleq \lambda_D \tag{2.4}$$

namely the thickness of the sheath region λ_{se} is of the order of the Debye length λ_D. For typical tokamak edge conditions, $T_e \approx 20eV$ and $n \approx 10^{19} m^{-3}$, so from (2.4) $\lambda_{se} \approx 10^{-5} m$. The potential drop in the sheath $\Delta\phi$ can be estimated as:

$$\Delta\phi = \frac{1}{2}\frac{kT_e}{e} \ln\left[\frac{2\pi m_e}{m_i}\left(\frac{T_i}{T_e} + Z_i\right)\right] \tag{2.5}$$

The boundary between the sheath region and the rest of the plasma is rather sharp. However, it is possible to identify a broader region before the sheath, called *pre-sheath*, into which the charge imbalance and the electric field are smaller with respect to those in the sheath, but sufficient to drive ions towards the sheath region. With the hypothesis made so far it is possible to demonstrate two things: the first is that the ions fluid velocity at the sheath edge v_{se}, could not exceed the sound speed c_s without singularities arising [26][13], namely:

$$v_{se} \leq \sqrt{\frac{k_B(T_e + T_i)}{m_i}} \triangleq c_s \tag{2.6}$$

The second, instead, is that looking at the sheath side, in order to have a non-oscillatory behaviour of the electrostatic potential in the sheath, it can be shown that

$$v_{se} \geq c_s \tag{2.7}$$

which is the so-called *Bohm criterion* [13]. As a consequence the only possibility for the plasma to satisfy both inequalities is that the ions velocity at the sheath entrance is exactly equal to the sound speed. Therefore, despite its small dimension, the presence of the sheath should be always taken into account from the plasma-material interaction point of view. The potential drop arising between the plasma and the wall is able to accelerate ions towards the solid, enhancing phenomena like sputtering and erosion, which will be described in the following sections. Also v_{se} is proportional to T_e so an important thing to reduce the energy with which the particles hit the wall is to keep the electron temperature low.

2.1.2 Interaction of atomic species in edge plasma

When a positively charged particle collides with a solid surface, one of three things usually happens: it undergoes the phenomenon of *backscattering*, returning to the plasma with an energy lower than the starting one, it can implant near the surface and subsequently be released as a *thermal particle* or it can remain trapped in the surface for an extremely long period of time. Since the solid wall, as explained in the previous paragraph, is negatively charged, when a charged particle collides with it, a *radiative recombination* can occur, which brings the charged particle back to its neutral condition. The resulting neutral particle will be less subject to wall attraction and will tend to re-enter the plasma. This phenomenon of radiative recombination and subsequent desorption back into the plasma is referred to as *particle recycling* and the plasma is said to *refuel itself* [13].

When switching on a tokamak-type machine, the surface possibility of retaining ions saturates and then all the ions arriving on the wall are thrown back into the plasma either as ions or as neutral (mostly as neutral). So the *particle recycling* initially will have the net effect of decreasing the amount of particles present in the plasma and it will be necessary to add some gas (*gas puffing*) through external pumping systems. After the initial transient, however, a situation of equilibrium will be reached where the net effect of recycling will be zero.

Recycling causes re-entering of neutral atoms from the walls in the the plasma. In the scrape-off layer, neutral particles can interact with plasma particles in different ways depending on the plasma regime, affecting reciprocally their properties. Among the different reactions that can take place between the atoms in the SOL, in this analysis we have considered four of them and they are:

- *elastic scattering*
- *electron ionization*
- *charge exchange*
- *radiative recombination*

The *elastic scattering* can occur between ions, between neutral atoms and between neutral atoms and ions. The effect it has on the atoms involved in the collision is to vary the kinetic energy of the reactants and their direction of motion. *Electron ionization* consists of the collision between an electron in the plasma and an atom, which can be either

neutral or positively charged if it has more than one electron to lose. After the collision, the atom is positively charged. During the collision it can also happen that the atom, only absorbs part of the electron's kinetic energy, remaining in an excited state, and not being ionized. This leads to the subsequent emission of a photon. The *charge exchange* involves the collision between two atoms with different charges and in the collision they exchange an electron. Finally, *radiative recombination* is a physical process that involves a positively charged atom and an electron: the first captures the electron and then a photon is emitted.

From the discussion just made, it is clear that treating this type of phenomena in the best possible way, from the computational point of view, is of fundamental importance, because the reactions that occur in the SOL drastically determine the plasma population parameters.

2.1.3 Sputtering and erosion

Let us analyze now what happens when an energetic ion (or even a neutral particle with sufficient energy) collides with the wall and interacts directly with the atoms that compose it. The kinetic energy of the incident particle can be sufficiently high to be able to pull out one or more atoms from the solid wall. This process occurs only through high energy collisions because the atoms in the crystal lattice are bonded to each other and is called *physical sputtering*. This phenomenon is characterized by a *threshold* trend, i.e. it is necessary for the incident particle to transfer an energy greater than E_{th} (*threshold energy*) that at least exceeds the binding energy of the solid particle to its lattice, called *surface binding energy* E_{SB}. The sputtering can be due either to a collision, where it is the transfer of kinetic energy that causes the ejection of the target particle, or due to the establishment of a chemical bond between the incoming particle and the solid particle, the so-called *chemical sputtering*. In addition to this distinction among physical nature of sputtering, we can speak of *self-sputtering* if the incident particles are of the same chemical species as those they affect.

When an elastic collision between particles occurs, the maximum fraction of energy that can be transferred from the incident to the target particle depends on the masses of the two particles. The maximum fraction of energy transferred is in fact given by [13]:

$$\gamma = \frac{4M_1M_2}{(M_1 + M_2)^2} \tag{2.8}$$

Where M_1 and M_2 are the masses of the two colliding particles. In general, in the context of tokamaks, the incident particles are much lighter than the target ones and therefore the fraction of energy transferred is basically small and this certainly goes in the direction of preserving the surface. However, this cannot be said with regard to the phenomenon of self-sputtering: with the same energy of the incident particle, this type of impact is much more effective in causing sputtering. The energy required for sputtering to occur can be calculated with the formula (self-sputtering makes E_{th} singular, it cannot be described by this formula):

$$E_{th} = \frac{E_{SB}}{\gamma(1-\gamma)} \tag{2.9}$$

While the energy of the particle ejected from the surface can be easily calculated with:

$$E_{\text{ejected}} = \gamma(1-\gamma)E_{in} - E_{SB} \tag{2.10}$$

Where E_{in} indicates the energy of the incident particle. The phenomenon of sputtering, if prolonged over time, can cause both a variation in the morphology of the surface and the *erosion* of the same, and therefore a macroscopic variation of its geometry.

Experimentally the physical sputtering can be characterized by the yield $Y(E_{in}, \theta_{in})$, usually a function of both the energy of the incident particles and the angle of incidence with the surface θ_{in}, which is the number of eroded particles per incoming projectile and can be defined as [27]:

$$Y = \frac{\Gamma^{\text{ero}}}{\Gamma^{\text{in}}} \tag{2.11}$$

where Γ^{in} and Γ^{ero} are the fluxes of the incoming projectiles and the eroded particles respectively.

2.1.4 Transport and re-deposition

If the choice of the material goes in the direction of high atomic numbers to avoid the phenomenon of sputtering as much as possible, on the other hand it must move in the opposite direction to avoid a too consistent cooling of the plasma due to the Bremsstrahlung radiation, which is proportional to Z^2. The impurities that are eroded from the surface tend to dirty the plasma by absorbing energy from it.

When we talk about *transport and re-deposition* within the context of magnetic confinement physics we mean the study of the trajectories and interactions of particles eroded from the surfaces. The particles are usually eroded as neutrals which can then undergo an ionization phenomenon by the plasma, more or less effective depending on the first ionization energy of the chemical element being considered. This aspect will have important repercussions in the Section 5.2 results. The eroded particles migrate inside the plasma and after interacting with it, they re-settle on the internal surfaces of the magnetic confinement machines, giving rise to phenomena of self-sputtering, alteration of the surface morphology and implantation.

2.2 Modelling the plasma edge with SOLPS-ITER

In this subsection we are going to deal specifically with plasma modelling, first from the theoretical point of view, then entering into the merits of

what is implemented within the *SOLPS-ITER* code, the numerical code that was used for the on-board plasma simulations of this thesis work.

2.2.1 Kinetic models for plasma

We have already spoken in section Section 1.3 about the motion of a charged particle feeling the effect of an external electromagnetic field. The single particle dynamics, however, is not enough if we meant to determine a collective behavior of a plasma. We introduce a *kinetic description* that is a description that refers to a distribution

$$f_a(\vec{x}, \vec{v}, t)$$

in the *phase space*, which indicates the number of particles of the a population of plasma which at time t are located around the position $\mathrm{d}^3\vec{x}$ and around the velocity $\mathrm{d}^3\vec{v}$, and that the objective is to determine the evolution of this distribution function over time. The exact equation describing the evolution of the distribution function is the so-called *Klimontovich equation* [28]. If we then introduce a suitable mean operation that neglects the statistical fluctuations of the distribution, but in the right hand side, we obtain the so-called *Boltzmann equation* [29]:

$$\frac{\partial f_a}{\partial t} + \vec{v} \cdot \frac{\partial f_a}{\partial \vec{x}} + \frac{q_a}{m_a}\left(\vec{E} + \frac{\vec{v}}{c} \times \vec{B}\right) \cdot \frac{\partial f_a}{\partial \vec{v}} = C_a \tag{2.12}$$

Where with q_a and m_a the mass and the charge of the *a-th* particle under consideration were respectively indicated. The term C_a, which more generically could be calculated as

$$C_a = \sum^{b} C_{ab}(f_a, f_b)$$

instead it is called *collisional term*. When more plasma populations are present it introduces the effect of the collisions on the population a, represented by the f_a, of all the other populations b represented by the f_b and depends from small-scale fluctuations in the system. The collisional term, for this reason, cannot be calculated exactly, otherwise we would return to the problem of how the temporal evolutions of the fluctuations of the distributions $f_a(\vec{x}, \vec{v}, t)$ should be calculated. For this reason, it is appropriately modeled according to the situation. For example, it might be interesting in some situations to explore the *non collisional plasma* condition, setting $C_a = 0$ and obtaining the so-called *Vlasov equation*.

Within the scrape-off layer, surely, this kind of approximation cannot be done, since collisions and interactions within the SOL play a fundamental role in determining the conditions of the plasma. In this regard, we analyze two possible expressions for the collisional term, one that concerns Coulomb binary collisions between charged particles, the term of *Landau collision integral*, and the other that instead models collisions between neutral particles or a neutral particle and a charged one, the *Boltzmann collision integral*.

The Landau integral is obtained from an approximation known as *diffusion approximation* which takes the term collisional in the form of a *Fokker-Plank* operator. The dynamic systems of particles that can be described correctly by the Fokker-Planck equation must have a peculiar behavior: the trajectory of the individual particles must be similar to that of the particles of Brownian motion, that is, made up of weak deflections corresponding to weak variations of speed and only rarely deflections with large angles and strong variations in speed [30] [31]. In the specific case in which only Coulomb binary collisions between the populations a and b are considered, the Fokker-Plank collision operator is reduced to

$$C(f_a, f_b) = -\frac{q_a^2 q_b^2 \log\Lambda}{8\pi\epsilon_0^2 m_a}\frac{\partial}{\partial\vec{v}}\int \mathbf{U}\cdot\left(\frac{f_b}{m_a}\frac{\partial f_a}{\partial\vec{v}} - \frac{f_a}{m_b}\frac{\partial f_b}{\partial\vec{v}}\right) \tag{2.13}$$

where the $\log\Lambda$ is the Coulomb logarithm [32] [31] and

$$\mathbf{U} = \frac{v^2\mathbf{I} - \vec{v}\vec{v}}{v^3}$$

is the so called *scattering tensor*.

For what concerns the expression of the collisional term according to a treatment with the Boltzmann integral, to calculate the variation of the distribution function f_a due to collisions of the species a with the species b we use:

$$C(f_a, f_b) = \int \mathrm{d}\vec{v}_a \int \frac{\mathrm{d}\sigma}{\mathrm{d}\Omega}|v|\left[f(\vec{v}_b')f(\vec{v}_a') - f(\vec{v}_b)f(\vec{v}_a)\right]\mathrm{d}\Omega \tag{2.14}$$

where with $\vec{v}_a'$ and $\vec{v}_b'$ the velocities of the particles after the interaction were indicated while with $\vec{v}_a$ and $\vec{v}_b$ the previous ones. $\mathrm{d}\Omega$ can be written as $\mathrm{d}\Omega = \sin\chi\mathrm{d}\chi\mathrm{d}\epsilon$, with χ being the deflection angle and ϵ the scattering angle.

The description just made is certainly not of our help if, for example, we wanted to represent all the plasma particles and neutral particles, it would require too much computational effort. Particle dynamics must be calculated through a simpler model, for example we will see the *fluid model* in the next subsection.

However, the kinetic model can be used for another purpose by introducing the concept of *test particle*. A test particle is basically a computational object that represents a set of particles. The hypothesis is therefore that the behavior of these particles is well represented by the behavior of the single particle. If we want to simulate the behavior of a plasma population and we group the physical particles in a sufficiently large number of test particles, we can assume that the evolution of the original population subjected to certain conditions is the same as the behavior of the population of the test particles subjected to the same conditions. The computational cost can be greatly reduced. This concept, in addition to specific hypothesis, is at the basis of the so-called *Monte Carlo* methods, which aim to calculate the evolution of the population of test particles to solve Boltzmann-like equations. We will see in this Section 2.2 *EIRENE*

and in the Section 2.3 *ERO2.0* two examples of codes based on the Monte Carlo method.

2.2.2 Fluid models for plasma

As we said before, a description that is based only on a kinetic model requires too much computational effort to be used, except in rare cases. We now want to try to obtain a model that refers to a more global behavior of the fluid we are considering, a *multifluid description*. We proceed by defining fields that represent known physical quantities useful for a fluid description starting from the distribution function $f_a(\vec{x}, \vec{v}, t)$, for example density n_a, fluid speed $\vec{V}_a$ defined below, and using the equation (2.12) we obtain evolution equations for those fields and consequently evolution equations for the physical quantities they represent.

So let us start by introducing the physical quantities starting from the distribution function. These are all derived from the generic form:

$$\langle \psi(\vec{v}) \rangle_a \triangleq \frac{\int \psi f_a \mathrm{d}\vec{v}}{n_a} \tag{2.15}$$

By doing so, we have introduced an appropriate averaging operation on the infinitesimal element of fluid volume that takes into account the average behavior of the particles in this element, which is small enough to well describe each point of the fluid but large enough to be able to statistically represent all of the particles it contains. It is defined *order of the moment* as the exponent of the velocity on which the function $\psi(\vec{v})$ depends. We then proceed by replacing the generic field ψ inside the (2.12), we obtain an evolution equation for ψ and introducing also the physical quantities:

$$n_a(\vec{x}, t) = \int f_a(\vec{x}, \vec{v}, t) \mathrm{d}\vec{v} \tag{2.16}$$

$$\vec{V}_a(\vec{x}, t) = \frac{1}{n_a} \int \vec{v} f_a(\vec{x}, \vec{v}, t) \mathrm{d}\vec{v} \tag{2.17}$$

The velocity indicated with $\vec{V}$ represents the fluid velocity while the velocity $\vec{v}$ indicates the velocity of the single particle. We obtain the fluid equations for the ion population and the electron one, which consist of two continuity equations, two for the conservation of momentum and two for the conservation of energy:

$$\frac{\partial}{\partial t} n_i + \nabla \cdot \left(n_i \vec{V}_i \right) = S_{ni} \tag{2.18}$$

$$\frac{\partial}{\partial t} n_e + \nabla \cdot \left(n_e \vec{V}_e \right) = S_{ne} \tag{2.19}$$

$$\begin{aligned}\frac{\partial}{\partial t}\left(m_i n_i \vec{V}_i\right) + \nabla\cdot\left(m_i n_i \vec{V}_i \vec{V}_i\right) = \\ = -\nabla p_i - \nabla\cdot\mathbf{\Pi}_i + Z_i e n_i\left(\vec{E} + \frac{\vec{V}_i}{c}\times\vec{B}\right) + \vec{R}_i + \vec{S}_{m_i v_i}\end{aligned} \tag{2.20}$$

$$-\nabla p_e - e n_e\left(\vec{E} + \frac{\vec{V}_e}{c}\times\vec{B}\right) + \vec{R}_e = 0 \tag{2.21}$$

$$\begin{aligned}\frac{\partial}{\partial t}\left(\frac{3}{2}n_i T_i + \frac{m_i n_i}{2}V_i^2\right) + \nabla\cdot\left[\left(\frac{5}{2}n_i T_i + \frac{m_i n_i}{2}V_i^2\right)\vec{V}_i + \mathbf{\Pi}_i\cdot\vec{V}_i + \vec{q}_i\right] = \\ = \left(e n_i Z_i \vec{E} + \vec{R}_i\right)\cdot\vec{V}_i - Q_{ei} + S_E^i\end{aligned} \tag{2.22}$$

$$\begin{aligned}\frac{\partial}{\partial t}\left(\frac{3}{2}n_e T_e\right) + \nabla\cdot\left(\frac{5}{2}n_e T_e \vec{V}_e + \vec{q}_e\right) = \\ = -e n_e \vec{E}\cdot\vec{V}_e + \vec{R}_e\cdot\vec{V}_i + Q_{ei} + S_E^e\end{aligned} \tag{2.23}$$

Where with the generic quantities for the $a-th$ plasma population S_{na}, $\vec{S}_{m_a\vec{V}_a}$, S_E^a have been indicated respectively volume sources of particle, momentum and energy; with $p_a = n_a T_a$ the scalar pressure and with $\mathbf{\Pi}$ the viscous stress tensor; Q_{ei} is the thermal power exchanged between the electron and the ion population; $\vec{R}_a$ is the change in momentum due to the collision with all other plasma populations; with $\vec{q}_a$ the heat flux of the $a-th$ plasma population. We obtain quantities that depend on ever increasing orders of moments of the generic function ψ. Among these quantities there are those just listed, which we do not explicitly report at this point of the discussion.

As it is done for the collisional term of the Klimotovic equation, also for the fluid equations it is necessary to develop a suitable model to express the higher order as a function of density, velocity and temperature. *Closure expressions* of the fluid equations are necessary which, expressing the quantities written above in an explicit form depending on other quantities of the system, allow to obtain a number of equations equal to the number of unknowns and which therefore lead to a self-consistent description of the physical system under consideration. This is what Braginskii [33] did in his 1965 work. His work is based on the hypothesis that plasma is a two populations hydrogenic plasma, which is in a condition close to a *local thermodynamic equilibrium* and that therefore electrons and ions can be well described by Maxwellian distributions. He then introduces a first-order expansion of this distribution into the equations, thus assuming that each non-equilibrium condition can still be well described by a *quasi-Maxwellian* distribution. The main results of this theory are reported below and were taken from [34]. The directions $\parallel$ and $\perp$ indicate the directions parallel and perpendicular to the magnetic field respectively, here the SI system of units is used, instead of that of Gauss, used in the remaining part of the thesis.

As for the $\vec{R}_a$ the change in electronic and ionic momentum due to collisions:

$$\vec{R} \triangleq \vec{R}_e = -\vec{R}_i = en_e \left(\frac{\vec{j}_\parallel}{\sigma_\parallel} + \frac{\vec{j}_\perp}{\sigma_\perp} \right) - 0.71 n_e \nabla_\parallel T_e - \frac{3}{2} \frac{en_e^2}{\sigma_\perp B^2} \vec{B} \times \nabla T_e \quad (2.24)$$

Where we can identify two contributions, one due to the variation of momentum due to viscous effects $\vec{R}_u$ and the other due to thermal gradients $\vec{R}_T$:

$$\vec{R}_u = en_e \left(\frac{\vec{j}_\parallel}{\sigma_\parallel} + \frac{\vec{j}_\perp}{\sigma_\perp} \right) \quad (2.25)$$

$$\vec{R}_T = -0.71 n_e \nabla_\parallel T_e - \frac{3}{2} \frac{en_e^2}{\sigma_\perp B^2} \vec{B} \times \nabla T_e \quad (2.26)$$

With $\vec{j}_\parallel$ e $\vec{j}_\perp$ have been indicated respectively the two components of the electric current density $\vec{j}$

$$\vec{j} = e \left(z_i n_i \vec{V}_i - n_e \vec{V}_e \right) \quad (2.27)$$

and with $\sigma_\parallel$ and $\sigma_\perp$ the respective *classical electrical conductivities*. The terms $\vec{q}_a$, ion and electron thermal power fluxes, are:

$$\vec{q}_i = -\kappa_\parallel^i \nabla_\parallel T_i - \kappa_\perp^i \nabla_\perp T_i + \kappa_\wedge^i \frac{\vec{B}}{B} \times \nabla_\perp T_i \quad (2.28)$$

$$\begin{aligned} \vec{q}_e = -\kappa_\parallel^e \nabla_\parallel T_e - \kappa_\perp^e \nabla_\perp T_e - \kappa_\wedge^e \frac{\vec{B}}{B} \times \nabla_\perp T_e + \\ -0.71 \frac{T_e}{e} \vec{j}_\parallel - \frac{3}{2} \frac{T_e}{e \omega_e \tau_e B} \vec{B} \times \vec{j}_\perp \end{aligned} \quad (2.29)$$

Where we have indicated with $\kappa_\parallel^a$, $\kappa_\perp^a$ and $\kappa_\wedge^a$ the *classical thermal conductivities*, with τ_e the *basic collision time for electrons* and with ω_e the *electron gyrofrequency*. Also in this case we can recognize the two contributions, one due to friction and the other to the thermal gradients of the system:

$$\vec{q}_T^e = -\kappa_\parallel^e \nabla_\parallel T_e - \kappa_\perp^e \nabla_\perp T_e - \kappa_\wedge^e \frac{\vec{B}}{B} \times \nabla_\perp T_e \quad (2.30)$$

$$\vec{q}_u^e = -0.71 \frac{T_e}{e} \vec{j}_\parallel - \frac{3}{2} \frac{T_e}{e \omega_e \tau_e B} \vec{B} \times \vec{j}_\perp \quad (2.31)$$

The thermal power exchanged between the ion and electron populations is given by:

$$Q_{ei} = \frac{3 m_e}{m_i} \frac{n_e}{\tau_e} (T_i - T_e) \quad (2.32)$$

The viscous tress tensor Π, instead, is linked to the *strain rate tensor* W which in absence of external magnetic filed is given by:

$$W_{ij} = \frac{\partial V_\alpha}{\partial x_\beta} + \frac{\partial V_\beta}{\partial x_\alpha} - \frac{2}{3}\delta_{ij}\mathrm{div}(\vec{V}) \tag{2.33}$$

For a complete discussion even in the presence of external magnetic fields, see [33].

All of these coefficients are two-dimensional. This classic description works well in the parallel to the magnetic field direction, but not in the radial one. If we wanted to approximate plasma motion with a diffusion approximation, we would not find a good agreement with the experimental results. Then one may try to consider toroidal effects: this theory is called neoclassical. However, even in this way, a too low value is obtained for the diffusion in the radial direction, indicating that turbulence should be also considered.

Furthermore, the Braginskii model just written is valid only within the validity hypotheses of the Maxwellian description for the fluids considered. This means that the time variation of the average plasma quantities should be slow with respect to the collision time of the plasma particles and that the spatial variation of the same plasma quantities should be small over distances of the order of that travelled by the plasma particles between collisions. Precisely for this reason, in the sheath this description cannot be used and since the sheath (as seen in Section 2.1) is limited to a region very close to the wall, what is usually done is to impose the so-called *sheath boundary conditions* in correspondence of the target surfaces. These kind of boundary conditions correspond to impose Bohm criterion (2.7), at the sheath entrance, neglecting of what actually happens inside the sheath region.

Braginskii's model was later revisited by Braams [35] and Baelmans [34] within the framework of the code *B2.5*. This is one of the two modules of SOLPS-ITER code, one of the two codes used in this work. The most significant contribution given in Baelmans' doctoral thesis work was certainly that of generalizing the Braginskii plasma equations for descriptions in any coordinate system, deriving the equations as a function of the coefficients of the metric of the chosen coordinate system. As an alternative to the closure of Braginskii, it is worth mentioning the closure of Zhadanov, which allows to calculate corrections to the closure of Braginskii even in the presence of traces of impurities.

2.2.3 SOLPS-ITER: structure of the code

SOLPS-ITER [36] is the latest version of the SOLPS (*Scrape Off Layer Plasma Simulator*) code, the state of the art among plasma edge codes. As the name implies, it simulates the behavior of the scrape-off layer and a small part of the core plasma which together just constitute the *plasma edge*. The code aims to obtain the physical quantities of greatest interest for the study of edge plasmas: radial profiles of temperature, density and thermal fluxes reaching the wall and divertor. Certainly one of the biggest strengths of the code, is that of being able to keep all plasma species in the same simulation, in a self-consistent way.

The code consists of two modules, one is the *B2.5* package and the other is the *EIRENE* module. With B2.5, as already mentioned in the previous subsection, different plasma species can be simulated and each plasma species is treated with a multi-fluid description based on the model described at the end of the previous paragraph. For completeness, refer to the code manual [37]. The code distinguishes the main species from a series of impurities, such as *seeding gases* (typically noble gases that are pumped to the divertor to low down the temperature and heat flows from the plasma) or the atoms generated by sputtering from the wall: the code is able to adapt the coefficients of the model to take into account the effects of these on the behavior of the main species.

The second main module of SOLPS-ITER is the *EIRENE* module [38], a Monte Carlo-like method that solves a *Boltzmann equation* and deals with the transport of neutral atomic and molecular species from the wall and with the interaction between these species and the plasma. The code launches neutral particles from the boundary surfaces and follows the trajectory of neutral atomic and molecular species until they are completely absorbed in the plasma.

Now let's see briefly how the code is structured and what are the main inputs. We will provide an overview only on what was needed to proper face the simulations contained in this thesis work. The specific setup of these routines will be provided in Chapter 3.

2.2.4 Inputs and workflow of the code

To begin, let's take a look at how code works in the Figure 2.4, taken from [39]:

- **DivGeo** it constitutes an interface that allows the user to prepare the main inputs of the code. It requires data on the poloidal section of the machine to be simulated and a configuration file for the magnetic equilibrium of the machine referred to a specific instant in time. An important thing to know is that the plasma volume simulated by the B2.5 module does not include the wall, because it can only intersect it at the ends of the flux surfaces, where the divertor is placed.
- **Carre** is the mesh generating program for B2.5 [40]. Starting from the DivGeo outputs, it generates a rectangular mesh starting from the magnetic field lines, aligning two sides of the mesh cells along the magnetic field lines. Carre does also the transformation between curvilinear and rectangular mesh cells and the grid resolution can be chosen by the user.
- **Triang** is the program used to build the triangular mesh for B2.5-EIRENE coupled mode, using the input from DivGeo and Carre. This grid extends allover the 2D-poloidal projection of the vacuum chamber.
- **B2.5** is one of the two main modules of which the SOLPS-ITER code is composed together with EIRENE. As mentioned before, this module is the one that solves the multi-fluid equations for plasma transport. This block is written in `FORTRAN 90` and is based on a *finite volume discretization*. The order in which the equations are solved at each step of the code is as follows: volumetric and surface

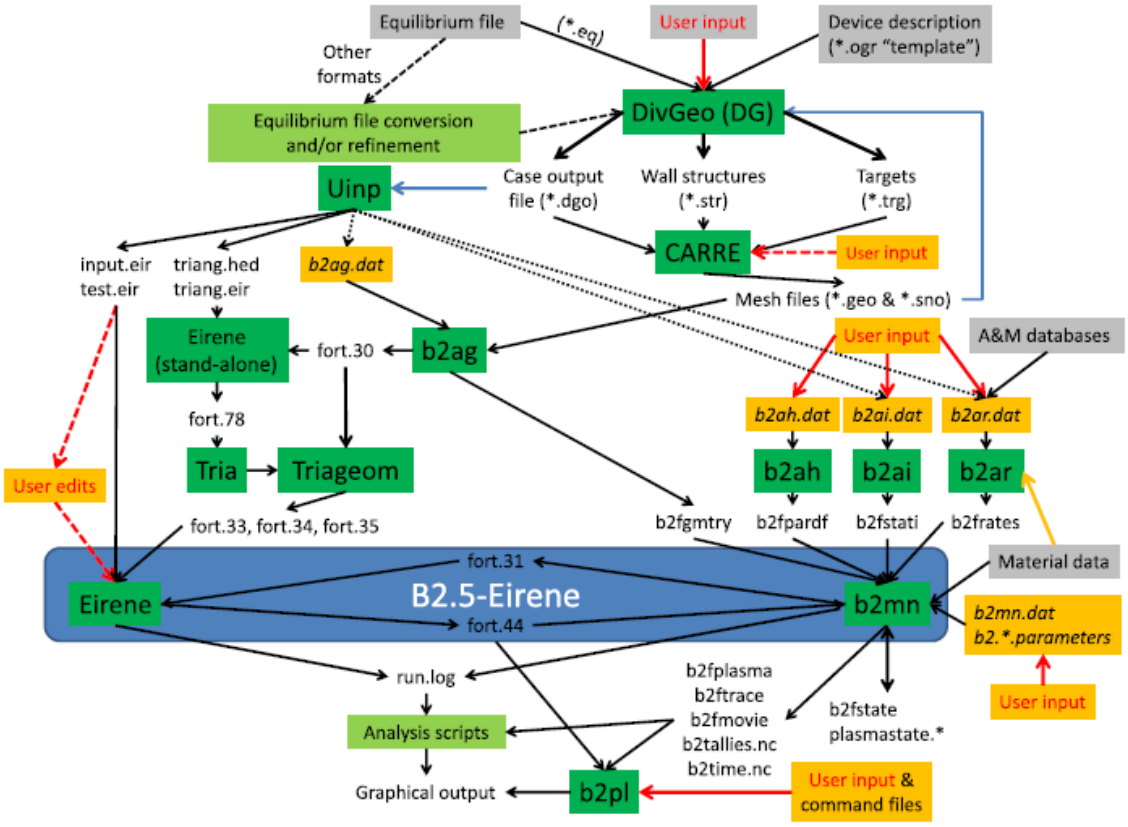

Figure 2.4: SOLPS-ITER workflow [39].

source terms are computed, solving for momentum conservation, continuity, energy conservation and finally again for the continuity equation. The above procedure is repeated for a sufficient number of internal iterations to relax the equation solutions before proceeding to the next time step, or external iteration. In this work we solved the problem for stationary solutions of the equations, that is, solutions where there was no longer variation of the simulation parameters between successive iterations of the code. Among the various B2.5 routines there are a series of files that are written in `ASCII` format that are editable by the user, containing specific information on the simulation setup, which we are now going to list.

- **b2ag.dat** contains data on the geometry of the problem, providing information like the number of cells in the grid, the symmetry of the problem and the mesh file to be read.
- **b2ah.dat** contains information about the different species that are considerd, boundary conditions and transport coefficient specifications.
- **b2ar.dat** specifies the ranges of densities and temperatures for atomic physics tables, taken from different atomic physics packages. The default option is the use of ADAS (Atomic Data and Analysis Structure)[41].
- **b2ai.dat** sets up the default initial plasma states, specifying a homogeneous value for the electron and ion temperature,

and neutral and ion densities.

- **b2mn.dat** is the main input file of B2.5 and determines its functionning. Among other things, it contains the switches required to obtain a given behaviour of the code.
- **b2.boundary.parameters** specifies the boundary segments present in the simulated region and the corresponding boundary conditions for each of the balance equation.
- **b2.neutrals.parameters** specifies data and parameters regarding the treatment of neutral species.
- **b2.numerics.parameters** specifies the settings for the numerical methods used for the solution of the equations in the different regions of the domain.
- **b2.transport.parameters** specifies the values for the anomalous transport coefficients.
- **b2.sources.profile** specifies arbitrary radially and axially dependent external source profiles. The types of sources that can be defined are particle source, momentum source, electron heat source, ion heat source, electric charge source and non-ambipolar electric particle source.

- **EIRENE** is the Monte Carlo part of the code that solves the transport part of the neutral species in 3D. Also written in `FORTRAN 90`, when coupled to B2.5, one of the three dimensions, the toroidal one, is neglected and treated appropriately. The main input required by this package is a formatted file called input.dat, produced by DivGeo and can also be edited by the user. The file is made up of fifteen blocks. To get into the specifics of how the input.dat file is divided, refer to the [38]. In the context of my thesis, in particular, we worked on evaluating the effect of the parameters contained in blocks 4 and 5, which are related to the reactions between species, as will be described in the next paragraph.

2.2.5 Rate coefficients and databases

As we have said so far, the presence of neutral atomic species in the plasma produce a large number of possible reactions between the plasma species. These reactions, as we have said, are computed by the EIRENE module through a Monte Carlo method. The data for the calculation of the reaction rates are taken from databases by means of interpolations on density and/or energy and/or temperature of the reagents. They provide the values of the reaction rates. These databases are available to the code and can be set in the `input.dat` file. Once the main plasma species has been set in DivGeo, the choice of the set of reactions that will be implemented by the code is made automatically by the code itself, it can be modified by the user, who can manually change the set of reactions and the databases from which to take data for interpolation. This implementation mode requires a good knowledge of all the inputs needed by the code, so usually the default reaction setup is almost never questioned by the user.

Now we do not go into the merits of how the rates are calculated by the code, but it is important to know that there are different types of databases. Fits are available both as a function of temperature alone or function of temperature and energy or density of the reacting species,

depending on whether the data is dependent on these quantities or not. In fact, for the electrons it seems to be sufficient to use a fit of the temperature alone, while for the heavier ions it is necessary to use a fit with two input variables. From databases we can extract different quantities and we will use for this explanation the notation used by the code, because this will help us in referring to these quantities. We can obtain interaction potentials (`H.0`), total cross-sections (`H.1`), rate coefficients (`H.2`, `H.3` and `H.4`) and momentum- (`H.5`, `H.6` and `H.7`) and energy-weighted (`H.8`, `H.9`, `H.10`) rate coefficients, respectively, as well as some supplementary data fits (`H.11` and `H.12`). For our purposes, it is important to know that if one uses a rate coefficient for compute a certain reaction, the result is to have the number of reactions occurring in the unit time, while if one combines the rate coefficient and the energy-weighted coefficient for a given reaction obtains the energy rate for that specific reaction that takes into account both the probability of the reaction to occurr and the energy distribution of the products. This type of reaction will be very useful to evaluate the energy distribution of ions and electrons after *electron impact ionizations*, with the possibility of including in the balance excited states of the neutral atom after the collision. The rates used in this thesis are:

- **H.1**: cross-section vs. energy $\sigma(E)$, $[cm^2]$ (used for charge exchange processes)
- **H.2**: rate coefficients vs. temperature $\langle\sigma(v)v\rangle(T)$, $[cm^3/s]$ (used for elastic collisions processes)
- **H.3**: rate coefficient vs. temperature and energy $\langle\sigma v\rangle(E,T)$, $[cm^3/s]$ (used for charge exchange processes)
- **H.4**: rate coefficient vs. temperature and density $\langle\sigma v\rangle(n,T)$, $[cm^3/s]$ (used both for radiative recombination and electron ionization processes)
- **H.10**: energy-weighted rates vs. temperature and density $\langle\sigma vE\rangle(n,T)$, $[cm^3/s\cdot eV]$ (used for electron ionization processes including the neutral atom excited states)

2.3 Modelling the plasma-wall interaction and impurity transport with ERO2.0

After talking about the physics of the main plasma-wall interaction phenomena in Section 2.1, let us now treat how they are implemented within the *ERO2.0* code [27], used in this thesis work to simulate plasma erosion of the chamber walls of the linear GyM machine, the self-sputtering from the eroded particles and the transport and re-deposition of the eroded particles within the considered machine. ERO2.0 is a numerical code written in C^{++} language, divided mainly into two parts: the first one which studies the erosion of plasma-exposed materials while the second one the transport of the eroded particles. In this section, we will first focus on the description of the models implemented by ERO2.0 to solve both the plasma-wall interaction and the transport of eroded particles and then we will focus on the structure of the code and inputs.

2.3.1 Erosion

In this section we focus on the description of the model implemented by ERO2.0 in the field of physical sputtering, chemical sputtering will not be treated from now on because in this thesis it has not turned out to be a relevant physical phenomenon. As already said, ERO2.0 has as its first objective that of calculating the yield of physical sputtering $Y(E_{in}, \theta_{in})$. For this calculation, the code has several possibilities at its disposal. For example, it can use databases generated by codes such as *SDTrimSP*, through preliminary sheath tracing simulations, or even using experimental data fitting formulas, such as the *Eckstein fit formula* [42]. Since this model is the one used in this work, we briefly illustrate it. The code calculates $Y(E_{in}, \theta_{in})$ as a function of the impact energy E_{in} of the incident particle and the angle of incidence θ_{in}.

Eckstein formula is given by:

$$Y(E_{in}, \theta_{in}) = Y(E_{in}, 0) A(E_{in}, \theta_{in}) \tag{2.34}$$

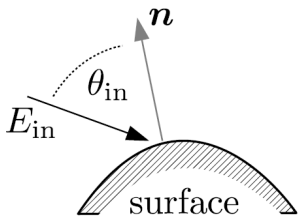

Figure 2.5: Definition of the projectile incidence angle θ_{in} relative to the surface normal $\vec{n}$.

Where the two contributions $Y(E_{in}, 0)$ e $A(E_{in}, \theta_{in})$ can be identified, named respectively *normal factor* and *angular factor*. The normal incidence factor depends on four fit parameters $(\lambda, q, \mu, E_{th})$ and is given by

$$Y(E_{in}, 0) = q s_n^{\mathrm{Kr-C}}(\epsilon_L) \frac{(E_{in}/E_{th} - 1)^{\mu}}{\lambda/\omega - (E_{in}/E_{th} - 1)^{\mu}} \tag{2.35}$$

Notice that the sputtering yield becomes zero when $E = E_{th}$, giving to E_{th} the meaning of sputtering threshold. $s_n^{\mathrm{Kr-C}}(\epsilon_L)$ is the nuclear stopping power for the Kr-C potential:

$$s_n^{\mathrm{Kr-C}} = \frac{0.5 \ln(1 + 1.2288\epsilon_L)}{\omega} \tag{2.36}$$

where

$$\omega = \epsilon_L + 0.1728\sqrt{\epsilon_L} + 0.008\epsilon_L^{0.1504} \tag{2.37}$$

the reduced energy

$$\epsilon_L = E_{in} \frac{M_2}{M_1 + M_2} \frac{a_L}{Z_1 Z_2 e^2} \tag{2.38}$$

with M_1, M_2 being the masses and Z_1, Z_2 the atomic numbers of the projectile and the target atoms respectively, a_l the Lindhard screening length given by:

$$a_l = \left(\frac{9\pi^2}{128}\right)^{\frac{1}{3}} a_B \left(Z_1^{\frac{2}{3}} + Z_2^{\frac{2}{3}}\right)^{-\frac{1}{2}}, \qquad a_B = 0.0529177 nm \tag{2.39}$$

and a_B the Bohr radius.

The angular factor $A(E_{in}, \theta_{in})$ is a function of three energy-dependent fit parameters (b, c, f) and is given by

$$A(E_{in}, \theta_{in}) = \xi^{-f} e^{b(1-1/\xi)} \tag{2.40}$$

with

$$\xi = \cos\left[\left(\frac{\theta_{in}}{\theta^*_{in}}\frac{\pi}{2}\right)^c\right], \quad \theta^*_{in} = \pi - \arccos\sqrt{\frac{1}{1+E_{in}/E_{SB}}} \tag{2.41}$$

Note that the sputtering yield is not a function of the charge of the ion, even if the ions make a more relevant contribution to the sputtering. This depends on the fact that ions, unlike neutrals, can be accelerated by the electric field in the sheath.

The emission of neutral particles is approximated with the *Thompson-Sigmund distribution* [43] which can be written as:

$$\frac{\mathrm{d}Y}{\mathrm{d}E} \propto \frac{E}{E + E_{SB}^{1+\alpha}} \tag{2.42}$$

with α fit parameter, while the emission angle is given by an *over-cosine law*:

$$\frac{\mathrm{d}Y}{\mathrm{d}\Omega} \propto \cos^y(\theta) \tag{2.43}$$

with y fit parameter.

2.3.2 Impurity transport

ERO2.0 calculates the trajectory of the eroded particles starting from a background plasma configuration and other inputs such as the magnetic field that we will see more specifically in the next Chapter 4. Eroded particles are always treated in approximation of test particles. The trajectory cannot be calculated with the *guiding center approximation* because the characteristic quantities of the motion of the particles (i. e. Larmor radius) are not sufficiently small with respect to both the variations in plasma quantities and the variations in the magnetic field. The Boris algorithm is used to resolve the gyromotion of the particles [44] [45]. As discussed in [45], the Boris method is the de-facto standard for full-orbit simulations of magnetized plasmas due to its excellent accuracy even for an arbitrarily large number of time steps. In particular, the method conserves energy exactly when there is no electric field. In the presence of an electric field, the numerical error is bounded. The Boris method is able to correctly reproduce effects present in tokamaks such as banana orbits ([46] p. 130) and the Ware pinch effect [47], in contrast to e.g. the 4^{th} order Runge-Kutta method, which fails at larger numbers of time steps due to accumulation of numerical error.

However, the motion of particles within the magnetic field is only part of the story. To deal with the transport of the eroded particles into the plasma, we also need to calculate the interactions they make with the plasma. We have already spoken in Section 2.2 about the kinetic model

and the function of the collisional term. Referring to (2.12) we briefly explain the model implemented by ERO2.0.

ERO2.0 calculates the collisional term for impurities using the *test particle approximation*. This approximation assumes the concentration of impurities (test particles) to be low enough that they do not influence the distribution of the *background* main plasma species. Furthermore, the test particles do not interact with each other and do not affect the electro-magnetic fields. In the following, subscript p will indicate the test particle while the subscript b the background plasma. The kinetic equation for a test particle becomes:

$$\frac{\partial f_p}{\partial t} + \vec{v} \cdot \frac{\partial f_p}{\partial \vec{x}} + \frac{q_p}{m_p}\left(\vec{E} + \frac{\vec{v}}{c} \times \vec{B}\right) \cdot \frac{\partial f_p}{\partial \vec{v}} = C(f_p, f_b) \tag{2.44}$$

In the case of small angle scattering, which dominates in the plasma, the collision term may be written as a Fokker-Planck term (also this derivation, taken from [27], by means of correctness is reported in the SI system of units):

$$C\left(f_p, f_b\right) = -\sum_i \frac{\partial}{\partial v_i}\left(K_i f_p\right) + \frac{1}{2}\sum_{i,j}\frac{\partial^2}{\partial v_i \partial v_j}\left(D_{ij} f_p\right) \tag{2.45}$$

where K_i and D_{ij} are components of the so-called drift vector and diffusion tensor. They are functionals of the background plasma distribution f_b and the the Trubnikov potentials ϕ and ψ:

$$K_i = \left(1 + \frac{m_p}{m_b}\right)\Lambda \frac{\partial \phi(\vec{v})}{\partial v_i}, \qquad \phi(\vec{v}) = \int \mathrm{d}\vec{v'} \frac{f_b(\vec{v'})}{|\vec{v} - \vec{v'}|} \tag{2.46}$$

$$D_{ij} = \Lambda \frac{\partial^2 \psi(\vec{v})}{\partial v_i \partial v_j}, \qquad \psi(\vec{v}) = \int \mathrm{d}\vec{v'} |\vec{v} - \vec{v'}| f_b(\vec{v'}) \tag{2.47}$$

The numerical constant Λ is given by:

$$\Lambda = \lambda \frac{Z_p^2 Z_b^2 e^4}{4\pi\epsilon_0^2 m^2} n_b \tag{2.48}$$

where λ is the Coulomb logarithm, ϵ_0 is the dielectric constant, Z_p, Z_b, m_p and m_b are the charge states and masses of test and background ions, and n_b is the density of background ions. By inserting the collision term (2.45) into the kinetic equation (2.44) and rearranging the terms, the kinetic equation is brought into the form of a Fokker-Planck equation:

$$\frac{\partial f_p}{\partial t} = -\sum_i \frac{\partial}{\partial x_i}\left(v_i f_p\right) - \sum_i \frac{\partial}{\partial v_i}\left[\left(\frac{\partial}{\partial t} v_i + K_i\right) f_p\right] + \frac{1}{2}\sum_{i,j}\frac{\partial^2}{\partial v_i \partial v_j}\left(D_{ij} f_p\right) \tag{2.49}$$

The Fokker-Planck form allows a particularly simple Monte Carlo procedure for solving the kinetic equation. For calculating the coefficients K_i and D_{ij} in equation (2.45), the background plasma distribution f_b is

assumed to be a Maxwellian shifted to the background flow velocity v_b and with ion temperature T_b:

$$f_b(\vec{v}) = \left(\frac{m_b}{2\pi k_B T_b}\right)^{3/2} \exp\left(-\frac{m_b(\vec{v}-\vec{v}_b)^2}{2k_b T_b}\right) \tag{2.50}$$

The numerical procedure for simulating the test particle transport in ERO2.0 works as follows: at the beginning, an ensemble of test particles in phase space $(\vec{x};\vec{v})$ is defined, and then the phase-space trajectory of each individual test particle is advanced by repeatedly applying the Boris method together with the Monte Carlo iteration.

2.3.3 ERO2.0: inputs and workflow of the code

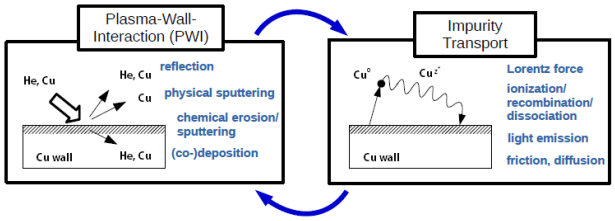

Figure 2.6: Example of workflow: illustration of the general workflow of the ERO2.0 code, based on the example of a copper surface exposed to a helium plasma, image adapted from [27].

Figure 2.6 illustrates the general workflow of the ERO code. We have already talked specifically about the two blocks at the beginning of this Section 2.3. For a target surface exposed to a plasma, ERO can calculate PWI processes, subsequently ERO creates an ensemble of computational test particles, which represent the eroded target material that enter the plasma as impurities. It then computes the trajectories and the interactions with the background plasma. If required for obtaining steady-state conditions (as in our case), this procedure can be repeated. In each new step, the additional plasma-wall interaction caused by the test particle impact from the previous step is considered when creating the new test particle ensemble. Also, the change in material composition from the previous time step may be taken into account.

The inputs required by ERO2.0 are the 2D and 3D geometry of the internal surfaces of the machine being simulated, the background plasma configuration, which includes the temperatures and densities of all plasma species, the magnetic field configuration and some boundary conditions including particle fluxes to the walls of the simulated machine. We will go to better analyze these aspects in the Section 4.1.

2.4 Overview on the reference literature context

To conclude the chapter, our goal here is to give an overview of the reference literature context of this work. The name of plasma-wall interaction refers to a very wide range of physical processes and consequently there are many areas of research that deal with specific aspects of this vast topic, both from experimental and from modelling point of view. There are also different machines and systems used to study these phenomena, as we have seen in Chapter 1. In this framework we have also clarified

the role that linear machines have, for example for the study of plasma exposures in fusion like conditions. Among the possible applications, the study of helium plasmas interacting with materials has become and will become an interesting research field, also with reference to what has been underlined for the first phase of ITER operation. We illustrate this area of interest, possibly highlighting the open points. Or by not highlighting them and leaving them as motivations and aims of this work.

2.4.1 Experimental investigations of plasma edge physics and plasma-wall interaction

The behavior and the morphological evolution of materials of fusion interest in thermonuclear plasma regimes have been investigated: in particular, the attention has been placed on tungsten because it is the first candidate material to be used in the divertor. The research, in this sense, has tried to understand the phenomenon of the formation of *nanostructures* that lead to the deterioration of the material: for surface temperatures $T_{surf} < 900 - 1000K$ the formation of *nanobubbles* has been observed [48][49][50], which is an energy threshold phenomenon for incident particles with saturation trend. At higher surface temperature, in the range $900 - 1900K$, and for $E_{ion} > 20 - 30eV$, the formation of a *fibreform* nanostructure, called *fuzz*, has been observed in a large variety of experiments [51][52][53] also in the framework of introducing a tungsten-vanadium alloy [54]. The conditions for fuzz to occur are expected to be reached in ITER in the divertor region [55], and tungsten fuzz has been observed even in nowadays tokamaks [56]. These experiments are mostly carried out with linear plasma devices, such as PISCES-A and PISCES-B [19], MAGPIE [20], PSI-2 [17], NAGDIS [18] and STEP [57]. Also, with PSIEC experimental investigations of plasma-wall interaction were carried out [58]. Also at GyM [21] tungsten fuzz formation has been investigated [59].

In addition to the formation of nanostructures, as part of the interaction of tungsten with helium plasmas in linear machines, the effect of helium and argon plasmas in the *retention* of deuterium in tungsten was also investigated [60], the *arcing* phenomena in the context of the plasma interaction of helium with tungsten and carbon [61] at NAGDIS and the effect of a helium plasma on a high conductivity graphite foam [62] in PSI-2.

2.4.2 Modelling activities related to the experimental ones

Another direction of plasma-wall interaction research, which takes place in parallel with the experimental activity, is the coding one. Each numerical code is written for the purposes of modeling the research field in which it is placed, and each code has been developed with specific purposes and intentions. Each code has specific strengths, but it is necessary to keep in mind the application limits. The application of numerical codes to the context of tokamaks is certainly the common approach in the literature, but recently the option of applying numerical codes for linear machine studies has also been evaluated.

For example, in the context of linear plasma devices, at PSI-2 some interaction studies between helium and chromium plasmas were carried out with the aim of validating the predictions made with the first version of the ERO2.0 code: ERO [63].

Since the release of version 2.0 of ERO [27], which, unlike the previous version, allows to simulate the transport of eroded particles on macroscopic volumes, the interest in simulating magnetic confinement machines raised [64]. In this direction, several simulations have been carried out using the ERO2.0 code to achieve surface erosion and depositions both in tokamaks such as JET [65], ITER [8], and in linear machines [66] [67] [68].

For what concerns SOLPS-ITER, the adaptation of this code that allows to use the code on a linear machine has only recently been implemented [69] [70], before there was no standard procedure that would allow you to easily launch a simulation and many steps of its preparation had to be implemented manually modifying the files produced automatically by the code routines. The work that was done made it possible to adapt the code written for tokamaks to the cylindrical geometry of a linear machine. Then in [22], the effect of the variations of some parameters on Argon *non-hydrogenic plasmas* was simulated (including only charge states Ar and Ar^+) as the main plasma species and implementing ionization and recombination reactions of Ar and Ar^+. Now that the adaptation of SOLPS-ITER to linear machines is available, taking into account the experimental context described above, the modelling of helium plasmas as the main plasma species with the state-of-art code SOLPS-ITER is of great importance. To the best of our knowledge, the only work in the literature on this topic is [71].

In addition to the applications of a single code, works are also beginning to be seen that go in the direction of studying the coupling between codes. In this context, the study done in the very recent work [72] carried out with the Proto-MPEX [73] machine is also of particular relevance. This study aimed to quantitatively determine the unwanted sputtering of the walls of the chamber of the machine used for the exposure of samples, due to the formation of a sheath caused by the presence of the radiofrequency source for the plasma. In all plasma-wall interaction works the question of the influence of impurities eroded by the walls on the results is often neglected a priori, while in this thesis work we place ourselves in this unknown area by taking a first step in the direction of giving a method for modeling and predicting these effects.

As for the interest in coupling the two numerical codes SOLPS-ITER and ERO2.0, it has been mentioned for example, both in the 2016 EUROfusion report [74] and subsequently in the [22] work. The work by J. Romazanov et al. [75] constitutes a first coupling of SOLPS-ITER and ERO2.0. It was made in the context of tokamaks and discusses the issue of extrapolating plasma parameters from one code to the other and the impact it has on ITER chamber beryllium erosion estimates. In the context of linear machines, such a coupling has never been done, either with helium plasmas or with any other type of plasma.

2.5 Motivations and aim of the work

As we have seen there are some open aspects such as the limited use of SOLPS-ITER with linear machines. Even more limited is the exercise of coupling them to study the erosion and transport properties of the eroded impurities. There are even more open elements if one considers helium plasmas for various reasons, because even the simulation of helium plasma with SOLPS-ITER uses elements still coming from the use made of them in the tokamak framework.

In this work was faced the problem of understanding whether the default SOLPS-ITER setup for tokamak's helium plasmas was as accurate as possible from the point of view of considered plasma reactions also in the linear device context. The important results of the carried-out analysis was subsequently included in the code changes and became the current standard setup. This is work is presented in the Chapter 3.

The works mentioned in the linear device context of application of ERO2.0, together with perhaps very few others, constitute the only examples of this code's application for the study of surface morphology. None of these works used the ERO2.0 code for global modelling to study the erosion and transport of impurities in the context of linear machines, if by global simulation we intend to explore the ability of ERO2.0 to study the transport and re-deposition of impurities over lengths and volumes much greater than those typical of the morphological evolution of surfaces (like in [75]). In this thesis, the second aim was to understand how to properly configure the ERO2.0 code in the field of linear machines. This is work is presented in the Chapter 4.

After this two intermediate steps, the third and final goal was to couple the SOLPS-ITER plasma edge code with the ERO2.0 code, for the study of erosion and eroded impurities transport in the GyM linear machine, in the context of helium plasmas. We remark that a coupled simulation of this type in the context of linear plasma devices has not yet been published in the literature. This is work is presented in the Chapter 5.

Analyzing helium plasma reactions and their contributions with SOLPS-ITER

3

3.1 Adapting SOLPS-ITER to the linear plasma device GyM 47
3.2 Updating the choice of the databases 51
3.3 Analyzing the reactions and their contributions 53
3.4 Summary 60

Here the analysis on the helium plasma reactions' setup with the SOLPS-ITER code is presented. This piece of work first required to learn how to generate the necessary inputs to the code with the recent developed procedure, also mentioned in Section 2.4. This adaptation is briefly illustrated in Section 3.1. Then, from the Section 3.2 we start presenting this work results. As underlined in the motivation section, in this chapter it was addressed the issue if the default SOLPS-ITER setup for tokamak's helium plasmas was as accurate as possible also in the linear device context. So in Section 3.2 and in Section 3.3 comparisons were made on the choice of databases and the set of reactions implemented by SOLPS-ITER to see the effect they have on the results of the simulations. This work has clarified what was the recommended setup for helium plasmas in linear machines and a summary of the results of this chapter is reported in Section 3.4.

3.1 Adapting SOLPS-ITER to the linear plasma device GyM

Let's start by briefly illustrating the path followed in preparing the simulations. This work was carried out in the context of this master thesis [76] and PhD activity of [70]. First of all it is necessary to understand the orientation of the reference system, and then move on to the calculation of the magnetic field for the construction of the mesh oriented according to the magnetic field lines.

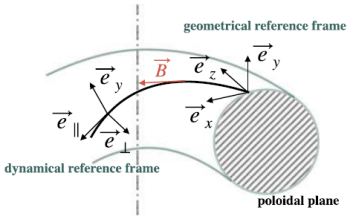

Figure 3.1: Illustration of the dynamical and geometrical reference frame in toroidal geometry.

3.1.1 Coordinate systems

The two coordinate systems on which the SOLPS-ITER code is based are the *dynamic system* $(\vec{e}_\parallel, \vec{e}_y, \vec{e}_\perp)$, which follows the magnetic field lines and the reference system written for a reference poloidal section: the *geometrical system* $(\vec{e}_x, \vec{e}_y, \vec{e}_z)$. Assuming the symmetry in the toroidal direction z, as mentioned in Section 2.2, the equations are solved by SOLPS-ITER in the second reference system working with a two-dimensional problem, taking into account the drift which instead depend on the direction z. The two reference systems are represented in the Figure 3.1, together with the Figure 3.2 which represents the mesh constructed in the geometric reference system by SOLPS-ITER.

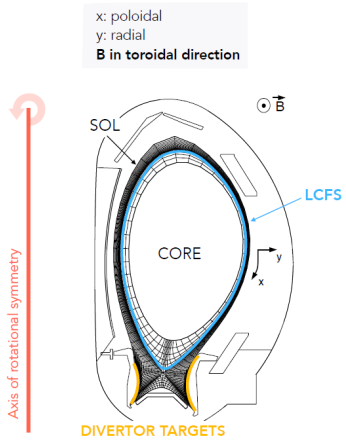

Figure 3.2: Example of the construction of the mesh in a poloidal section in the geometrical reference frame.

To readjust the SOLPS-ITER mesh to the cylindrical geometry of a linear machine, the section of the cylindrical machine identified by the plane (Z, R) has been treated as the section of a tokamak, where the Z axis is aligned with the central axis of the cylinder of the machine and R is the radial coordinate of the machine. In the Figure 3.3 we clearly see the analogy between the two sections of the tokamak and the top view of the

linear machine section. We also see represented an example of a mesh built starting from the magnetic field. How it was built will be briefly explained below. Here we focus on the considerations that can be made related to this choice of coordinates to model GyM.

The reference system used to refer to the linear machine is the system $(\vec{e}_R, \vec{e}_\Phi, \vec{e}_Z)$. For comparison, also the coordinates of the geometric reference system of the toroidal case are reported. As a first consideration, we note the fact that in a tokamak-type magnetic field, the direction where the main component of the magnetic field lies, is the toroidal one, which in the geometric reference system is in the direction identified by the $\vec{e}_z$ unit vector. In the case of a linear machine, the magnetic field is oriented according to the central axis of the linear machine, so along the axis that in the figure is indicated with the capital letter Z. Any component of the magnetic field in the direction perpendicular to the (Z, R) plane, would be instead the analog of the z direction of the tokamak. In the geometric reference system of the tokamak, on the other hand, the Z direction of the linear machine would coincide with the $\vec{e}_x$ direction. The SOLPS-ITER equations, as we said earlier, are written in two dimensions (x, y) while the expressions of the drifts are calculated taking into account the magnetic field component B_z in the direction z, which in the case of linear geometry it is null, so we can say that a limit of this description is the fact that we cannot calculate the plasma drifts in linear geometry. Let's now take a closer look at how the quadrilateral mesh for B2.5 was constructed.

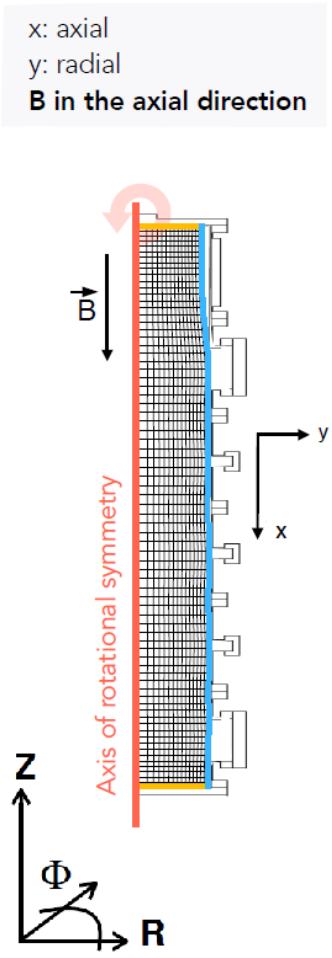

Figure 3.3: Example of the construction of the mesh in the geometrical reference frame in GyM.

3.1.2 Building 2D meshes from the magnetic field

We said in Section 1.4 that the magnetic field configuration is calculated starting from the solution of the equation of Grad-Shafranov (1.15): $\psi(Z, R)$ is the flux function, j_z is the azimuthal current density, indicated in this case with j_Φ and it includes contributions coming from the plasma and from the external magnetic field coils. The first contribution in this case is negligible, since we are in linear geometry, so j_Φ only depends on the known external current, that for our case is $600A$. From the computation of $\psi(Z, R)$ (represented in Figure 1.24), it is possible to compute the magnetic field in the azimuthal B_Z and radial direction B_R:

$$B_Z = \frac{1}{R}\frac{\partial \psi}{\partial R} \qquad B_R = -\frac{1}{R}\frac{\partial \psi}{\partial Z} \tag{3.1}$$

Now, once the solution has been calculated, the magnetic field lines that are inside one half of the occupied volume of the linear machine chamber are taken. The mesh is constructed by taking the magnetic field line close to the wall (radially speaking) and a mesh is constructed: equally spaced in the azimuthal direction (Z), while in the radial direction (R) following the trend of the iso-ψ lines. The generated mesh is $64x12$ in size. We then obtain the mesh represented in Figure 3.4. Moreover, around the mesh, so-called *guard cells* have been generated, of very small extension compared to the other cells. These guard cells are required by the code in order to work correctly. Starting from this mesh, a file in `ASCII` format

has been created, readable by the B2.5 `b2ag` routine, which contains information on the coordinates of the cell points.

3.1.3 Setting up the configuration with DivGeo

We will not go into the specific issue of the procedure required by the code, we will limit ourselves only to a summary of the conceptual steps to understand which specifications have been fixed in the setup of our work. Once the creation of the geometry file has been completed, we proceed by running the `b2ag` routine, which produces a first geometry file readable by the code containing the constructed mesh. After this, we run the `DivGeo` program. The procedure with `DivGeo` requires you to also specify a file that contains the magnetic reconstruction of tokamak equilibrium, as already mentioned in Section 2.2. In order to make the program work also in the linear geometry, this step is performed by giving input to the procedure a dummy tokamak balance file which will then have no effect on the output produced by `DivGeo`.

With the `DivGeo` program various things are then specified, including all the information (for example material and temperature) regarding the internal surfaces of the machine. They include: targets, walls, pumping surfaces and puffing surfaces for the introduction of the neutral gas which will then constitute the plasma. The information regarding the size of the plasma and the power introduced from the outside are then provided to the program. Finally, also the created mesh is inserted, in order to create the output required by `Uinp` to properly generate the `input.dat` file when launched. In this regard it is necessary to make another clarification: having been made the hypothesis of axial symmetric geometry, it is not possible to model the pumping surfaces as they really are. The code assumes as if the pumping surfaces were lateral openings of the chamber, obtained by making the revolution of their projection on the 2D (R, Z) plane of the semi-cylinder. Even the gas puffing surfaces are actually located in only one point of the geometry, but the code transforms this input into a ring of gas puffing. For the sake of completeness, let us now summarize in the Table 3.1 the main parameters set in `DivGeo` common to all the simulations done in this work.

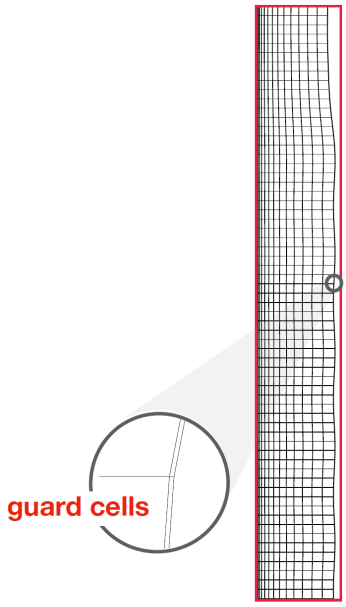

Figure 3.4: Generated 64x12 SOLPS-ITER mesh used in this work.

DATA	VALUE
Coil current	$600A$
Puffed flux	$1.12 \cdot 10^{19} atm/s$
Puffed gas Temp.	$0.03eV$
Core width	$0.1m$
Aborption coeff.*	0.018
Wall Temp.**	$0.029eV$
Wall Material	Fe
Total Power	$540W$
Plasma species	He

Table 3.1: Summary of the main input parameters set in the DivGeo program, common for all the simulations done in this thesis work.
* probability of the incident particles to be absorbed by the pump
** thermal particles from the wall are modeled as a Maxwellian distribution with $T = T_{wall}$

Once this phase has been completed, the code is automatically able to produce all the necessary files to be launched, such as the mesh for EIRENE and the `input.dat` file which we will talk about shortly.

3.1.4 Limits of the standard setup and the need to improve helium reactions

As we have already said, the code is able to produce the `input.dat` file on the basis of the specifications provided by the user with the `DivGeo` program. In the `input.dat` file the specifications useful for the correct functioning of the EIRENE part are contained as written in Section 2.2. Among these, in blocks 4 and 5 are contained the reactions that constitutes the possible events of the scenario to be treated with the Monte Carlo method. So here, basically, all the possible reactions between the plasma species in the scrape-off layer should be listed, or in any case there should not be missing any reaction that makes a significant contribution in determining the behavior of the plasma. Here is the original setup of the code (we have listed both the physical reaction and the corresponding code with which is implemented, this notation will help us in the discussion):

- Elastic scattering:
  $He + He \longrightarrow He + He$

```
0 AMMONX H.2  R-HE-HE  EL
```

- Electron ionization:
  $He + e^- \longrightarrow He^+ + e^- + e^-$

```
0 HYDHEL H.2  2.3.9    EI
```

- Radiative recombination:
  $He^+ + e^- \longrightarrow He$

```
0 ADAS   H.4  acd96    RC
1 ADAS   H.10 prb96    RC
```

Where the first item indicates the *database* from which to extract the needed data, `H.2`, `H.4` and `H.10`, as specified in Section 2.2 are used to indicate the type of data extracted from the database: for the first and the second we recall that they are rate coefficients, and the last one is an energy rate coefficient. Third element stands for the specific reaction to be found in the databases, and the last two letters indicate the type of the reaction: `EL` = *elastic scattering*, `EI` = *electron ionization*, `CX` = *charge exchange*, `RC` = *radiative recombination*. Now, we see that in the original code setup, in the helium ionization reaction

$$He + e^- \longrightarrow He^+ + e^- + e^- \tag{3.2}$$

the possibility that the helium atom could remain in an excited state after the electron impact ionization, was not included.

$$He + e^- \longrightarrow He^* + e^- \tag{3.3}$$

This is due to the fact that in the reaction statement only the rate coefficient (H.2 or H.4) is present and the corresponding energy rate coefficient (H.10) for that process is not associated (an example of H.4 and H.10 coupling can be seen instead in the the radiative recombination reaction). And since the temperature in GyM is low enough for which the degree of ionization of the plasma is very low (density of neutral atoms of the

order of $\approx 10^{19} atms/m^3$ against the density of $He^+ \approx 5 \cdot 10^{19} atms/m^3$) it was considered necessary to also include this type of reaction, since it directly involves the species dominant in the simulated LPD chamber.

This type of reaction was not originally included among the reactions implemented by default by SOLPS-ITER because in tokamaks the temperature is much higher (remember that it is of the order of tens of keV in the core plasma) and therefore the presence of neutral species compared to ionized ones is certainly less than in this case. Furthermore, helium in tokamaks, has always been treated in the simulations with SOLPS-ITER only as an impurity and therefore in that case a refinement work on the helium reactions was not necessary.

In an attempt to include the excitation contribution of neutral helium atoms, further investigations were required in the reaction setup. This investigation was carried out on two fronts, the first was to understand if the databases chosen by default to extract the rates coefficients were actually the most suitable. The second was to understand which reactions to insert in the list of possibilities contained in blocks 4 and 5 of the `input.dat` file.

3.2 Updating the choice of the databases

As we stated in the concluding part of Section 3.1, here we move in the direction of clarifying the *database* choice. This investigation was made necessary by the fact that HYDHEL, used to obtain the rate coefficient for the electron ionization reaction, is the oldest database among those in the list above and it was not possible to couple the reaction rate coefficient H.2 with an energy rate coefficient from HYDHEL to compute neutral excitations. Therefore two more recent databases have been taken into account, ADAS and AMJUEL, which contains also the energy rate coefficients. Moreover, ADAS and AMJUEL interpolate the data with respect to density, which HYDHEL does not do. Before adding the energy part, a comparison was made between the three rate coefficients provided by the three databases. Three simulations have been launched where the standard setup for the elastic scattering reactions and radiative recombination was held, but the database from which to take the reaction rate for the electron ionization was varied. In the three simulations, the electron heat loss (EHL) due to interaction with neutrals is computed as a constant energy loss per collision event equal to the He ionization energy ($-24.58eV$). The three simulations' setup are summarized in this Table 3.2:

Table 3.2: Summary of the reactions implemented in run 0.S, run 1.S and run 2.S

RUN	EL	EI		RC
	reaction	database	reaction	reaction
0.S	AMMONX	HYDHEL	H.2 2.3.9	ADAS H.4 acd96
1.S	H.2 R-HE-HE	AMJUEL	H.4 2.3.9a	ADAS H.10 prb96
2.S	(same for all)	ADAS	H.4 scd96	(same for all)

For these comparisons, in order to catch the information we needed it has been sufficient to evaluate mean parameters: in the first Figure 3.5

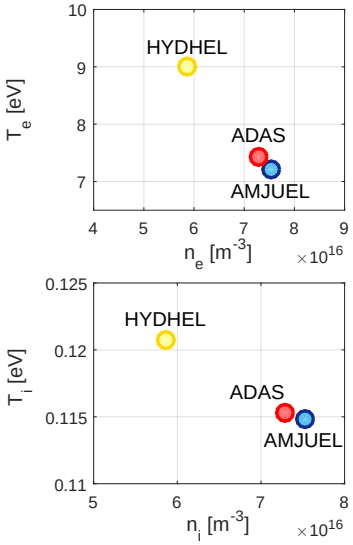

Figure 3.5: Mean volume temperature and density plots, for electron population (first figure T_e, n_e) and ion (second figure T_i, n_i), database comparison.

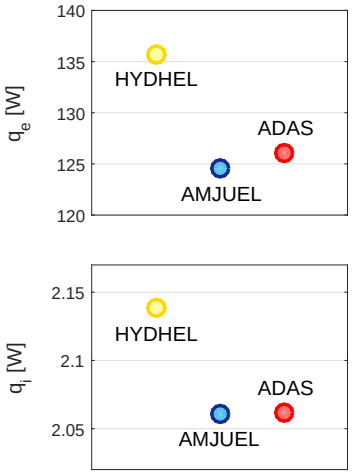

Figure 3.6: Heat fluxes at the West target, for electron population (first figure q_e) and ion (second figure q_i), database comparison.

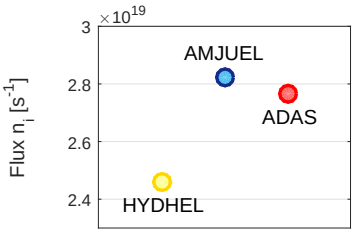

Figure 3.7: Ion particle flux at the West target *flux* n_i, database comparison.

have been plotted on two graphs the values of the ion and electrons temperatures (T_e, T_i $[eV]$) and densities (n_e, n_i $[m^{-3}]$) averaged over GyM's chamber volume. Representing temperatures and densities on the same graph it allows us to look at two parameters at a time. In the second Figure 3.6 the values of the thermal fluxes (q_e, q_i $[W]$) at the surface that the code recognizes as the *West target*. For us it coincides with the upper basis of the cylinder of Gym which, to be clear, is the one towards which the radiofrequency source is located. In the last Figure 3.7 is represented the value of the ion flux, always calculated at the West target.

What can be observed from these figures is that AMJUEL and ADAS produce almost the same results and this can be seen in practically all the plotted results. HYDHEL seems to overestimate the electron and ionic temperature values, resulting in a lower density for both populations. This is due to the fact that the product of density and temperature is related to the internal energy of the system and in the three cases it should be about the same, so if the temperature increases, the density decreases and vice versa. HYDHEL, due to these temperature discrepancies, also overestimates the heat fluxes at the West target. Finally, since the ionic density estimated by HYDHEL is lower, this has repercussions in having a lower ionic particle flux at the West target. HYDHEL however was the default database chosen by `Uinp` for the implementation of the ionization reaction and the importance of changing the default database was certainly a first result of the analysis made.

We can also infer that the difference in results may be due to a lower accuracy of the data available from the database at low temperatures. In fact, at low temperatures, the reaction rate decreases very quickly and if we look at the electron ionization reaction rate obtained with HYDHEL, we can see the difference of about a factor of 2 with respect to the fit of the database obtained with ADAS (or AMJUEL). They are represented in Figure 3.8.

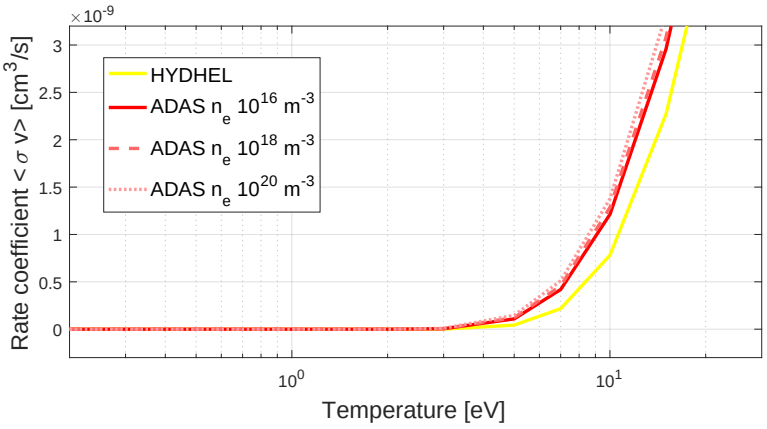

Figure 3.8: Rate coefficients from ADAS and HYDHEL databases

For a matter of completeness, it has to be said that also an important difference between ADAS and AMJUEL databases exists: AMJUEL gives the coefficient of a polynomial interpolation between datas, while ADAS requires an interpolation within the data. This is one of the reasons because the two databases gives different (but close to each other) results.

To conclude this analysis let us see also the 2D contour plots of the three

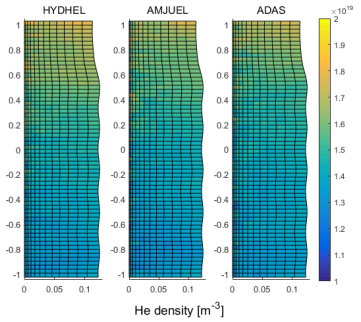

Figure 3.9: Neutral He density 2D contour plot: the effect of the choice of the database

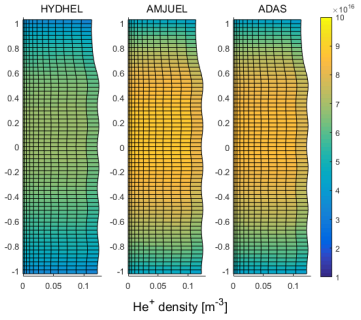

Figure 3.10: Ion He^+ density 2D contour plot: the effect of the choice of the database.

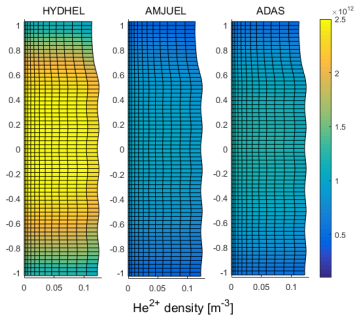

Figure 3.11: Ion He^{2+} density 2D contour plot: the effect of the choice of the database.

atomic populations taken into account in this analysis: He, He^+ and He^{2+}. Also here it can be observed that the obtained results are almost the same for ADAS and AMJUEL, while differences are observed if HYDHEL is chosen as the reference database. This can be a further effect of the higher electron temperature obtained in the *run 0.S* which affects the lower electron density and this results in lowering down He^+ and rising up He^{2+} densities with respect to other two cases.

3.3 Analyzing the reactions and their contributions

After clarifying the use of the databases for the ionization reaction rate, before arriving at the inclusion of the energy-rate coefficient for this reaction, we also carried out a more in-depth investigation on the other reactions present in the code's default list. This analysis was carried out by manually modifying the set of standard reactions present in the `input.dat` file. From the physical point of view, the four reactions considered in the analysis are:

- elastic scattering:
  $He + He \longrightarrow He + He$
- electron ionization with excitation of neutrals:
  $He + e^- \longrightarrow He^+ + e^- + e^-$
  $He + e^- \longrightarrow He^* + e^-$
- charge exchange:
  $He^+ + He \longrightarrow He + He^+$
  $He^{2+} + He \longrightarrow He + He^{2+}$
- radiative recombination:
  $He^+ + e^- \longrightarrow He$

Compared to the standard reaction setup, the charge exchange reaction between the neutral population and the two ionized helium populations was also added to the list. The analysis done can be divided into three parts: elastic scattering, charge exchange and electron ionization. Firstly we analyzed the effect that *turning on and off* the contribution given by elastic scattering has on the results. The original setup (listed in Section 3.1) was used for this analysis. This choice was motivated by the fact that, before modifying the original reaction set, we wanted to confirm the importance of the elastic scattering reactions in the standard reference context. Once these issues were clarified and the choice of the reference database for the ionization reactions updated, it was possible to analyze the effect of the charge exchange reactions, manually switching their contribution on and off. The *a priori* reason for the inclusion of this reaction is still linked to the high presence of neutral particles in the system. In this case the ionization was treated also including the results obtained on database comparisons. So ADAS rates were used but without including the possibility of the excitation of the neutrals, analyzed in a dedicated part. The latter reaction has never been completely switched off because it makes no sense to ask whether it should be included in the balance or not because the answer is definitely affirmative. In summary, the three objectives were:

- To evaluate the importance of the elastic collisions in the standard setup
- To include the updating of the database and and see the effect of the charge exchange
- To include the neutral excitation in the electron impact ionization process

3.3.1 The effect of elastic collisions

For convenience, we report the reactions of the standard setup:

- Elastic scattering:

```
0 AMMONX H.2  R-HE-HE  EL
```

- Electron ionization:

```
0 HYDHEL H.2  2.3.9    EI
```

- Radiative recombination:

```
0 ADAS   H.4  acd96    RC
1 ADAS   H.10 prb96    RC
```

And here below there is the summary of the simulations that has been implemented in order to investigate the weight of the elastic collisions:

RUN	EL	EI	CX	RC
0.S	✓	✓	×	✓
3.S	×	✓	×	✓

As previously said in the introduction, the first one contains the standard set of reactions implemented by default by SOLPS-ITER, the second contains the same set of reactions but turning off elastic collisions.

Let us analyze the obtained results. We reported the same physical quantities used for the previous comparison and the dot colour reflects the database from which has been extracted the electron ionization datum. It can be seen from the graphs that the effect of the elastic collision is only slightly significant. In fact, turning off the elastic collisions causes a decrease in the electron and ion temperatures of $\approx 1\%$ that corresponds to a little increase in their density (also here of about$\approx 1\%$). It can be seen that also other quantities, as for temperatures and densities, have not being changed so much by the elastic scattering reactions.

This can be due to the fact that ions and neutrals are at about the room temperature, and so thermal energy cannot be exchanged. In order to have a much more impacting contribution from elastic collisions to the physical quantities in the system, it could be interesting to study the same two set of reactions at higher relative energies between ions and neutrals, so in a condition where we are closer to that of tokamaks.

To conclude the discussion, let us also look at the 2D contour plots of the neutral densities in Figure 3.15. Also here it can be observed that turning off elastic collisions produces very slight increases of the neutral density. In this situation we can say that probably, even if we had used the ADAS or AMJUEL database for the ionization calculation, we would

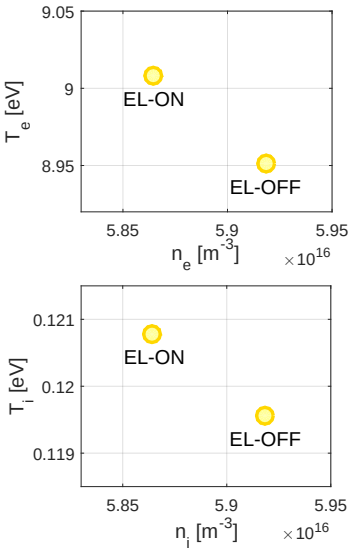

Figure 3.12: Mean volume temperature and density plots, for electron population (first figure T_e, n_e) and ion (second figure T_i, n_i), elastic scattering effect.

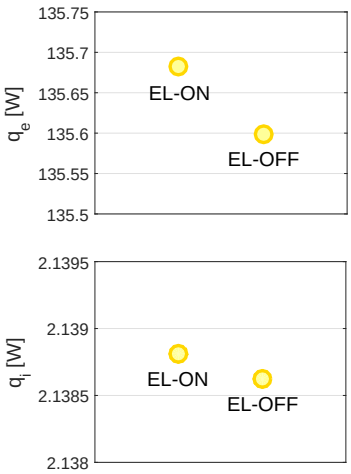

Figure 3.13: Heat fluxes at the West target, for electron population (first figure q_e) and ion (second figure q_i), elastic scattering effect.

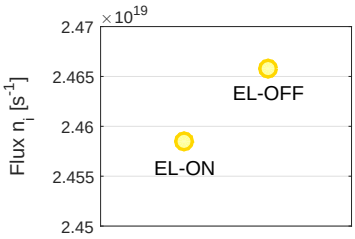

Figure 3.14: Ion particle flux at the West target *flux* n_i, elastic scattering effect.

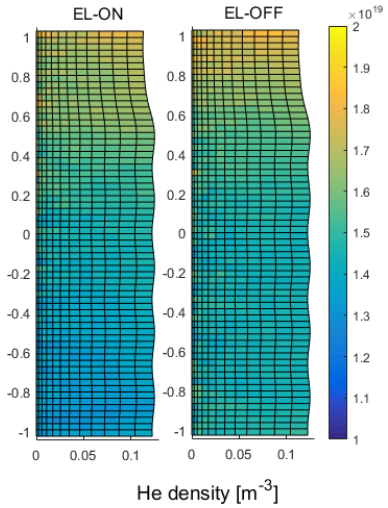

Figure 3.15: Neutral He density 2D contour plot: the effect of elastic scattering

have obtained the same results. All the more so due to the fact that HYDHEL, as we have seen in our case, tends to overestimate the ionic temperature.

3.3.2 The effect of charge exchange

In this analysis the effects of charge exchange process have been investigated. To make the comparison we ran two simulations, employing the same set of reactions and switching off the contribution of charge exchange in one of the two simulations. For this comparison, we selected ADAS as database for electron impact ionization. The reaction setup is summarized:

- Elastic scattering:

```
0 AMMONX H.2  R-HE-HE  EL
```

- Electron ionization:

```
0 ADAS   H.4  scd96    EI
```

- Charge exchange:

```
0 HYDHEL H.1  5.3.1    CX
1 HYDHEL H.3  5.3.1    CX
2 HYDHEL H.1  6.3.1    CX
3 HYDHEL H.3  6.3.1    CX
```

- Radiative recombination:

```
0 ADAS   H.4  acd96    RC
1 ADAS   H.10 prb96    RC
```

In Table 3.3, we reported the identification number of the simulations, i.e. *run 2.S* and *run 4.S*, and the corresponding set of reactions. Note that the *run 2.S* is the same run that we analyzed in the Section 3.2.

RUN	EL	EI	CX	RC
2.S	✓	✓	×	✓
4.S	✓	✓	✓	✓

Table 3.3: Summary of the charge exchange simulations.

Let us start analyze the results from the same quantities always reported in these analysis. Overall, we can say that the introduction of charge exchange, unlike what has been said for elastic scattering, has a considerable influence on the results. Let's start with the scatter plot represented in Figure 3.16: the inclusion of the charge exchange reactions has the effect of decrease the electron temperature (from $7.4eV$ to $6.9eV$) and considerably increasing plasma density of about 40% (from $7.3 \cdot 10^{16} m^{-3}$ to $10.4 \cdot 10^{16} m^{-3}$). On the ion side, instead, it can be seen that both the quantities of density and temperature increase. The ionic temperature rises from $0.115eV$ to $0.134eV$ ($\approx 17\%$). This indicates that the internal energy of the ion population has increased.

The cause of the increase in ion density is to be identified in the activation of the *collisional drag* force between the ionic and neutral population due to the charge exchange. The existence of this force causes the ions to slow down during the approach to the walls in the pre-sheath region and therefore increases the confinement time of the system. This fact is confirmed by the decrease of the ion particle flux to the targets, while the increase of the ionic heat flux is linked to the increase of the temperature of the ions. By increasing the ion density, they also have more collisions with the electrons and to gain energy, lowering electron temperature. We remember in fact that it is through the electronic population that the radiofrequency source introduces energy into the system. The decrease in the electron temperature affects also the electron heat flux.

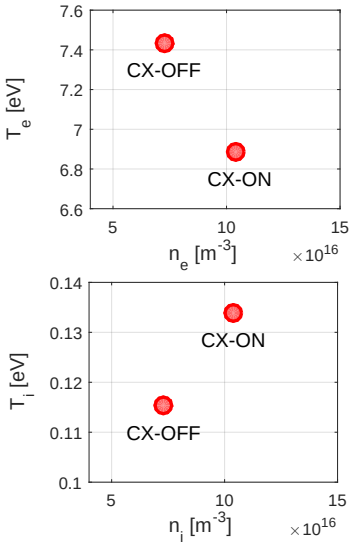

Figure 3.16: Mean volume temperature and density plots, for electron population (first figure T_e, n_e) and ion (second figure T_i, n_i), effect of charge exchange.

Even looking at the density and temperature distributions of the neutral population in Figure 3.19 it can be seen that the temperature rises slightly at the extremes.

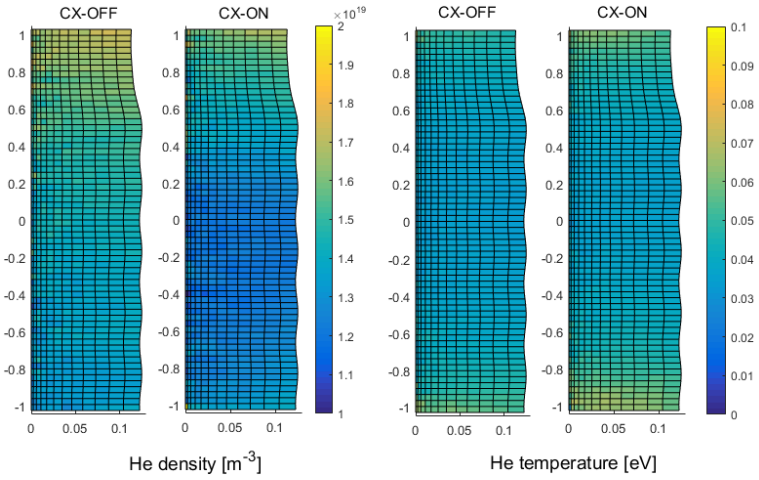

Figure 3.19: Neutral He density and temperature 2D contour plot. Effect of the charge exchange.

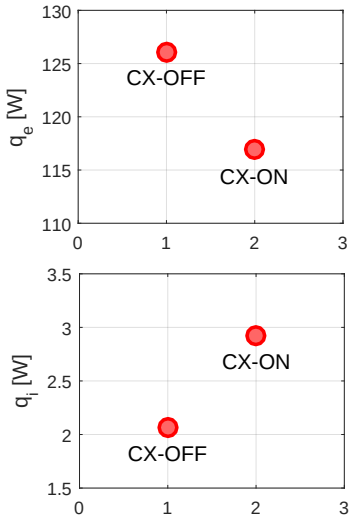

Figure 3.17: Heat fluxes at the West target, for electron population (first figure q_e) and ion (second figure q_i), effect of charge exchange.

If we then observe the density distributions of the charged populations, we can easily see how the increase of the confinement time of the ionic population has repercussions in a greater degree of ionization of the plasma, this fact is connected with the decrease in the density of the neutral population.

To conclude, we can say that the effect of activating the charge exchange processes is not negligible and these reactions should be included in the default reactions set. Also here, we say that it could be very interesting

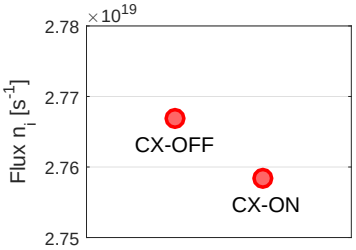

Figure 3.18: Ion particle flux at the West target *flux* n_i, effect of charge exchange.

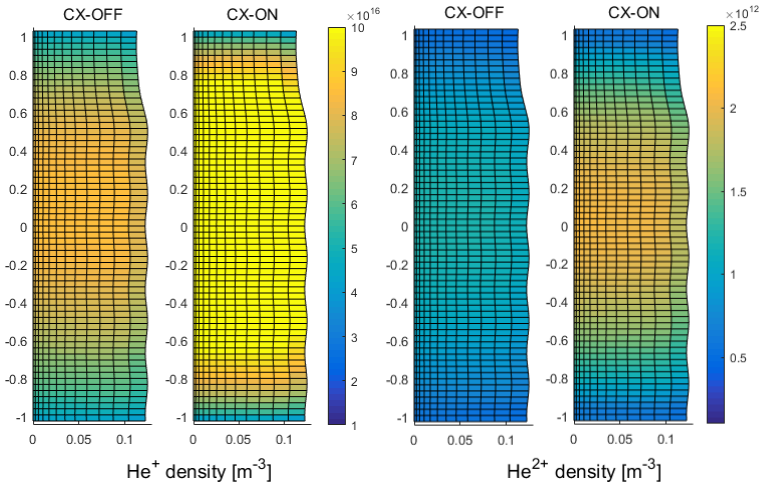

Figure 3.20: He^+ and He^{2+} density 2D contour plots. Effect of the charge exchange.

to study the effect of these reactions also for higher relative energies between ions and neutrals.

3.3.3 Including neutral excitations in the electron impact ionization process

In this section comparisons have been made between ADAS and AMJUEL databases, with the aim of including together with neutrals ionization also the excitation of the neutrals after the electron collision. As discussed in section Section 3.2, the HYDHEL database does not include this reaction, hence it has not been considered for this study. In trying to include this contribution as well, the two different databases were compared. If the same result were obtained, we would have confirmed the success of the process.

Before proceeding with the discussion of the simulation results, we will address from the technical point of view how the code includes the electron impact excitation reaction. In block 4 of the *input.dat* file there is a parameter ([38] p. 118), indicated with the variable `DP`. It gives you the possibility to include an additional constant contribution to the energy loss, given by the associated rate in the process you are describing. Considering an electron impact reaction with a neutral atom, the energy lost in the process by the electron is the combination of two terms. On the one hand, the electron can extract another electron from the neutral helium atom, and the energy lost in the process corresponds to the neutral atom ionization potential (in this case for helium $\approx -24.587eV$). On the other hand, the electron can excite the neutral atom. Neutral de-excitation leads to the emission of a photon. For AMJUEL, it is clear from the description of the energy-weighted rate coefficient that in the data H.10 contains the sum of both energy contributions just described. For ADAS it seemed that only the excitation energy contribution were contained. So the energy lost by the electron to ionize the neutral atom, had to be entered in the DP parameter by setting DP = -24.587 eV. This type of syntax at the time of the simulation was not accepted by the code that returned a syntax error message. Consequently it was necessary to work with the developers of the code so that negative values of DP could

be set and then do some checks to understand what was the correct way to declare the reaction with ADAS if we wanted to include ionization and excitations. To do this last step, two ways of doing this have been identified: either set `DP = 0` (if ionization was already included by the database) or set `DP = -24.587 eV`. Here we then proceed as usual, first reporting the reactions implemented in this section:

- Elastic scattering:

```
0 AMMONX H.2  R-HE-HE  EL
```

- Electron ionization:

```
0 SEE THE TABLE BELOW
```

- Radiative recombination:

```
0 ADAS   H.4  acd96    RC
1 ADAS   H.10 prb96    RC
```

The simulations' scheme for this section is the following Table 3.4:

Table 3.4: Summary of the electron ionization simulations.

RUN	**EL**	**EI**				**CX**	**RC**
		database	reaction		DP		
			ionization	energy			
1.S	✓	AMJUEL	H.4 2.3.9a	-24.587eV	0	×	✓
5.S	✓	AMJUEL	H.4 2.3.9a	H.10 2.3.9a	0	×	✓
2.S	✓	ADAS	H.4 scd96	-24.587eV	0	×	✓
6.S	✓	ADAS	H.4 scd96	H.10 plt96	0	×	✓
7.S	✓	ADAS	H.4 scd96	H.10 plt96	-24.587eV	×	✓

In the two cases run 1.S and run 2.S the energy loss per collision is constant, set to -24.587 eV, according to the syntax used for the simple rate coefficients of H.2 and H.4 type: the meaning is that the rate H.4 gives as a result the number of ionizations per unit time unit volume and for every ionization event the loss of energy is the one specified by the value -24.587 eV. The other three runs: run 5.S, run 6.S and run 7.S has been declared using the H.10 energy rates trying to include also electron energy losses due to neutral excitations. The energy loss is no more constant and it is taken from the databases indicated. DP was set to 0 and to -24.587 eV in run 6.S and run 7.S respectively, the reason is that one mentioned above. Let us look at the results.

Figure 3.21 represents the total radiation energy from the neutral atoms. It can be observed that in the cases in which the excitation have not been taken into account (run 1.S and run 2.S) the energy coming from neutral de-excitation is null. What can also be observed is that the value assumed by this quantity in the run 6.S is not correct if we wanted to include both excitations and ionizations, because it is positive, while this value is a loss of energy for the neutral atoms. Another comment that confirms this can be done looking at this second plot, 2D electron temperature among the five cases:

Temperature lowers between run 1.S case and the run 5.S and this is correct, because the energy that the neutrals gain to reach the excited state lowers the electron temperature, this confirms that AMJUEL works correctly. Accordingly to this reasoning, it can be observed that this happens also

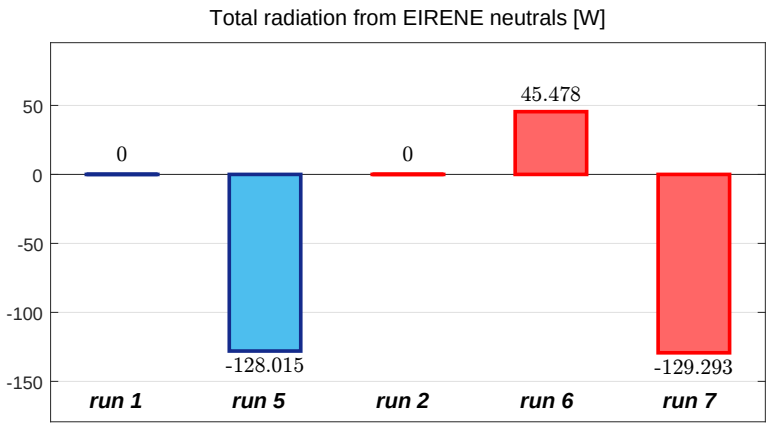

Figure 3.21: Total radiation from neutrals.

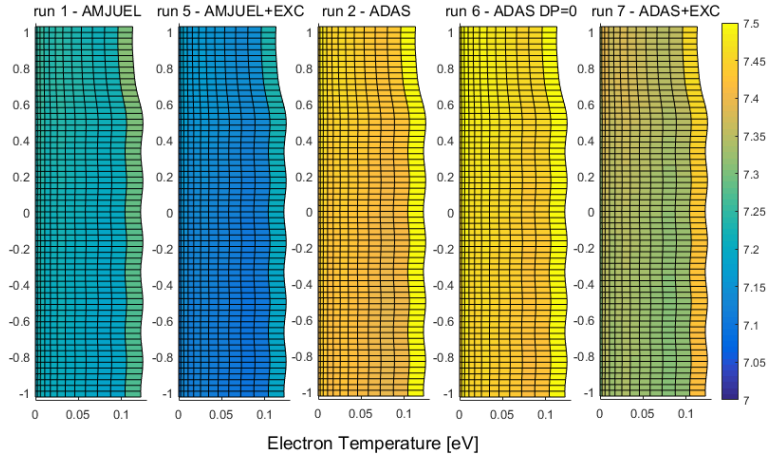

Figure 3.22: Electron temperature 2D contour plot, effect of neutral excitation.

for run 2.S and run 7.S cases, in which the electron temperature decreases as the excitation is activated in the system. Run 4.S shows instead a slightly higher temperature than its reference case, the case of run 2.S. This is nonphysical because electron temperature is expected to decrease if excitation of neutrals is turned on. In the following run 6.S will be removed from the comparisons: the correct statement of the desired reaction is represented by the run 7.S case.

The reason why the results obtained with run 6.S are wrong is related to the value of DP = 0. To compute the energy radiated from the neutrals, the code first computes the energy loss for the electrons and then adds the ionization energy value *shifting up* that value. But if you do not subtract the value of DP (= -24.587eV) for each ionization to the electrons' energy before computing neutral radiated energy, the values of energy lost by the neutrals due to radiation result shifted upwards, so much so that it becomes positive. This work was of crucial importance in refining the usage of ADAS database and now the possibility of choosing a negative value of DP has been standardized in the official version of SOLPS-ITER code. Let us now analyze the other plots:

All the physical quantities represented in Figure 3.23, Figure 3.24 and Figure 3.25 shows a decreasing trend if excitations are included. In

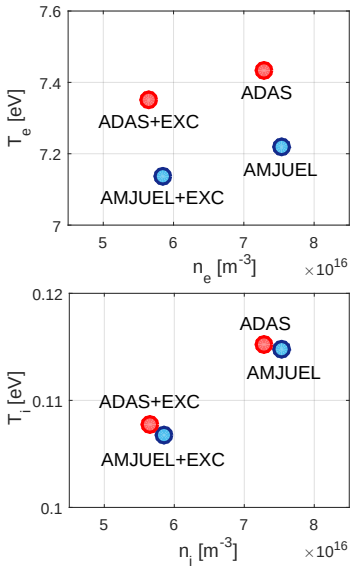

Figure 3.23: Mean volume temperature and density plots, for electron population (first figure T_e, n_e) and ion (second figure T_i, n_i), effect of neutral excitation.

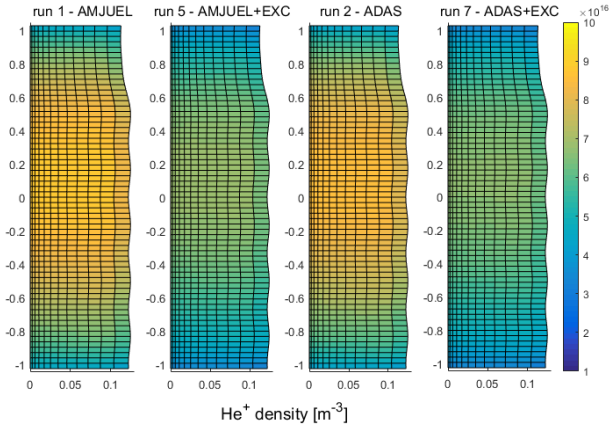

Figure 3.26: He^{+} density 2D contour plot, effect of neutral excitation.

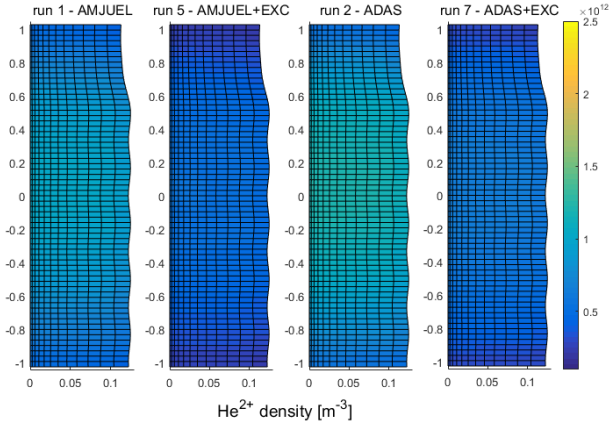

Figure 3.27: He^{2+} density 2D contour plot, effect of neutral excitation.

particular, this result was expected for electron temperature, which in this case lose more energy due to the excitations of the neutrals. This is reflected in the lower temperature also reached by the ions: since the electrons are less energetic, they draw less energy from them. The effect of this fact reflects also on the density distributions of the ions populations, represented in the following 2D contour plots:

It can be seen that the effect of switching on the excitations results in a slight decrease of the degree of ionization of the plasma and this is consistent with the fact that the electrons now lose energy also to excitate the neutrals, as well as to ionize them.

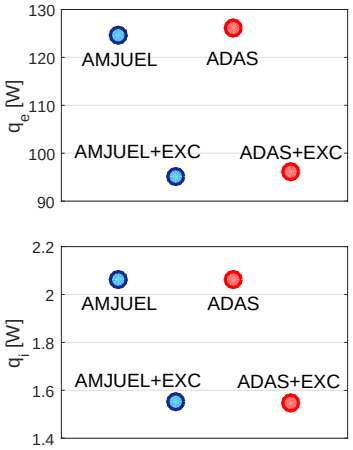

Figure 3.24: Heat fluxes at the West target, for electron population (first figure Q_e) and ion (second figure Q_i), effect of neutral excitation.

3.4 Summary

We summarize the results obtained with this analysis. First of all we understood that the database chosen by default by the code to calculate the reaction rate coefficients on the ionization reactions had to be updated with a more accurate database at low temperatures. We understood that the elastic collisions in the system do not play a significant role due to the low temperatures. The charge exchange effect between populations has the effect of activating collisional drag for the ions, this has a particularly relevant effect on the plasma and so it is recommended to include this reaction. Finally, we investigated the effect of including in the balance the excitations of neutral atoms. It was found that this also has significant

repercussions on the behavior of the system: it activates an exchange of energy between the plasma populations. This reaction must be declared appropriately depending on whether you are using ADAS or AMJUEL, but consistent results regardless of the database you choose are found. To conclude, we list the reactions that, in order to correctly simulate GyM plasma, must be included in the balance. We will refer to this setup with *run 8.S*:

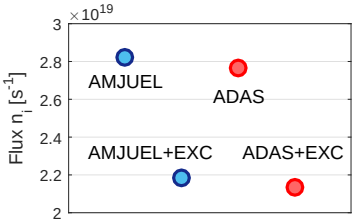

Figure 3.25: Ion particle flux at the West target *flux* n_i, effect of neutral excitation.

- Elastic scattering:
  $He + He \longrightarrow He + He$

```
0 AMMONX H.2  R-HE-HE  EL
```

- Electron ionization:
  $He + e^- \longrightarrow He^+ + e^- + e^-$

```
0 ADAS   H.4  scd96    EI
1 ADAS   H.10 plt96    EI     (DP = -24eV)
```

- Charge exchange:
  $He^+ + He \longrightarrow He + He^+$
  $He^{2+} + He \longrightarrow He + He^{2+}$

```
0 HYDHEL H.1  5.3.1    CX
1 HYDHEL H.3  5.3.1    CX
2 HYDHEL H.1  6.3.1    CX
3 HYDHEL H.3  6.3.1    CX
```

- Radiative recombination:
  $He^+ + e^- \longrightarrow He$

```
0 ADAS   H.4  acd96    RC
1 ADAS   H.10 prb96    RC
```

This list of reactions is what was then used to simulate GyM plasma in the remainder of this thesis work. Results will be seen in Chapter 5. The results found in this work were used to build the current setup for the SOLPS-ITER code in the case of a linear machine with helium plasmas.

The coupling: set up of the ERO2.0 simulation with SOLPS-ITER background plasma

4

4.1 Converting SOLPS-ITER outputs into ERO2.0 inputs 62
4.2 Set up of the global simulation of GyM with ERO2.0 66
4.3 Summary 72

In this chapter we want to show how it was possible to couple the SOLPS-ITER and ERO2.0 codes in the context of linear machine. This coupling work can be divided into two steps. The first, illustrated in Section 4.1, focuses on converting the SOLPS-ITER outputs into a readable format for ERO2.0. It aims both to clarify the conversion procedure and to briefly describe the contents of the generated files. In Section 4.2, on the other hand, the preliminary analysis made for global simulations of ERO2.0 in a linear machine have been reported. This part of the work was made necessary by the fact that it was not yet well known how to optimize the ERO2.0 configuration for this type of application.

4.1 Converting SOLPS-ITER outputs into ERO2.0 inputs

In this section we are going to perform a coupling between the plasma data obtained with SOLPS-ITER and the ERO2.0 code. As represented in the Figure 2.6, ERO2.0 requires the plasma condition at the edge among the input data. The output files of the SOLPS-ITER code are not suitable, at the time of their compilation, to be read by the second code. Consequently, it is necessary to extract the necessary information, to process and to convert it and finally to pass it as an input to the run of the second code. Data conversion is a job that depends on how the files were generated from the plasma edge code, so the job is specific to the pair of codes you want to put in series. So let's see how to couple the outputs of SOLPS-ITER to ERO2.0 in the case of a linear machine, starting from the workflow of the procedure.

4.1.1 Workflow of the procedure

The conceptual workflow of the entire procedure is shown in Figure 4.1. The main program that deals with the generation of input files for ERO2.0 is `heroin`. This program is written in C^{++} and takes in input the 2D data from SOLPS-ITER appropriately processed and compacts them in a single database file referred to a 3D situation: the file that here we call generically `plasma.h5` (the format is *Hierarchical Data Format 5 File*). The files that the `heroin` program needs, indicated in the light blue box in the middle, are generated by two MATLAB [77] routines: the script `heroin_config_linear.m` and the function `original2heroin_solps_iter_linear_half.m`. They have been generated by Romazanov J. in the tokamak framework [75] and re-adapted by Tonello E. for linear machines. The files that `heroin_config_linear.m` needs are taken both from the data produced with SOLPS-ITER and in part they are the tools required to process them, contained in the `tools` and `magnetic`. They allow the reading of the files produced by SOLPS-ITER and the calculation of the

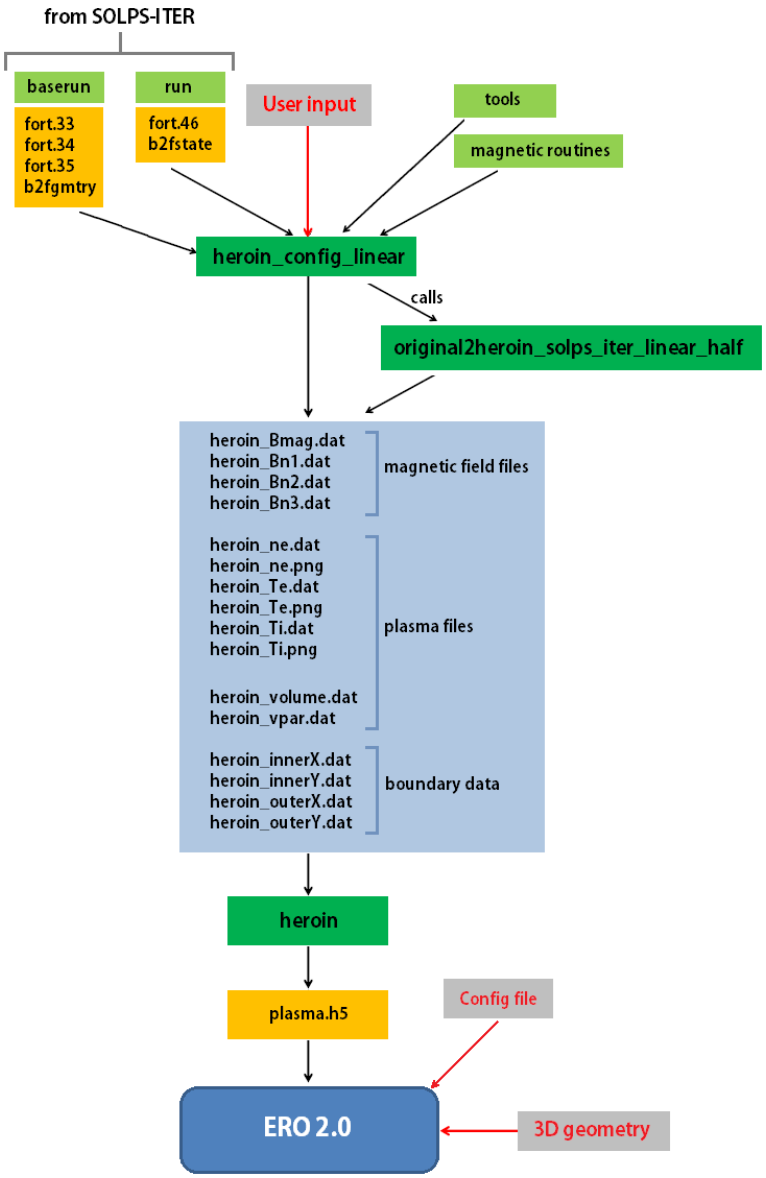

Figure 4.1: Workflow of the converting procedure.

magnetic field of GyM respectively. These second files are the same that were used to solve Grad Shafranov's equation (1.15) in Section 3.1. We can divide the data conversion procedure into three steps, each of them is analyzed in a dedicated paragraph: data reception from SOLPS-ITER, data processing with MATLAB [77] routines and description of ERO2.0 inputs.

4.1.2 Required SOLPS-ITER outputs

We describe the necessary outputs from the SOLPS-ITER side. These files are taken from the *baserun* and *run* folders respectively. The reader was never made a distinction between these two folders, because we never specified the internal structure of the SOLPS-ITER folders. Even here the purpose is not to give a full explanation of this, they have been reported only in the event that the reader is familiar with the SOLPS-ITER code.

What we need to know is only that the SOLPS-ITER baserun contains a series of files that are never changed during the simulation, for example the geometry data of the problem, and they can be in common with other simulation that have a similar setup. In the run, on the other hand, there are files that are updated at each iteration of the code and that contain information on quantities such as plasma density, temperature, etc. recalculated at each step. The contents of these files are shown below.

- **fort.33**, **fort.34** and **fort.35**: EIRENE geometry files, those file contain the coordinates of the nodes, the vertices and the neighbours of the EIRENE triangular mesh.
- **b2fgmtry**: contains the information about the B2.5 geometry.
- **b2fstate**: database file in which the data about the plasma state is stored, such as densities of ions and electrons, temperatures, heat fluxes, velocities etc.
- **fort.46**: contains data about the species treated by EIRENE so: atoms, molecules and test ions. Data are defined on the EIRENE triangle grid, and are: particle and energy densities, components of the momentum density carried in 3D and other information about the finite volume triangle mesh.

(fort.33, fort.34, fort.35): those files contain the cooridfnate of the vertices, nodes AND NEIGHBOURS

4.1.3 Interpolating and extrapolating the data with MATLAB routines

From the files just indicated, the quantities listed in the central blue square are extracted from the MATLAB [77] routines. In particular, the routines allow to obtain from the `b2fstate` file the electronic and ionic temperature values, the electronic density and to view the data (in the `.png` files) for a check before they are compressed by the `heroin` program.

Here we need to make a clarification on how the data of the central block *plasma files* are constructed. The ERO2.0 mesh, specified by the user in the `heroin_config_linear.m` file, extends beyond the wall of the machine to be simulated, unlike the SOLPS-ITER mesh which stops before reach it. The routine performs two things, one is for the computational volume that is in common between the two codes: it interpolates the SOLPS-ITER data on the ERO2.0 mesh. For the rest of the computational volume it extrapolates the SOLPS-ITER data to the ERO2.0 mesh.

The extrapolation of the data from one mesh to another is a decidedly critical step which has a particular weight in determining the results of the simulations made with ERO2.0. The type of extrapolation can be specified within the MATLAB routines and several extrapolations can be chosen, an example of some of these is the following:

- **nearest projection method**: take the unknown data equal to that of the nearest cell with known data. The distance is measured between the sides of the cells, moving perpendicularly from the side of the SOLPS-ITER inner cell to the ERO2.0 outer one.

- **nearest node method**: equal to the previous one but with distance measured between vertices and not between sides.
- **nearest penetration method**: the extrapolated data is given by a linear combination between data of the outermost known cells.
- **exponential method**: the data is extrapolated on the basis of an exponential function with user-defined exponent.

In this work, two methods of extrapolation of the data were considered: the nearest projection method has always been used, except in the last part of the work described in Section 5.4 where the exponential method has been used. The method with which the extrapolation is chosen can greatly affect the results of the simulation, see for example the sensitivity analysis of the results obtained on ITER [75].

Analyzing the remaining data required by `heroin` and created with the MATLAB routines we see that there are *magnetic field files* which respectively contain the module of the magnetic field and the three components of the vector units that identify the direction in 3D. They are calculated with the magnetic field routines mentioned above. Finally, the files in the *boundary data* block contain the coordinates of the points that build the boundary of the SOLPS-ITER mesh.

4.1.4 Running heroin and ERO2.0 inputs

Once all the files in the blue list have been generated, it is possible to launch the `heroin` program which creates the plasma database file in the `.h5` format. At the end of this process we will have obtained an ERO2.0 readable file that contains all the necessary specifications for the code to simulate the background plasma.

In addition to the `plasma.h5` file generated with `heroin`, ERO2.0 needs a dedicated configuration file and the three-dimensional geometry of the internal surfaces of the machine, in our case the GyM linear device. Also the sputtering yield databases must be provided to the code. To handle the ERO2.0 code it is essential to know how to set the configuration file. In this file, all the information needed to manage the functioning of the code is specified by the user. Let's see some examples of parameters that can be specified in this file, with the aim of dwelling only on those that have been important in the work done here:

- **Specification of the 3D mesh representing the external structure**: in the `config` file it is possible to specify the path to the three-dimensional mesh file, user provided. It represents the machines' structure to be simulated. The meshes were built during this work, both less dense for preliminary studies and then more detailed ones in the points where it was necessary.
- **Setting the wall material**: the material of the machine chamber to be simulated can be set and the choice must be compatible with the databases available to the code.
- **Setting the impurity species to compute**: we can specify which charge states of the eroded material to include in the simulation.
- **Setting the number of test particles**: the number of test particles that ERO2.0 uses in the Monte Carlo simulation can be varied. The higher the number, the better the statistical representation of the

simulated particles will be. However, this has a direct impact on the computational cost of the simulation.

- **Particle creation method**: the logic with which the code creates the test particles can be specified by the user as needed. Depending on the choice, a better statistical representation of the simulated physical particles can be obtained.
- **Setting the number of time steps**: at each step the code calculates the erosion of the plasma and the self-sputtering erosion of the particles eroded by the plasma at the beginning of the step. From the second step onwards ERO2.0, in the first calculation also includes the impurities erosion contribution coming from the previous step.

4.2 Set up of the global simulation of GyM with ERO2.0

As already introduced in Section 2.5, with global simulation we mean the use of the ERO2.0 code for the study of the erosion and transport of impurities on macroscopic spatial scale. In this section we are going to present the results of the preliminary investigations made with ERO2.0, where it was possible to understand which parameters were important for the use we made of the code. In this sense, the goal was to gradually refine the results produced by the code, looking for a satisfactory degree of detail with acceptable computational cost. The analysis in the next Chapter 5 have been done thanks to the results obtained here.

4.2.1 The choice of copper as the wall material

The GyM chamber is made of steel, which as we know is an alloy of iron and carbon. Precisely for this reason, simulating a material such as steel is not easy. This is because the data available to simulate the interaction between plasma and material are collected in databases that refer to specific pairs of plasma and material. From the knowledge of the sputtering yields of two distinct materials with the same plasma it is not immediate to deduce the sputtering yields of a solid formed by a combination of the two materials. If we wanted to model a steel GyM chamber, it would therefore be necessary to carry out specific work to obtain databases of a helium plasma on steel. At this point, the choice could shift to iron, since carbon is present in steel only in a very limited percentage ($< 2\%$). Also in this case, however, helium-on-iron plasma databases were not available to the code at time. Consequently the choice made is *copper*. Copper is the element with the closest atomic weight (63.546 u) to that of iron (55.845 u) of which the interaction databases with helium plasmas are available. For the sake of completeness we show in the Figure 4.2 the sputtering yield of helium on copper taken from [42].

4.2.2 Building 3D geometry and mesh refining

The first investigation made concerns the construction of the three-dimensional geometry. As previously said, GyM is a linear machine and

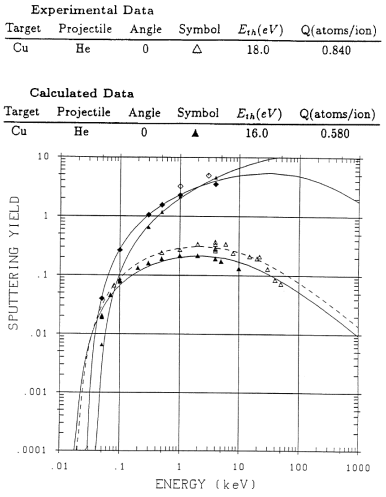

Figure 4.2: Energy dependence of the sputtering yield of Cu with ^{4}He ions.

as we have seen also in Section 3.1 the inner chamber is cylindrical. Inside there are also cylindrical elements with a diameter and height of 20mm, the *bushings*. These elements allow to insert inside the chamber some tungsten *liners* to restrict the plasma volume, a useful configuration for some experimental GyM activities.

The three-dimensional mesh has been built in order to reproduce the internal chamber of the GyM machine in the simplest possible way and the geometries are mostly made up of simple shapes. It is a set of four different meshes that represent each one: the two bases Figure 4.4, the bushings Figure 4.7 and the side walls of the machine Figure 4.5 and Figure 4.6 divided into two half cylinders. All the components have been constructed starting from the technical drawings of GyM, from ISTP intranet (REFERENCE). We see below a section of the simulated geometry and we see on the side the 4 meshes that have been built and that together constitute the internal chamber of GyM.

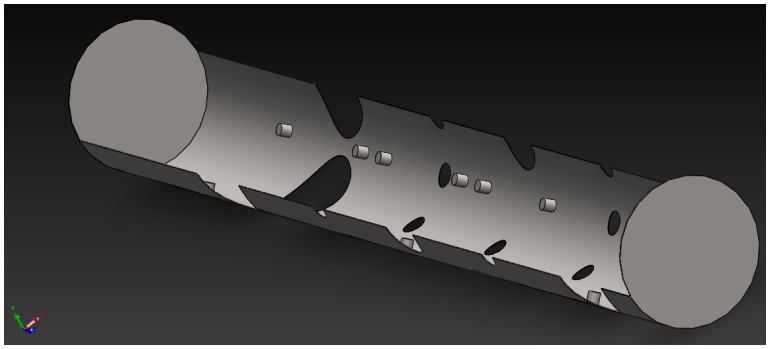

Figure 4.3: Section of the GyM's internal surfaces, simplified for modelling.

The triangular meshes were constructed so that each surface (or PFCs, from plasma facing component) was divided into elements each with approximately the same area, since ERO2.0 could work in a more optimized way. This is because the code works by throwing test particles from each cell into which the geometry is divided (as long as the number of these is large enough) and imbalances in the erosion calculation can arise due to the existence of cells that are too large or too small. This principle is valid only if we consider cells of the same component (for example the

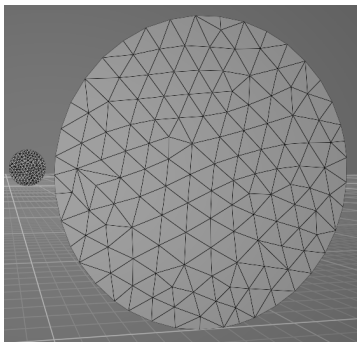

Figure 4.4: Representation of the mesh constructed for GyM bases.

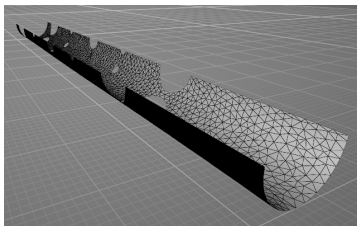

Figure 4.5: Representation of the mesh constructed for GyM lateral wall, part I.

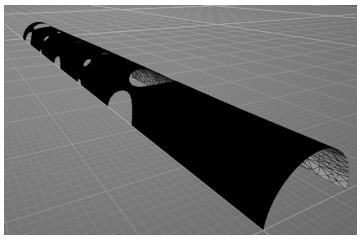

Figure 4.6: Representation of the mesh constructed for GyM lateral wall, part II.

RUN	PFC	# ELEMENTS	# STEPS	COMP TIME
1.E	1	512	2	$2.25 \cdot 10^3 s$
2.E	1, 2	2112	2	$2.21 \cdot 10^3 s$
3.E	1, 2, 3	10427	2	$2.38 \cdot 10^3 s$

Table 4.1: Summary of the computational cost of the simulations, adding elements to the 3D mesh

bases), it can be relaxed if we take cells from different components (for example bases and side walls).

Once the 3D contours of the internal surface of GyM were defined, three preliminary simulations were made in which the different elements that make up the three-dimensional geometry were inserted one at a time: the first with only the bases, the second with bases and bushings, the third with bases, bushings and side walls. Thanks to this, it was possible to evaluate the computational cost, to be subsequently related to the quality and precision of the results. In these three simulations for each simulation two time steps were computed and the traced impurities included were only Cu and Cu^+. Let's summarize everything in this Table 4.1, where with *PFC = 1* we indicate the bases mesh, with *PFC = 2* the bushings and with *PFC = 3* the side walls.

From the results obtained we can say that even inserting large surfaces with very large meshes such as side walls, it does not affect too much the computational cost of the simulation. In fact, this cost seems to depend much more on the number of test particles that the Monte Carlo code has to deal with. In this case the number of test particles is fixed at 10^4. Choosing a low number of test particles does mean lowering the computational cost of the simulation but it is not advisable for very large meshes. In fact the code tends to try to launch at least one test particle for each cell that undergoes some PWI interaction. In the last case we would have an insufficient number of particles for this purpose if all the cells were affected by at least one interaction. Therefore it is advisable, in the latter case, to increase it, to ensure that the eroded particles are correctly tracked. This aspect will then be dealt with later in the chapter, first it is necessary to make a further consideration linked to the low quality of the results obtained with these meshes on the bases and bushings of the simulated machine.

In the Figure 4.8 Figure 4.9 and Figure 4.10 the two bases and one of the bushings are represented respectively, on which are represented total erosion (contribution of plasma and self-sputtering of the impurities) and the plasma particle flux. As can be seen from the figures, the meshes used for the bases and bushings are not suitable for correctly describing the nature of the process. One of the most important consequences of having an insufficiently refined mesh is that the specificities of processes such as erosion (that we remember being an energy threshold process) are not well captured. This can lead to poor accuracy in the results. Even on the bushings, where the plasma impacts at different angles, we can see that there is a poor quality in capturing the angular pattern of the erosion, visible only by increasing the richness of the various angles of incidence of the surfaces. On the walls of the machine the quality of the result turned out to be satisfactory, results are not reported here because it will be analyzed in detail in the dedicated Chapter 5.

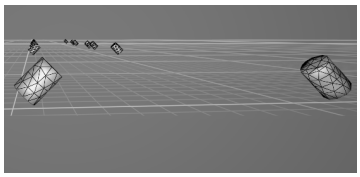

Figure 4.7: Representation of the mesh constructed for GyM internal bushings.

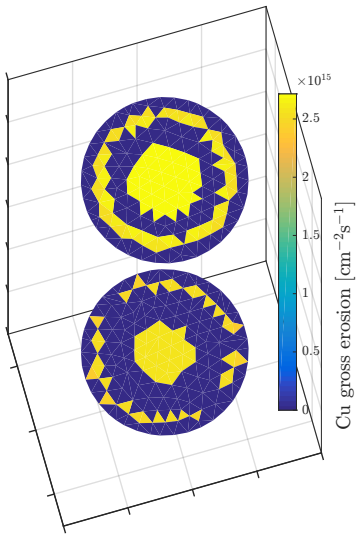

Figure 4.8: Total erosion rate of the bases $s^{-1}m^{-2}$, contribution from plasma ion erosion rate and impurity erosion rate.

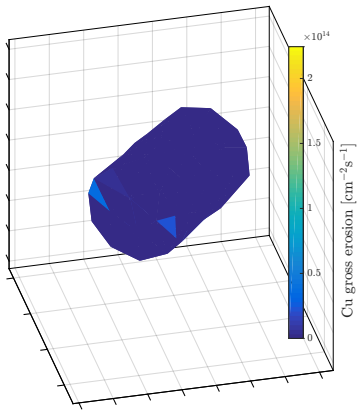

Figure 4.9: Total erosion rate of the bushings $s^{-1}m^{-2}$, contribution from plasma ion erosion rate and impurity erosion rate.

RUN	PFC	# ELEMENTS	# STEPS	COMP TIME
4.E	1,2,3	40.717	1	$5.37 \cdot 10^3 s$

Table 4.2: Summary of the setup using the refined mesh.

What was done was to increase the mesh accuracy on the components that required it. We passed from 512 to 12.174 on the bases while from 1.600 to 20.228 on the bushings, for a total of 40.717 cells. The number of test particles was increased from 10^4 to $4 \cdot 10^4$ and the time steps decreased from 2 to 1. The computational cost required was not unreasonable, in fact the simulation time has little more than doubled, passing from $2.30 \cdot 10^3 s$ to $5.37 \cdot 10^3 s$. The information on the simulation performed is summarized in the Table 4.2.

In this way, a degree of detail of the results has been obtained (shown in Chapter 5). In the Figure 4.11 and Figure 4.12 we can see the refined meshes.

We can conclude by saying that the greatest contribution in the computational cost is given by the number of time steps that you decide to perform, because as the test particles grow, the computational cost of each step increases. The choice made by us in order not to have too high computational times must, however, be adequately motivated. We must ask ourselves whether or not a situation of equilibrium is reached between the self-sputtering phenomena in a single time step, otherwise this is underestimated. It is very important to refine the mesh in the points where the erosion has thresholds in order to be able to capture its nature. At the end of this section we recall also that we have not yet faced the problem of the statistics of test particles, an issue that we deal with in the dedicated paragraph.

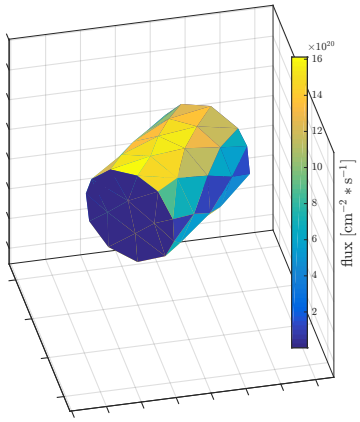

Figure 4.10: Plasma ion particle flux impinging on the bushings $atm/s\ m^2$.

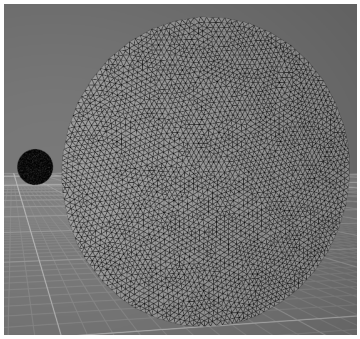

Figure 4.11: Representation of the refined mesh for GyM bases.

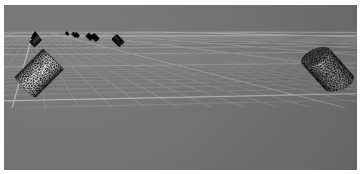

Figure 4.12: Representation of the refined mesh for GyM internal bushings.

4.2.3 Presence of other impurities: including the Cu^{2+}

Before proceeding with the actual refinement of the mesh, we moved with the aim of understanding whether the choice of including only Cu and Cu^+ was a reasonable choice. On the one hand, the presence of Cu^{2+} is certainly lower than Cu^+, but this ion is much more effective if we talk about sputtering: it sees a sheath potential that is the double of that of Cu^+ ion. Furthermore, given the atomic number of copper ($Z = 29$), and given that the second ionization energy is $\approx 20.29eV$, it does not seem unreasonable to try to include this second charged species in the calculation of impurities as well. An analysis was made of the impact it had on the results from the point of view of computational time. We tried to include also the Cu^{2+} in the *run 3.E* and we observed only a $50s$ increase in the computational time. However, the increase in the erosion rate was not so considerable, in fact we passed from $3.31 \cdot 10^{11} atm/s\ cm^2$ to $3.32 \cdot 10^{11} atm/s\ cm^2$. However, since the computational cost did not increase too much, the choice was made to include this charged species anyway. One more reason to make this choice is that by comparing the erosion rates between two successive time steps: it can be seen that the erosion rate varies less between the first and the second time step if the Cu^{2+} is included.

4.2.4 Time evolution: reaching the equilibrium

After choosing to reduce the number of simulation time steps from 2 to 1, we have to ask ourselves if this choice is reasonable or not. Remember that at each time step the code includes the erosion contributions of the particles eroded at the previous time step, so the number of time steps is very important if for increasing time the erosion due to the eroded particles tends to change. If, on the other hand, this contribution is constant, then we can say that we are in an equilibrium situation and therefore the time evolution will have no effect on the results. Consequently it will not be important to consider more time steps but it will be sufficient to take for example only the first step. To study the situation, we launched a simulation with 20 time steps and went to analyze the erosion data of the eroded particles. Moreover, in this simulation we have applied a bias potential of $100V$ to the most eroded surfaces: the basics (for a complete discussion of the effects of the bias on the results, see the dedicated section Section 5.2). For what concerns this part, has been observed that between successive time steps this value did not change but remained constant over time. This results is very important because confirms that also in an enhanced erosion situation (due to the application of the bias we reach a stationary result). We therefore concluded by saying that a single time step was sufficient to calculate the erosion, because in this time interval a stationary condition is reached for the process.

4.2.5 Statistics optimization strategies with refined mesh

Let us now turn to the question of test particle statistics. At the beginning of the discussion made in this Section 4.2, it was said that it is important to verify that the number of test particles used is sufficiently large to well represent the behavior of the population of impurities they represent. In this brief analysis we tried first of all to understand if, in the preliminary simulations made, the number of particles used was sufficient. After this we moved to understand the functioning of the code when applying different logics in test particles creation, to go in the direction of improve statistical parameters when you want to avoid increasing the computational cost too much.

Taking into account the considerations made in the first part of this analysis, we reported the results regarding the simulation statistic indicated with the code *run 4.E*:

RUN	**#TEST**	R_0**[#/s]**	R**[#/s]**	R/R_0	**LOST FR.**
4.E	40.000	$8.98 \cdot 10^{13}$	$8.98 \cdot 10^{13}$	100%	0.0329%

Table 4.3: Summary of the statistics with refined mesh, **LOST FR.** = lost fraction.

Where R_0 indicates the number of real particles that are eroded by the surface, while with R those represented by the test particles. *Lost fraction* represents the unit complement of the R/R_0 ratio and therefore the fraction of untracked eroded particles. The logic with which ERO2.0 assigns the test particles to the cells of each PFCs is in this case: constant number of particles launched from all PFCs, with the number of particles per PFC scaled with the gross erosion of the whole PFC. This method is named by the code as *Creation Method (C.M.) = 4*.

Analyzing the table, we see that although the number of test particles is less than the number of cells from which the erosion should be calculated, with this logic we have an excellent representation of the real particles by the test particles. This is certainly due to the fact that, as will also be seen in the analysis made in Chapter 5 and as already seen from the results with the raw mesh, many cells do not undergo erosion. So the number of cells actually affected by erosion is less than the test particles available to the code. If, on the other hand, the background plasma were different and we were in the condition of greater surface erosion, surely for the same test particles the statistics would worsen. As an example and without going into too much detail, we use once again the plasma from *run 7.S* to see the effect it has on the statistics the increased wall erosion.

Three different simulations have been made, the specifications of which are listed below in Table 4.4. The three simulations were generated starting from the considerations just made on erosion: the setup of the *run 4.E* simulation was taken, the background plasma was changed, excluding the charge exchange reactions, and the refined mesh was used. Always taking $40,000$ particles, three different logics scheme for creating test particles were adopted to evaluate their functioning.

RUN	**C.M.**	R_0**[#/s]**	R**[#/s]**	R/R_0	**LOST FR.**	**R. F.**
5.E	4	$6.34 \cdot 10^{15}$	$5.83 \cdot 10^{15}$	92.1%	7.93%	×
6.E	4	$6.34 \cdot 10^{15}$	$5.99 \cdot 10^{15}$	94.6%	5.43%	×
7.E	2	$6.34 \cdot 10^{15}$	$5.83 \cdot 10^{15}$	92.1%	×	1.09

Table 4.4: Summary of the statistic optimization results. **C.M.** = creation method, **LOST FR.** = lost fraction, **R.F.** = rescale factor.

The first logic scheme is the same as the *run 4.E* but as we can see, increasing the erosion decreases the precision with which the eroded particles are represented, because fewer and fewer cells are not affected by the erosion. The other two simulations were launched respectively by activating a different logic scheme. *Run 6.E* uses a different *creation method* with respect to *run 5.E* while *run 7.E* uses the same creation method of *run 5.E* but explores the introduction of a *rescale factor*. The creation method *C. M. = 2* differs from *C. M. = 4* presented above, to the extent that the code may choose to increase the test particles to try to fill the lack of test particles. In this way we see that the representation statistics improve, but the disadvantage is that at each time step there is no constant number of test particles. The second method that can be followed (*run 7.E*) to improve the statistic is to scale the weight of all test particles by a *rescaling factor* (RF) so that untracked particles could also be included. The rescaling factor is given by the ratio R_0/R and ensures that particles that would not be tracked are redistributed into the generated test particles.

If we chose to combine the logics of *run 6.E* and *run 7.E*, we would certainly go in the direction of improving the representation statistics and the total number of physical particles represented would be preserved. However, the risk in this case is that if there are many areas where erosion is low, the contributions from this type of surface would be overestimated. It is therefore necessary to evaluate case by case which is the best solution to optimize this parameter. The best choice in our case seemed simply to increase the number of test particles to 50.000 from now on: it does

not seem to be too prohibitive from a computational cost point of view. This is because in Chapter 5 we are going to work in the direction of increasing the erosion in some cases and we need this margin to remain calm from the point of view of the issues just presented.

4.2.6 Wall reflections and analytical sheath tracing models

Here we want to briefly present two other parameters we investigated and that concern the collision and emission of particles by the surfaces with which they interact.

To calculate the angle of reflection, the standard choice of the code is to use a cosine distribution for emission angle: the angle formed between the trajectory and the normal to the surface that emits the particle. The code, among the various possibilities, provides that of using the `SDTrimSP` code for reflected energy and polar / azimuthal angle distribution. The effect of the variation of this parameter, however, was not appreciable because in our case we do not have wall reflection.

A second interesting parameter to vary in the calculation of the trajectories seemed to be that of the model with which the tracing of the trajectories in the sheath is made. By default ERO2.0 traces particles with the default Monte Carlo method. On the other hand, it is however possible to activate an analytical tracking according to the Borodkina [78] approximation model. In this case, unfortunately, it was not possible to appreciate the results of this analysis because the computational cost was too high, even limiting the number of test particles to 10.000.

4.3 Summary

In this chapter we have dedicated ourselves to conceptually describe the procedure with which it is possible to convert the data produced by SOLPS-ITER into a format that could be read by the ERO2.0 code. The passage from one code to another is achieved through the use of *ad-hoc* written routines because the data conversion depends on the specific pair of codes we want to put in series. After doing this we focused on some important aspects that we had to face in setting up the global simulation with ERO2.0 in the context of GyM. These include the choice of material, the creation of the three-dimensional precise meshes and the way in which the test particles are treated by the code. It is also important to have a sufficiently refined mesh in the transition areas between below and above the sputtering threshold. Finally we tried to understand which strategies can be adopted when we want to improve the representation statistics of real particles by the test ones.

Coupled Simulations Analysis 5

In this chapter we focus on the presentation of the results obtained with the coupled simulations of SOLPS-ITER and ERO2.0. In Section 5.1 we focus on plasma analysis, in the light of all the considerations made on the reaction setup to be included in simulating a helium plasma in a linear machine. We then move to the analysis of the surfaces facing the plasma, focusing on the erosion patterns both from plasma physical sputtering and self-sputtering contributions. The transport of the eroded particles in the machine is then analyzed in its relevant features. These include the impact energy and impact incidence angle distributions of the impurities and the re-deposition fractions on the inner structure components of the machine. Finally, a sensitivity analysis of the results is made, using a background plasma in which charge exchange reactions are neglected. In Section 5.2 the application of a bias potential to the bases and bushings surfaces, was simulated. The effect it has on the erosion data of the surfaces and on the behavior of the eroded species was observed, including both the analysis of energy and incidence angle distributions at the impacts. In Section 5.3 it has been explored the possibility of varying the chamber's material, choosing two other materials that might have some interests related to the thermonuclear fusion. Also in this case, the sputtering patterns and the behavior of the eroded species were analyzed even when varying the applied bias to bases and bushings. Finally, in Section 5.4 another plasma configuration was simulated with SOLPS-ITER and a sensitivity analysis was made on the data extrapolation method between the innermost mesh of SOLPS-ITER and the more extended one of ERO2.0.

5.1 Helium plasma on a GyM made of copper 73
5.2 Enhancing the erosion: applying the bias to the surfaces 81
5.3 Changing the material of the chamber: tungsten and carbon 85
5.4 Restricting the plasma: varying the extrapolation 90
5.5 Limits of this modelling . . 93
5.6 Summary 94

5.1 Helium plasma on a GyM made of copper

As anticipated in the introduction of the chapter, in this section we are going to analyze the results of the coupled simulation performed with SOLPS-ITER and ERO2.0 of GyM. Let us start by analyzing the background plasma data.

5.1.1 Data on the helium plasma in working conditions

Before proceeding, we recall that the overall setup of the helium reactions (*run 8.S*) is described in detail in Section 3.4 and that the summary of the setup for GyM main parameters is the one in Table 3.1. For ERO2.0 setup we used the results of Chapter 4 concerning the choice of the refined mesh, with 50.000 test particles and considering only one time step. Let's start by analyzing the helium plasma with the help of the following graphs in Figure 5.1, Figure 5.2, Figure 5.3 and Figure 5.4.

In the Figure 5.2 we can see the trend of the ionic and electronic temperatures, of the electron density and of the neutral atoms density with respect

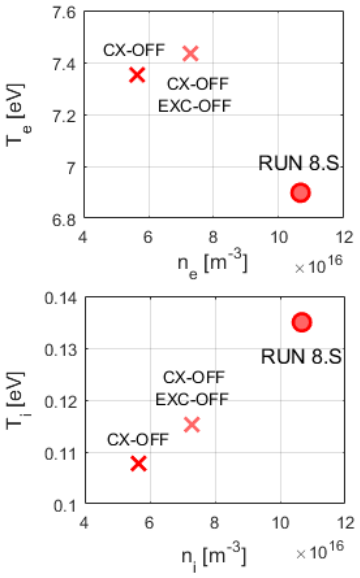

Figure 5.1: Mean volume temperature and density plots, for electron population (first figure T_e, n_e) and ion (second figure T_i, n_i).

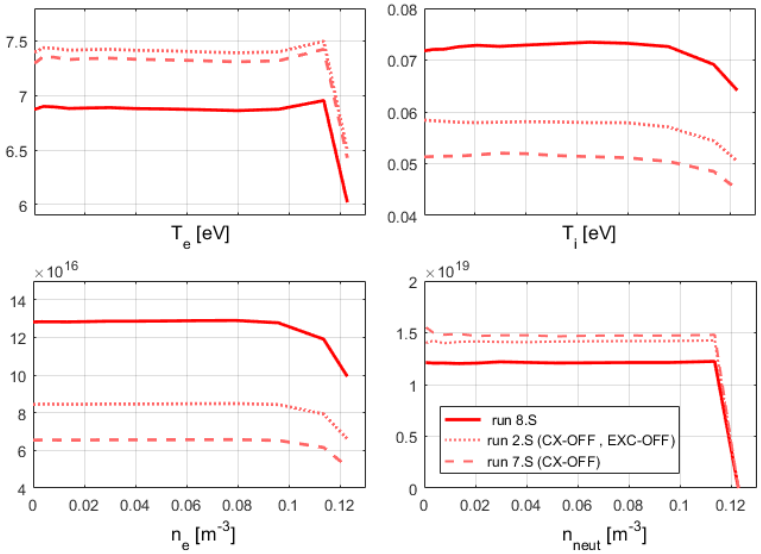

Figure 5.2: Radial profiles of the electron and ion temperatures T_e, T_i $[eV]$, electron and neutral densities n_e, n_{neut} $[m^{-3}]$.

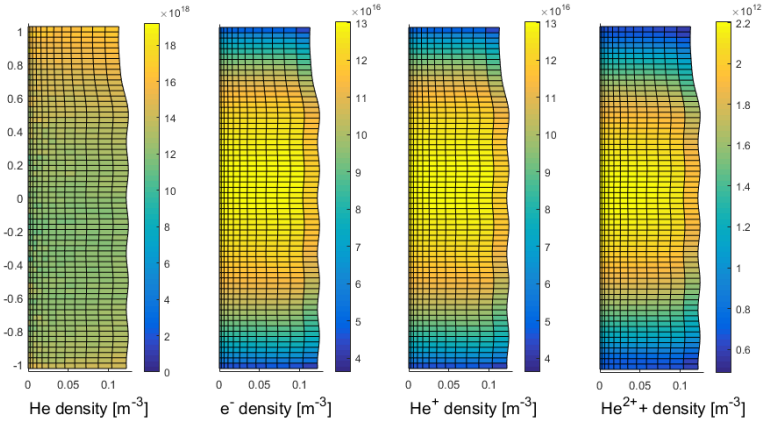

Figure 5.3: Neutral He, electron e^-, He^+ and He^{2+} density 2D contour plots, $[m^{-3}]$.

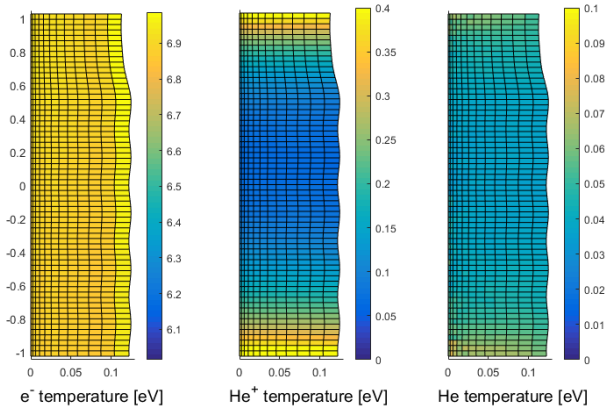

Figure 5.4: Electron e^-, He^+ and He^{2+} temperature 2D contour plots, $[eV]$.

to the radial coordinate, all calculated at the axial height of the *Langmuir probes*. Langmuir probes are experimental instruments that permit to determine typical quantities for the characterization of plasmas such as temperatures and species density. In these graphs ion density profile has not been reported because it has the same trend as the electronic one. Furthermore, the temperature of the neutral species has not been represented here because it is not a particularly relevant data from the point of view of its radial trend. It can also be seen from the Figure 5.4 which presents its trend over the entire section of the machine.

In Figure 5.2 we also reported the profiles obtained if we neglected only the contributions of charge exchange reactions (*run 7.S*) or even the excitations of neutrals in collisions with electrons (*run 2. S*). We see in the results that all the analyzed quantities show a decrease at the edge, while they have an almost constant trend up to a radius of about $0.1m$. The average volume quantities have been calculated in Figure 5.1 and they show us that the electron temperature is approximately $6.9eV$ while the ion one is $\approx 0.135eV$. Electron and ion mean densities are just below $1.1 \cdot 10^{17} m^{-3}$ while the neutral density is around $1.2 \cdot 10^{19} m^{-3}$. We can calculate the ratio between the two populations' densities and find that the degree of ionization of the plasma is less than 1% ($\approx 0.91\%$).

If we now observe the Figure 5.3, we can see at the ends of the chamber, in correspondence with the two bases, the *recycling* of neutrals. The ions and electrons have a decreasing density when approaching the sheath, while the neutral density increases because they are released from the bases after the radiative recombination of the helium ions on them has taken place. The neutral atoms, going towards the center of the machine in the axial direction, are ionized again and what can be seen is a decreasing density of this population and an increase of the ionized one. Unfortunately, the large difference in density values between plasma populations does not allow a comparison using the same color scale, but looking at figure side, one can understand the order of magnitude of the density of the populations. It can also be seen that the ion He^{2+} density has a pattern similar to that of the He^{+} but with a number density of almost five orders of magnitude less.

In the Figure 5.4 we can observe that the electron temperature is almost constant throughout the chamber volume, this happens due to the high mobility of the electron population. What we see instead for the He^{+} ion is an increase in temperature due to the presence of the plasma sheath which accelerates the ions towards the wall. Also the neutrals He show an increase in temperature at the extremes.

5.1.2 Plasma fluxes and temperatures on the surfaces

Let us now analyze the behavior of the plasma particles in the chamber of the linear machine. We spoke about particles' motion in external magnetic fields, mentioning the gyration motion around the guide center. Following magnetic field lines, particles will collide on the surfaces they intersect. In the Figure 5.5 we have represented the particle flux density ($\#atmm^2s^{-1}$) on the reference mesh. Since the cells are closer together as you move towards the axis of the machine, it is important to clarify that the graph does not represent greater flux with denser lines, but only

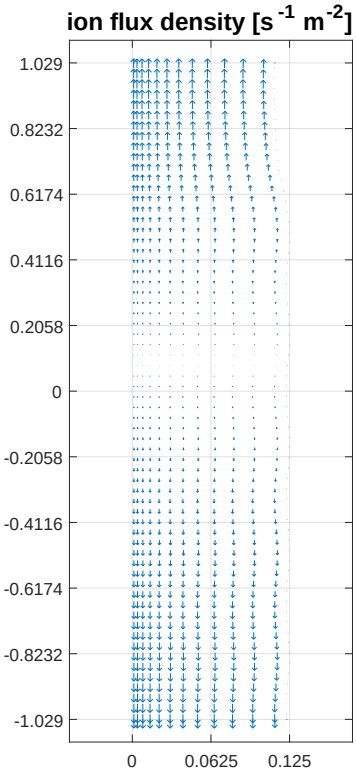

Figure 5.5: Ion particle flux density ($\#atmm^2s^{-1}$) on the reference mesh.

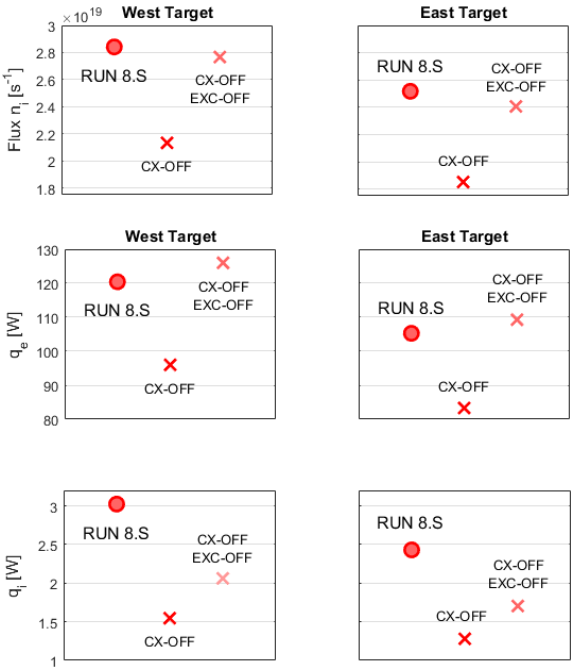

Figure 5.6: Ion particle flux *flux* n_i at the West target (left) and at the East target (right), $[s^{-1}]$.

Figure 5.7: Thermal energy fluxes at the West (left) and East (right) targets, for electron population (upper half q_e) and ion (lower half q_i), $[W]$.

the flux value at the point considered (that is the center of the mesh cell). The amplitude of the arrow is proportional to the value of the flux in that point. Analyzing the figure, we see how the charged particles follow the field lines and collide on the two bases of the machine. From here on we will call the upper base with the name that SOLPS-ITER assigns it, that is with *West Target*, the other will be indicated with *East Target*. We can see that the abscissa where the longitudinal component of the velocity is zero, is slightly shifted towards the West target, where the magnetic field is narrower. The fact that the magnetic field is narrower near the West target also affects particle fluxes and thermal powers at the targets. Let us see them in the Figure 5.6 and Figure 5.7.

As already anticipated, the number of particles per unit of time that reaches the two targets is greater on the base closest to the most intense magnetic field. This also results in a higher thermal load, both ionic and electronic. The difference between the two transmitted powers is just less than $20W$, West Target load is around $120W$, which translates into an average power flux of about $2.5kWm^{-2}$.

Let us see some of these quantities represented directly on the surfaces we are considering. We considered the helium ion flux density and the electronic temperature on the bases and on the bushings, respectively in the Figure 5.9 (to be related to the Figure 5.5) and Figure 5.10. The Figure 5.8 instead represents the electron thermal power per unit surface that reaches the bases, which must be related to the total one represented in the Figure 5.7.

These data have been extrapolated from ERO2.0 starting from the SOLPS-ITER data. On the bases the pattern observed is similar to that of the radial density profiles shown above: it is approximately constant and then falls near the edge. This is true also for both the ion particle flux and the electron temperature. The latter shows a slight rise, before reaching its maximum value, in a precise radial point. If all the maxima are collected

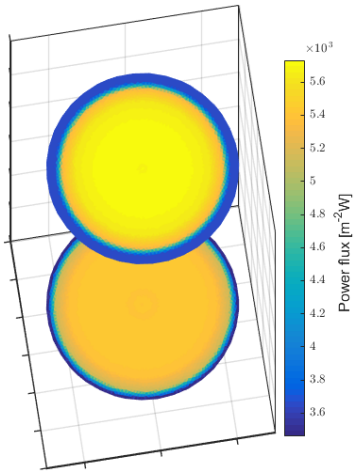

Figure 5.8: Electron thermal energy flux density at the GyM bases, $[Wm^{-2}]$.

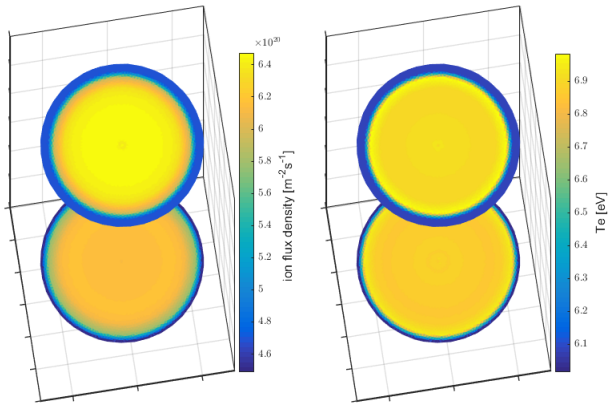

Figure 5.9: Ion particle flux density $[m^{-2}s^{-1}]$ and electron temperature T_e $[eV]$ on the GyM bases.

together on the surface, they form an annulus pattern. This pattern is also observable in Figure 5.2.

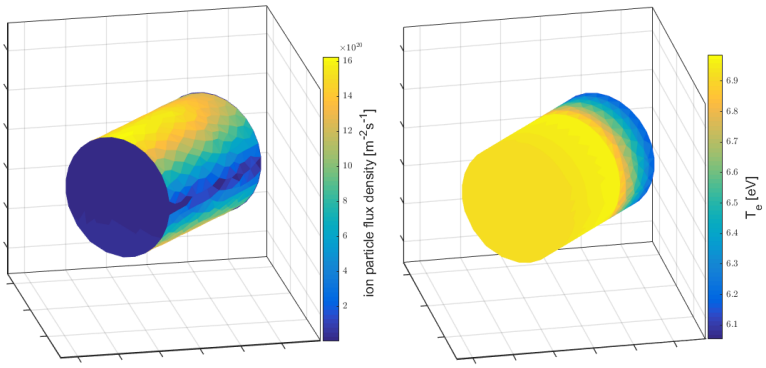

Figure 5.10: Ion particle flux density $[m^{-2}s^{-1}]$ and electron temperature T_e $[eV]$ on the bushings.

Since there are a lot of bushings in the chamber, one of them has been taken as reference. It is placed about halfway the length of the chamber, closest to the area where the plasma shrinks. It is not important to analyze each of the bushings because more or less the considerations that can be made by looking at just one are also valid for all the others. On the surface represented in Figure 5.10 one can easily see how the plasma (which impacts along the bottom-up direction) has different angles of incidence. It will therefore be interesting to study the erosion of plasma on the surface at different angles of incidence. Looking instead at the electron temperature, it can be seen that it does not depend on the angle formed between the plasma flux and the normal to the surface of the bushing. Also in this case it is due to the effect of the mobility of the electron population.

5.1.3 Erosion analysis of helium plasma on copper

We now put the attention on some results that can be obtained with ERO2.0 regarding the linear machine's internal structure erosion. Firstly we make some considerations on general data, then we will pass to a more specific analysis of the different surfaces. As mentioned in Section 2.1, various physical phenomena can contribute to the phenomenon of surface sputtering. We analyzed here the physical sputtering, to which two contributions exist in this case: that coming from plasma ions and the one from self-sputtering of eroded copper impurities. In this operating

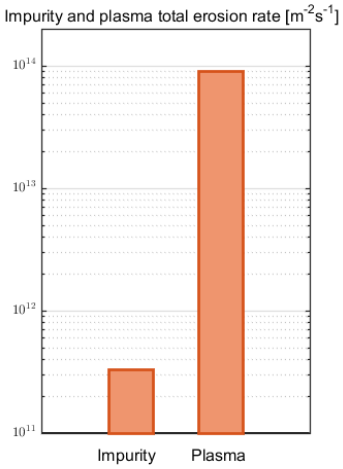

Figure 5.11: Comparison between erosion rate due to plasma and due to self-sputtering $[m^{-2}s^{-1}]$.

condition, we can observe that the greatest contribution to erosion is given by the plasma ions. In fact, as can be seen in the Figure 5.11 the contribution of sputtering by the plasma ions is at least two orders of magnitude more important than that of copper self-sputtering. The overall erosion is equal to

$$8.98 \cdot 10^{13} atm\ s^{-1} + 3.31 \cdot 10^{11} atm\ s^{-1} = 9.01 \cdot 10^{13} atm\ s^{-1}$$

Going into more detail, we can analyze how the erosion contribution is divided between the internal surfaces of the machine. As we have said, almost all of the erosion occurs thanks to the plasma and if we isolated the contribution of plasma erosion only, we would obtain that only the bases of the GyM chamber are involved in this phenomenon. However, the self-sputtering contribution exists and all internal surfaces are affected, albeit to a lesser extent than the bases. We analyze the erosion on each component.

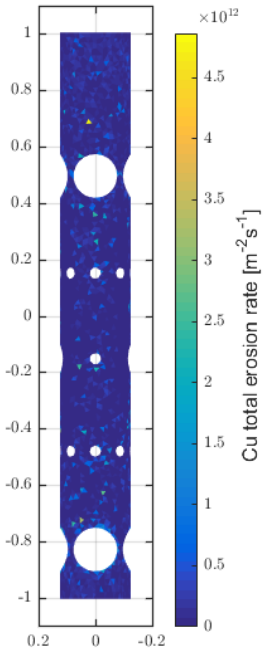

Figure 5.12: Erosion rate on GyM lateral walls $[m^{-2}s^{-1}]$.

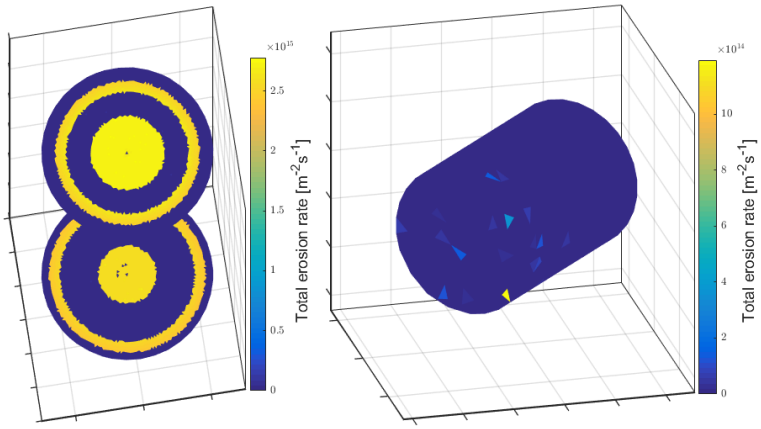

Figure 5.13: Erosion rate on GyM bases and bushings $[m^{-2}s^{-1}]$.

We in Figure 5.13 that the bases are eroded in the center and on an external annulus. This pattern refers to the shape that the electronic temperature has, in fact in the points where the electronic temperature is higher it seems that erosion occurs, because in these points plasma conditions that allow the ions to exceed the sputtering threshold of the material are reached. The clear division between the eroded and the non-eroded areas suggests the need to increase the precision in the calculation of the sputtering yield for the helium-copper pair in the proximity of the threshold. Instead, one would expect that, since the plasma quantities do not vary so abruptly along the surface, the resulting sputtering pattern should also be. Looking at the erosion on the side walls and on the bushings, we can see how the erosion contribution is much less uniform than that on the bases, thus indicating that the erosion of these surfaces is due to the self-sputtering of the eroded copper particles.

5.1.4 Impurity transport: trajectories, densities and redeposition

Let us now analyze some aspects related to the presence of impurities inside the GyM chamber once eroded by the walls. We begin by showing the impurity densities in the Figure 5.14. As we can see, the number

densities of the copper particles Cu and the ionized copper Cu^+ are comparable. In fact, there is an ionization percentage of 45.8%. The neutral copper atom density close to the bases is around $10^{12} \div 10^{13} atm\ m^{-3}$. As can be seen in the Figure 5.14 and as can also be seen in the Figure 5.15, which represents only some of the trajectories of the test particles, the Cu^+ charged particles tend to be distributed more evenly throughout the volume of the chamber. This is because being charged particles, they follow the magnetic field lines. Neutral particles, on the other hand, unless they undergo ionization, have rectilinear trajectories because they do not feel the effect of the electromagnetic field.

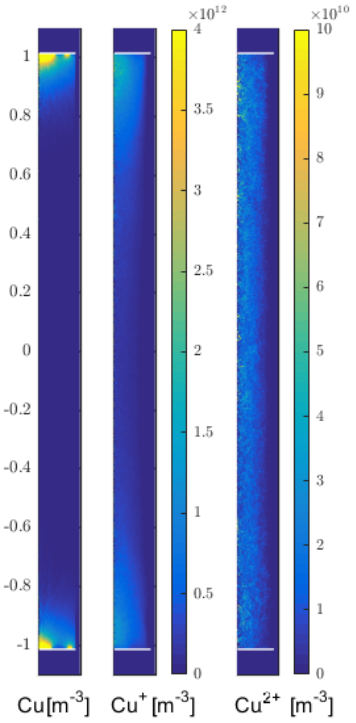

Figure 5.14: Neutral Cu, Cu^+ and Cu^{2+} density 2D contour plots, $[m^{-3}]$.

5.1.5 Impacts of the impurities with the wall: energy and angle distributions

Once the impurities have entered the plasma and transported, they are re-deposited on the internal surfaces of the chamber. To conclude this first section of analysis, we show some features about the re-deposition phenomena. Let us start by calculating the percentage of re-deposition of the impurities on the various components, which results: 28.4% on the bases, 0.9% on the bushings and 70.7% on lateral walls. We observe in the Figure 5.17 and in the Figure 5.16 re-deposition patterns over the surfaces.

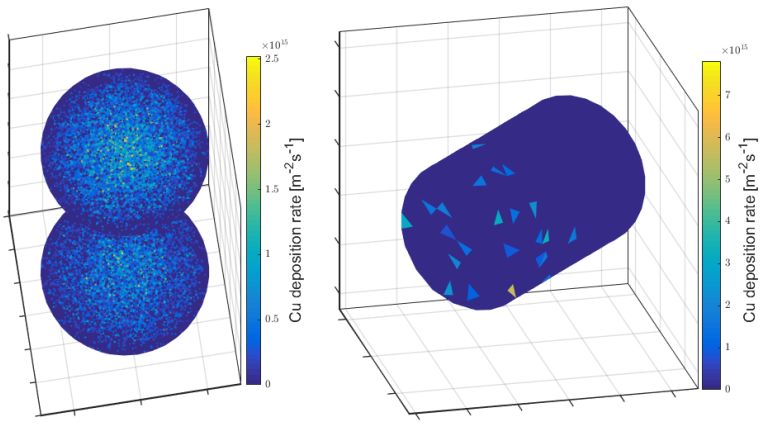

Figure 5.17: Deposition rate of the impurities on GyM bases and bushings $[m^{-2}s^{-1}]$

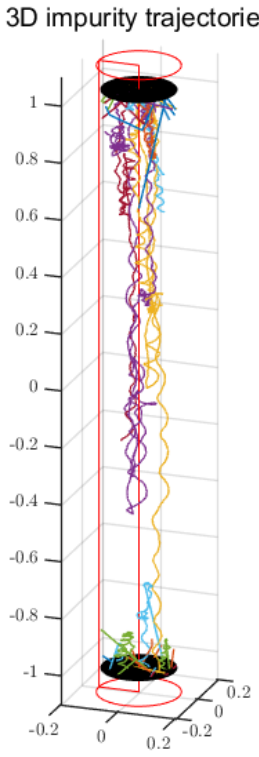

Figure 5.15: 3D trajectories of some of the traced impurities.

As we can see, most of the impurities are distributed in the close-to-the-bases part of the side walls. The particles that arrive here are mostly neutral copper atoms eroded by the bases. Not being affected by the magnetic field and being the geometry of the machine very elongated, it is easy for neutral particles to end up in this area. The re-deposition on the bases is certainly more related to charged particles which, following the magnetic field, have been transported to where them intersect the structure. Let us now analyze Figure 5.18 which represents the energy distributions and the angle of incidence of the impurities upon impact with any internal surface of the machine.

We can see, by looking at the energy distributions, that a large amount of eroded copper atoms collide with GyM structure at very low energy. These particles are certainly neutral particles because they are not affected by the acceleration given by the sheath potential. We then notice four

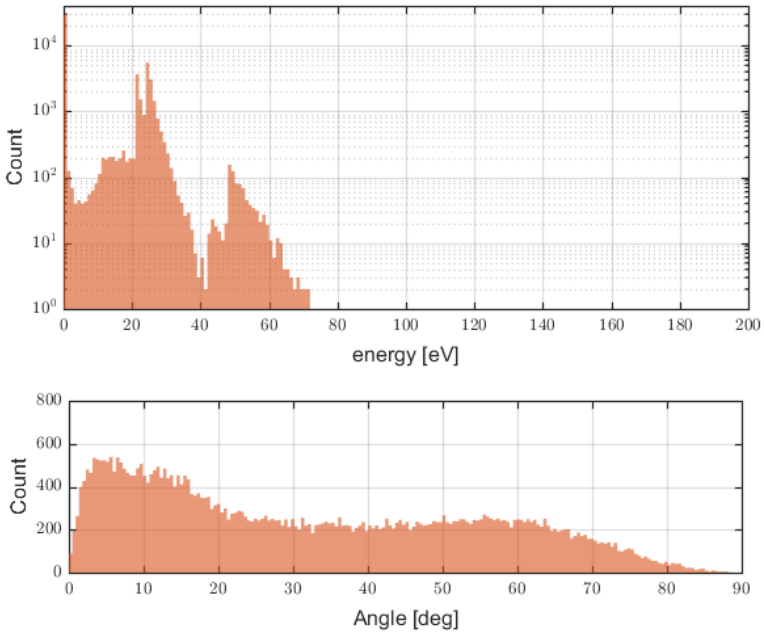

Figure 5.18: Angle and energy distributions of the impurities at the impact with GyM structure.

energy peaks at around $22eV$, $24eV$, $44eV$ and $48eV$. These energy peaks represent the copper particles falling on the lateral walls or on the bases of the chamber respectively. Compared to the side walls, the bases are at a higher temperature and therefore generate a sheath potential approximately $2eV$ higher than that of the side walls. The peaks are coupled two by two, one a multiple of the other, because each of them represent the distribution of Cu^{+} and of the Cu^{2+} respectively which sees a double sheath potential compared to the other ion.

Regarding the incidence angle distribution, we see two important peaks, the first at small angle, with a maximum at about 5^o, while the second less marked with a maximum that is about between $50^o - 60^o$. The less marked contribution is that given by the fall of the particles on the side walls, which receive particles with more variable angles of incidence. The contribution to small angles of incidence instead is given by the bases, which see arrival trajectories mainly normal to their surface, for geometric and transport reasons.

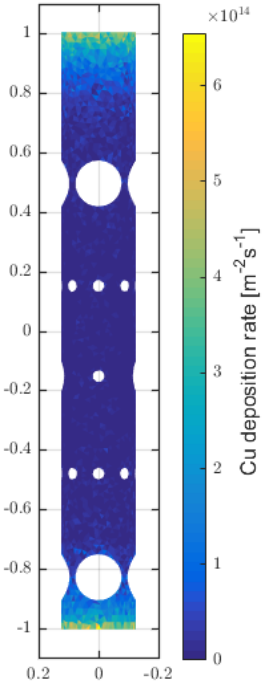

Figure 5.16: Deposition rate of the impurities on GyM lateral walls $[m^{-2}s^{-1}]$.

5.1.6 Sensitivity analysis neglecting charge exchange reactions

Here we want to put the attention on the topic of the precision with which the background plasma must be calculated, giving the example of what would happen if charge exchange reactions were neglected in the plasma balance. We have therefore made a comparison based on the plasma generated in *run 7.S* where we neglected the effect of these reactions. As an example, we report the erosion of the bases and bushings calculated with the more refined mesh introduced previously.

Here it can be easily observed how the effect of the temperature increase, excluding charge exchange reactions, affects erosion. The bases were formerly eroded only in the center and along an annulus, but now

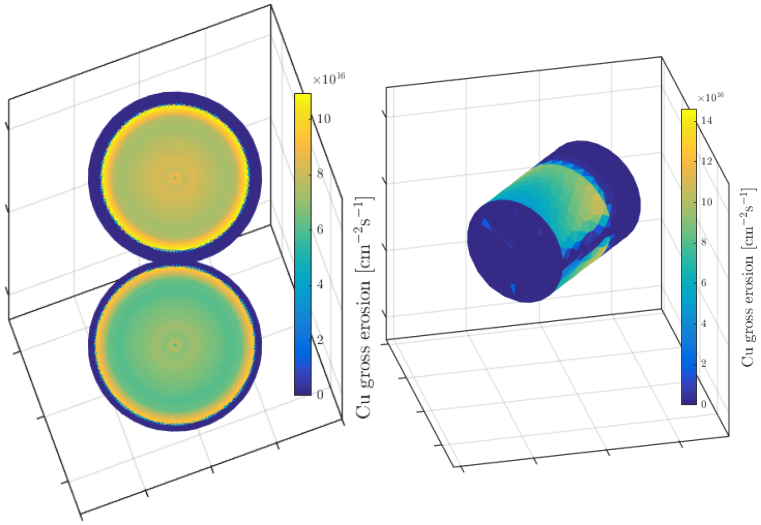

Figure 5.19: Erosion rate on GyM bases and bushings $[m^{-2}s^{-1}]$, sensitivity analysis neglecting the charge exchanges.

almost the entire surface of the base undergoes erosion. Furthermore, the bushings are now eroded whereas this did not happen before. The increased sputtering in this case is due to the increase in electronic temperature, as it can be seen in Figure 5.1. This temperature rise, increases the sheath potential [13], bringing the bushings to a condition where the copper can be eroded by the plasma.

5.2 Enhancing the erosion: applying the bias to the surfaces

In this section the possibility of the ERO2.0 code to increase the bias potential on the internal surfaces of the GyM chamber has been explored. A bias potential was applied to the bases and bushings, at different intensities, to analyze the effect it had on erosion and on the behavior of eroded impurities. We recall that from the experimental point of view, the application of a bias potential to the plasma exposed target it is one of the techniques used to study physical phenomena in the PWI research. Applying a bias is also a way to intentionally enhance the erosion of the surfaces, to study for example sputtering even on materials with very high sputtering thresholds [66].

5.2.1 Erosion analysis: beyond thresholds on basis and bushings

We begin also in this case with the study of the effects on the erosion of applying a bias potential to bases and bushings surfaces. Increasing bias potential was applied of $20V$, $100V$ and $200V$, respectively. Here we are not going to inspect all the chamber surfaces, but we will only analyze the most important aspects. We can start by looking at this Table 5.1.

We can observe the quite reasonable increase in total erosion, which increases by almost five orders of magnitudes if we compare the data

	$0V$	$20V$	$100V$	$200V$
Self-sp. $[s^{-1}]$	$3.31 \cdot 10^{11}$	$1.06 \cdot 10^{15}$	$3.32 \cdot 10^{16}$	$1.35 \cdot 10^{17}$
Plasma $[s^{-1}]$	$8.98 \cdot 10^{13}$	$2.72 \cdot 10^{17}$	$1.75 \cdot 10^{18}$	$3.60 \cdot 10^{18}$
Total $[s^{-1}]$	$9.01 \cdot 10^{13}$	$2.73 \cdot 10^{17}$	$1.78 \cdot 10^{18}$	$3.74 \cdot 10^{18}$
Self-sp. fraction	0.37%	0.39%	1.86%	3.61%

Table 5.1: Contribution of self-sputtering and plasma sputtering to the total erosion rates, absolute values and self-sputtering fraction varying the bias.

at zero bias and that at $200V$. Another comment that can be made is related to the increase in the self-sputtering fraction with respect to the total erosion as the bias increases. In fact, the number of eroded particles present in the machine increases, while that of plasma particles remains constant. Another consequence to the increased weight of erosion due to self-sputtering can be seen by observing the following Figure 5.20, which represents the total erosion of the bases of the GyM chamber as the bias varies.

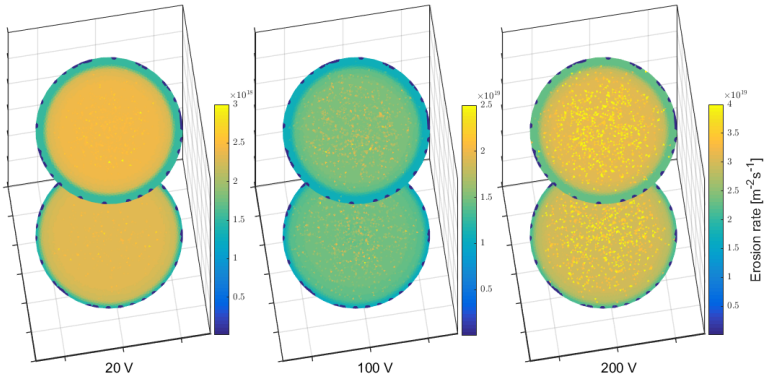

Figure 5.20: Erosion rate on GyM bases $[m^{-2}s^{-1}]$, effects of the increasing bias on the erosion pattern.

Also here we used different scales because it was not possible to have the same scale for all three images and to be able to grasp the progress of the erosion. It can be noted, as already observed, that the erosion due to the eroded copper particles increases compared to that of the plasma, in fact we see more and more marked punctual contributions as the applied bias increases. This is a clear sign of erosion from eroded particles, which is less regular in profiles than that from plasma. We can also see that the sputtering threshold for the copper base is exceeded at $20V$. There is no longer a clear distinction between the eroded and non-eroded area. This is because with $20V$ we are above the sputtering threshold everywhere on the base. In fact, calculated Eckstein sputtering yield for copper is about $16eV$ [42].

5.2.2 Decreasing ionizations

Let us now see the effect that the application of the bias has on the ionization degree of the impurities. We have summarized the calculations in the Table 5.2. The percentages have been calculated starting from the data on the particle that collide on the GyM internal structure. The percentages represent the probability that a particle with a certain charge will collide with the structure of the chamber. At 200 V, for example, we see that if we take the number of particles that collided with the internal structure of GyM, about 82% was neutral.

	Cu	**Cu^+**	**Cu^{2+}**
$0V$	57,2%	41,0%	1,8%
$20V$	79,6%	19,5%	1,0%
$100V$	82,5%	16,5%	1,0%
$200V$	82,5%	16,8%	0,7%

Table 5.2: Population fractions of the particles at the impact with the internal surfaces of GyM, effect of the application of the bias.

We can easily see that as the bias applied increases there is a progressive decrease in the degree of ionization of the eroded particles, as if as the bias increases they tend to be sputtered with a higher velocity, so to remain less time in the plasma, lowering down the probability of being ionized.

5.2.3 Effects on the incident angle distribution of the impurities

A datum that goes in the same direction as what has just been said, is represented by the incidence angle distribution of the particles, reported in the Figure 5.21. The figure shows the incidence angle distributions as the bias varies. We have also reported the angle distribution of copper at zero potential for completeness, to show the gradual effect of bias application to the surfaces.

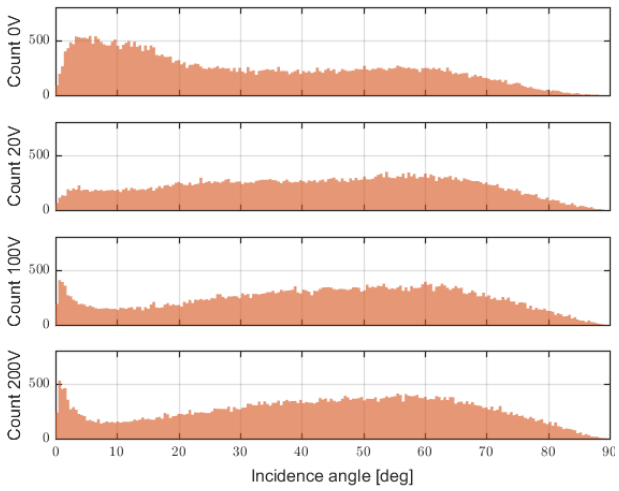

Figure 5.21: Incidence angle distributions of the impurities at the impact with GyM structure, effect of varying the bias.

We can observe that initially the bias appears to have the effect of lowering the peak at small angles, absorbing it in the distribution at higher angles. This can be interpreted as a sign that the copper impurities are redeposited more on the walls and the peak at small angles is completely absorbed by the increased re-deposition on the walls. By increasing the bias, the contribution of re-deposition on the bases becomes visible again, in fact now the applied potential is strong enough to bend the impurities' trajectories close to the normal incidence on the bases, which results again in a variation of the distribution profile. The distributions at $100V$ and $200V$ do not seem to be very different, which means that the behavior of particles in the two situations is similar.

5.2.4 Effects on energy distributions of the impurities

After having analyzed the incidence angle distributions, let us move on to analyze the graph of the energy distributions. We recall that in Section 5.1 we observed the presence of well-defined peaks to represent the impacts of the particles on the two main surfaces affected by the re-deposition phenomenon: the bases and the lateral walls. Now that we have applied a bias potential to the chamber bases and the bushings, we expect to see a shift of the peak representing the bases (and in this case also the bushings because the bias is also applied here) at higher energies. Let us see the energy distributions in the Figure 5.22

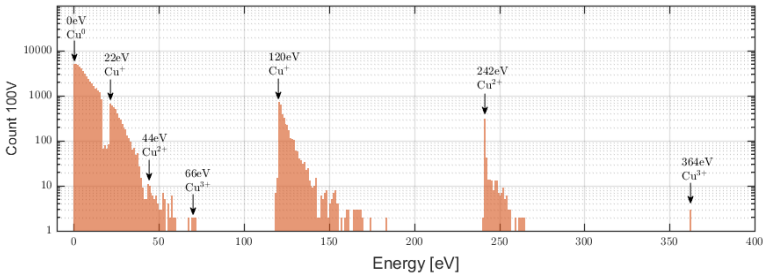

Figure 5.22: Energy distribution of the incident impurity particles with GyM internal structure, applied bias to bases and bushing of $100V$.

As an example we have taken the power distribution of copper at $100V$, because it seems to be the most instructive for our purposes. We observe that by increasing the bias, some charged species are now represented by distinct peaks, shifted with respect to the situation without bias applied. Applying a bias of $100V$ to the bases and bushings of the chamber we observe that the peaks previously found at $24eV$ and $48eV$, which represented the impact of the Cu^+ and Cu^{2+} on the bases and on the bushings, are now shifted by approximately $100V$. Peaks due to the impacts of the ions at different charges are visible, respectively those ionized once, twice and three times. At low energies we see the peak of the neutral species and the peaks referred to the ions Cu^+, Cu^{2+} and Cu^{3+}. From the height of the Cu^{2+} peak we can see that this ion tends to redeposit on the bases, rather than on the side walls. The Cu^+ seems to settle equally on the two surfaces. It is interesting also to see the energy distribution of the particles once they are sputtered, in Figure 5.23

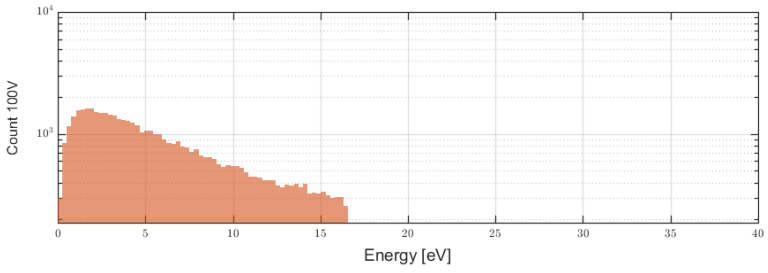

Figure 5.23: Energy distribution of the impurity particles at the release from GyM internal structure, applied bias to bases and bushing of $100V$.

The energy distribution at the start shows a cut at high energies because the energy with which the particles are emitted from the surface is physically limited at the top. This limit is higher the more effective the collisions between the light plasma ions He^+ and the copper atoms are. If the solid surface atom were lighter, the collision with the helium atoms would be more effective and the maximum transferable energy with the collision would increase.

5.3 Changing the material of the chamber: tungsten and carbon

In this section the possibility of changing the material of the chamber of which the GyM linear machine is made has been explored. We then went on to analyze some of the characteristics of the erosion as in the previous sections, taking into account the peculiarities of each considered material. We have chosen two different materials in addition to copper: carbon and tungsten. So let's first analyze some of the properties of these materials and also give a justification to the simulation work carried out on the basis of their use from an experimental point of view.

5.3.1 Motivations to the choice of the two materials and some relevant physical quantities

The choice of using carbon and tungsten as copper substitute materials for the GyM chamber is linked to several reasons, which we now present. Carbon is one of the two materials of which stainless steel is made, but the choice of this material for the internal chamber of GyM is not very related to this. The reasons are mainly related to the fact that historically both carbon and tungsten were used for the construction of surfaces in contact with plasma, such as limiters and divertors [65]. To understand the reasons why they are used, i. e. refer to [79] and [80]. Furthermore, as far as the experimental activity of GyM is concerned, there is another reason why there is the interest of studying a material such as tungsten. In fact, for GyM there is the possibility of inserting a tungsten cylindrical *liner* (supported by the bushings) inside the machine and knowing how to simulate this type of material is certainly a matter of interest.

Let us now analyze the main characteristics of these two materials. Carbon is the element of the periodic table which corresponds to an atomic number of $Z = 6$, while tungsten has a much higher atomic number, $Z = 74$. Carbon and tungsten atoms have atomic masses of $12.01u$ and $183.84u$, respectively. The copper considered so far ranks between these two materials as regards the atomic weight. Since the maximum transferable energy in an elastic collision between two particles depends on the relative colliding masses and since it grows if the two masses are comparable, we will see that helium collisions will be more effective for carbon and less effective with tungsten. This will have particular importance in determining the energy distributions of the sputtered particles. The ionization energy is also an important parameter in determining the behavior of impurities. In fact the lower it is, the more easily the impurity atoms will be ionized and consequently more easily carried around by the magnetic field of the machine. The ionization energy decreases in general as the atomic number of the material increases and for carbon it is $11.26eV$, while for tungsten it is $7.98eV$. The second ionization energy, which is important to understand a priori the potential presence of higher charge states for impurities, is $24.38eV$ for carbon while $17.62eV$ for tungsten. To complete the list of properties of the two materials useful for the analysis we will do, we report in Figure 5.24 the experimentally measured sputtering yields (and fitted) from [42].

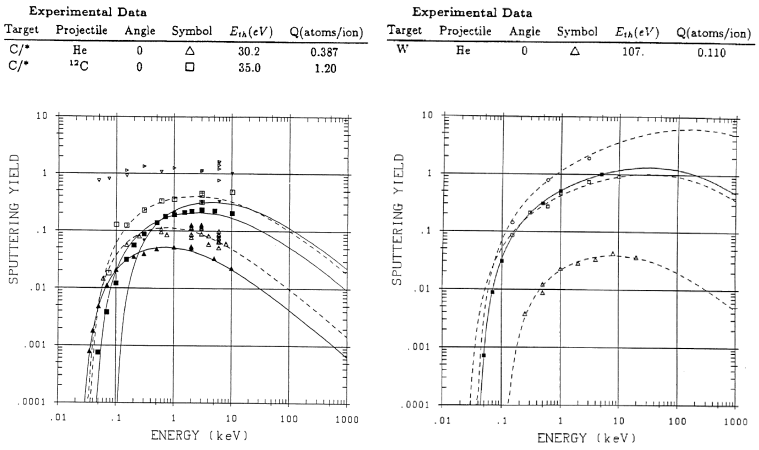

Figure 5.24: Carbon (left) and tungsten (right) Eckstein sputtering yield [42]

5.3.2 Global erosion analysis: inspecting thresholds and presence of charged particles

Similarly to what was done in Section 5.1, let us analyze the result obtained if the background plasma is used including all the reactions' contributions (*run 8.S*) in a chamber made of carbon or tungsten. The main differences from a general point of view, compared to copper simulation, are to be identified in two aspects: the difference in the sputtering thresholds and the presence of charged impurities. Let us analyze the issue of sputtering thresholds. Carbon under these conditions (*run 8.S* plasma, null bias applied) is eroded by the plasma, while tungsten is not eroded. In order to initiate the erosion of this material, a bias potential of $110V$ had to be applied. We see in Figure 5.25 the representation of the erosion of the surfaces of the carbon bases and bushings.

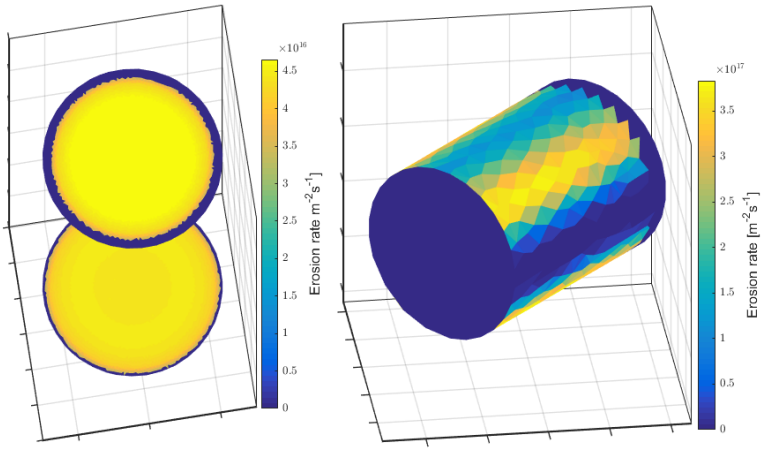

Figure 5.25: Erosion rate on GyM bases and bushings $[m^{-2}s^{-1}]$ using carbon as structure material.

What we observe is that for carbon the sputtering thresholds are exceeded on the whole base and also the bushings are affected by erosion, unlike what happened for copper. However, if we look at the tables in Figure 4.2 and in Figure 5.24 and compare the experimental data, we see that the threshold energy for having sputtering for copper ($18eV$) is lower than that of carbon ($30.2eV$). This suggests once again that greater accuracy of the data at low temperatures may be required for the copper sputtering threshold.

Let us now move on to a second question and that is the degree of ionization of the impurities present in the machine. As before, we calculated in the Table 5.3 the percentages of presence of certain charge states among the particles impinging on the internal structure of the GyM machine. We took as a reference three simulations where the bias was set at $200V$ on bases and bushings, to increase erosion and the consequent presence of eroded particles.

Charge state	0	1	2	3	4
C	97.3%	2.6%	0.04%	0%	0%
Cu	82.5%	16.8%	0.7%	0%	0%
W	58.4%	31.6%	8.3%	1.5%	0.2%

Table 5.3: Population fractions of the particles at the impact with the internal surfaces of GyM, for different materials with applied bias to bases and bushings of $200V$.

As we can see from the data, as the ionization energy decreases, the presence of ions at different charge states increases. Tungsten is the material that is most ionized and this depends precisely on the fact that it is an atom with many electrons, extracting one is much easier than in the case of copper and carbon. In fact, carbon ionizes very little, the 97.3% of the particles collides with the structure still in the neutral atomic carbon state. This has important repercussions on the transport of particles, which we will analyze in the second part of this analysis. Before we do this, let us look at another aspect of erosion.

5.3.3 Erosion angle pattern: the case of the bushings

If we isolate the erosion due to plasma alone on the bushings when the considerable bias of $200V$ is applied, we can observe a pattern of erosion that varies as the material changes. In fact, let us look at the Figure 5.26.

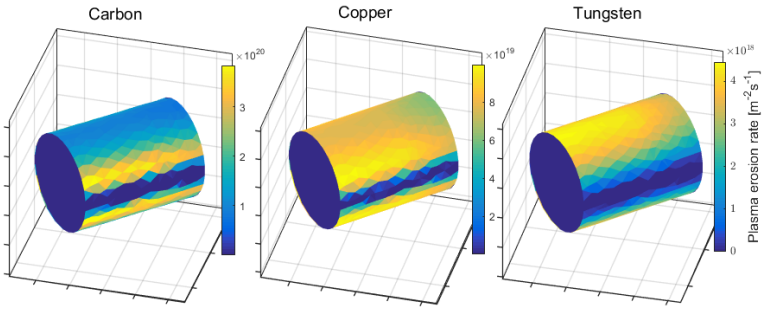

Figure 5.26: Angle pattern of the erosion rate due to plasma on GyM bushings $[m^{-2}s^{-1}]$, comparison among the three different materials: carbon (left), copper (middle) and tungsten (right), applied bias of $200V$ to the bushings.

We took the plasma contribution only because the erosion due to the charged particles would not have been so regular on the surface of the bushings. In the figure the overall erosion are different, but here we are interested in seeing how the position of the maximum erosion point varies as the material varies. Each material has an increasing sputtering yield as the angle of incidence of the plasma increases. Furthermore, the plasma flow on the surface of the bushing varies as the angle of incidence with the surface varies. Here we can observe the erosion result as the net effect between reducing plasma flow and increasing yield as the angle of incidence increases, and one thing or the other prevails depending on the material. On the three materials, we see that as the plasma angle of incidence varies, the point of maximum erosion appears to shift from

incidence angles of over 45^o for carbon to nearly normal incidence angles as for tungsten.

5.3.4 Erosion and deposition fractions of the impurities

After talking about the characteristics of the materials taken into consideration and how they affect the degree of ionization of the impurities, let us see another consequence of the different ionization energy of the particles. We have collected in the Figure 5.27 data on erosion by impurities only, depending on the material and the applied bias. In particular, the fraction of total erosion coming from the bases (with the darker color), from the bushings (intermediate color) and from the side walls (with the lighter color) was represented.

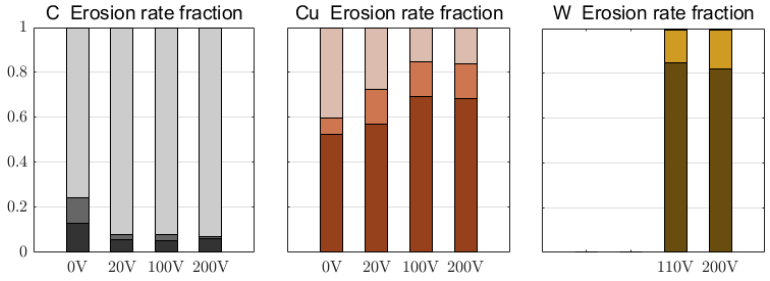

Figure 5.27: Erosion fraction, surfaces comparison. Structure are indicated as: bases (darker color), bushings (intermediate color) and lateral walls (lighter color). Comparison among the three material varying the bias.

For tungsten there is no erosion data for bias below $110V$, as previously mentioned. We can see that increasing bias for carbon has the net effect of decreasing erosion on bases and bushings, while for copper the opposite is true. Tungsten always sees very low erosion of the walls (almost imperceptible from the graph), the contribution of erosion of the bushings increases by no more than 10%.

From these observations we can say that the increase in bias serves for copper mainly to increase the energy of the ions which, after being transported, return to bases. In the case of carbon, on the other hand, it increases the energy that neutral atoms receive when leaving the wall after being sputtered. Both of these effects occur in both situations, but depending on the material one effect prevails over the other. This effect is certainly still an aspect of the materials' different ionization energy, much higher for carbon than for copper. To confirm this explanation and to highlight other aspects related to this, we will then analyze the energy distributions of the impurities that fall on the internal structure of GyM. Now we still remain on the calculation of the fractions, going to see the fractions of material re-deposition on the internal surfaces as the material and the bias in Figure 5.28

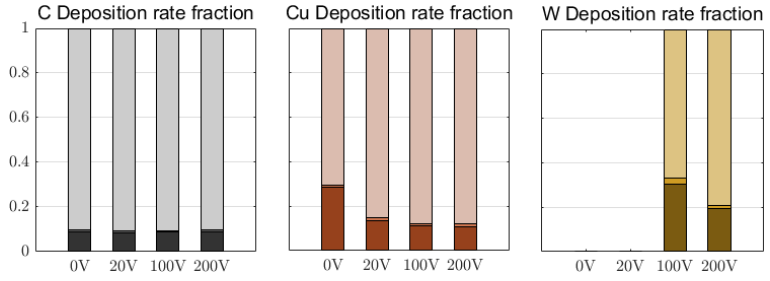

Figure 5.28: Re-deposition fraction, surfaces comparison. Structure are indicated as: bases (darker color), bushings (intermediate color) and lateral walls (lighter color). Comparison among the three material varying the bias.

Looking at these three graphs, we can see that increasing the bias it reduces the probability of ionization of copper and tungsten, as already seen in the Table 5.3, because it increases the probability that the impurities go on the walls, without following the magnetic field. This fact can be explained in this way: the particles eroded by the structure as neutral, now have a higher kinetic energy at the start and therefore remain for less time in the plasma. This decreases the likelihood that they will be ionized before redepositing on the internal structure of the chamber. However, the net effect on global erosion is to increase erosion on bases, because the bias potential makes self-sputtering reactions very effective.

5.3.5 Plasma-wall collisions: broadening energy peaks of the impurity energy distributions

We now see the energy distributions to confirm what we said above, both in the graphs of the erosion and deposition fractions, and on the presence of the ionized states of the materials. The Figure 5.29 shows the energy distributions of the impurity particles at the impact with the internal structure of the GyM chamber. We can see the distributions of the three materials all taken in the case of applying the $200V$ bias.

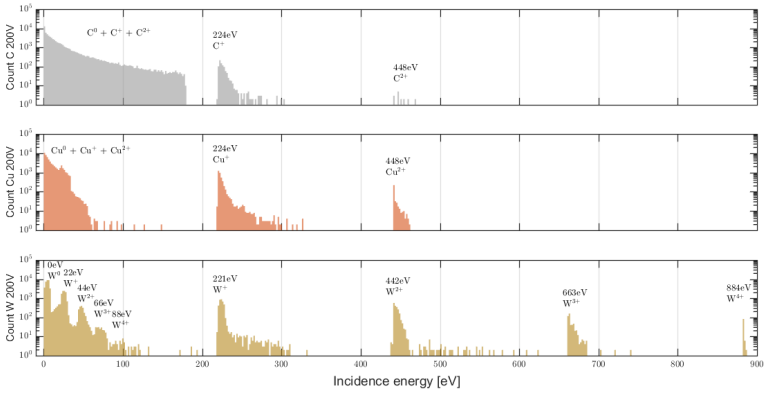

Figure 5.29: Energy distribution of the incident impurity particles with GyM internal structure. Comparison among the three materials: carbon (upper), copper (middle) and tungsten (lower). Applied bias to bases and bushing of $200V$.

Let us start by observing the degree of ionization of the impurities in the three cases. We can see that tungsten peaks are very marked, while those of copper and carbon are gradually less marked. This is a symptom of the different degree of ionization of the impurities, again due to the different ionization energy of the materials. Let us look at the carbon distribution: it has a very regular profile up to $200eV$, until it collapses before reaching $200eV$. This trend is given by the distribution of the eroded particles departing from the surfaces from which they have been eroded. These particles being poorly ionized, still fall on the surfaces as neutrals. Only very few particles are ionized to become C^+ and C^{2+} ions. They then gain energy thanks to the bias potential and the respective peaks are visible in the graph. The energy peaks that should represent the carbon ions falling on the walls, similar to the peaks we observed for copper in the Figure 5.22 are completely absorbed by the neutral distribution. Speaking of copper, we can see how the ionization is more marked than in carbon. We can also note that, compared to the distribution in Figure 5.22, the contribution to lower energies has increased, precisely due to the fact that more neutral atoms fall on the internal structure of GyM

without being ionized. Looking at tungsten, we see that the effect of the greater ionization is here extreme: the energy distribution presents evident peaks in correspondence with the different charge states of the material, depending on whether it falls on the side walls (where the bias of $200V$ is not applied) or on the bases.

A final comment on energy distributions can be made regarding the effectiveness of the energy transfer in the impact causing the sputtering. As we have said, the regular low-energy profile seen for carbon is mainly due to the collisions of the neutral particles on the internal structure of GyM after being sputtered. The cut that can be seen at about $180eV$ is due to the fact that, following an elastic collision between particles of different mass such as carbon and helium atoms, only a fraction of the energy of the helium can be transferred to the carbon. Therefore, as the mass of the target atom increases (passing from carbon which has only three times the mass of helium, up to tungsten, which has about 46 times greater) we observe that the extension of the distribution is progressively reduced.

5.3.6 Angle distributions of the impurities: bending the charged particles increasing the bias

For completeness we also see the distributions of the incidence angles of the impurity particles. Here we have chosen to represent, in Figure 5.30, the distributions per bias of $200V$.

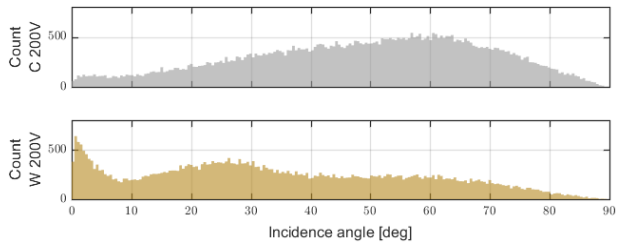

Figure 5.30: Incidence angle distribution of the impurity particles at the impact with GyM internal structure. Comparison among the two materials: carbon (upper) and tungsten (lower). Applied bias to bases and bushing of $200V$.

We have represented in the upper part of the figure the carbon incidence distribution and in the lower part the tungsten one. Observing the graphs and remembering that the low energy peak represents more the bases, also in this case we see that the carbon is redeposited more on the walls, while the tungsten which is affected by the magnetic field is pointed towards the bases, following the field lines.

5.4 Restricting the plasma: varying the extrapolation

We move now to a final issue and that is a sensitivity analysis of the model with which the data are extrapolated from the SOLPS-ITER mesh to the ERO2.0 mesh. We remind that, since the SOLPS-ITER mesh is narrower than that of the ERO2.0 code because it does not touch the internal structure of the machine, it is necessary to perform an etrapolation of the plasma data up to the wall of the simulated machine. Once the extrapolation has been performed, the data can be taken as input from

the second code. To extrapolate the data, there are many possibilities, and as explained in Section 4.1, some of these are made available to the user when working with the dedicated routines. The extrapolation method used so far, as already reported, is the *nearest projection method*, which practically consists in assuming that outside the cells of SOLPS-ITER the data is equal to that of the last cells at the edge of the mesh. What we want to do here is to use the *exponential method* that consists in extending the data by imposing an exponential decrease as we move away from the edge of the inner mesh. The exponent of the function is not defined *a priori* but is made to vary to see the effects it has. The reason why this section has been inserted here is that the plasma used in this case is different from the plasma generated in the *run 8.S* used up to now, it is radially narrower and this allows to better observe the different extrapolations. Let's first understand the logic behind the narrower plasma on the SOLPS-ITER side.

5.4.1 Comparison with extended case: radial profiles of relevant physical quantities

If we look at what we made in the Chapter 3, we can notice that the problem of how the presence of the bushings could modify the simulation results has never been raised. In fact, the mesh we have used so far extends to be close to the GyM lateral wall but the bushings have not been included. However, we also know that, since SOLPS-ITER is a 2D code, it is not possible to include objects that have a three-dimensional extension in the two-dimensional geometry (of the poloidal section) in which code B2.5 works. What is the best way to treat the bushings from a conceptual point of view to go in the direction of simulating a condition similar to the real one, can be considered an open question. What we have done here was simply to consider the extreme case complementary to the one in which the bushings are completely neglected. They have been inserted in the two-dimensional geometry and then treated by the code as if they were rings with an axis coinciding with that of the cylindrical chamber (and then treat them as if they were limiters for a tokamak). This case certainly overestimates the presence of the bushings, the *real situation* is definitely somewhere between these two extreme cases.

Having inserted other elements in the two-dimensional geometry of the chamber required the modification of the SOLPS-ITER mesh, which was restricted to avoid intersecting the new elements inserted in the chamber. With SOLPS-ITER a new simulation was carried out, with the restricted mesh, in which it was established that the power introduced from the outside was the same as in the previous case, which we remember to be $540W$. From here on, we will refer to the restricted mesh simulation as *run 9.S*. As we did for the extended simulation plasma (*run 8.S*), we are going to quickly analyze the restricted mesh simulation plasma (*run 9.S*) in the Figure 5.31, highlighting the differences.

As in the Figure 5.2, the radial trends of the most relevant quantities of plasma have also been reported here. We see that by shrinking the plasma there is an increase in the electron density, correlated to a decrease in the electron temperature. The rise of the electronic temperature causes the ionic temperature to drop as well. The lower electronic temperature also

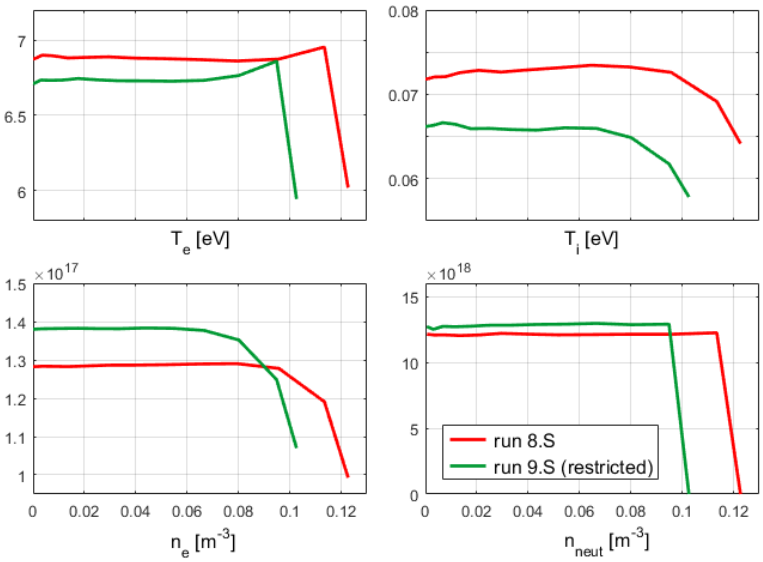

Figure 5.31: Radial profiles of the electron and ion temperatures T_e, T_i $[eV]$, electron and neutral densities n_e, n_{neut} $[m^{-3}]$. Comparison between restricted (green) and extended (red) plasmas.

causes the plasma to be less ionized, as a result we see an increase in the density of neutrals inside the chamber. Although these quantities change in mean value, the qualitative trend of these quantities that would be seen from the 2D density and temperature patchplots would remain similar to that of the extended case (*run 9.S*). For this reason, only these quantities have been reported. The lower electron temperature, as far as we know from the sensitivity analysis made by neglecting the charge exchange reactions, we expect to be reflected in a further lowering of the overall erosion of the surfaces facing the plasma.

5.4.2 Effects of the extrapolation on the results in the most sensitive case: carbon

Let us now change the model of extrapolation of the SOLPS-ITER data on the ERO2.0 mesh. As an example, the bases of the GyM chamber were represented in the Figure 5.32, where the extrapolated electron temperature was plotted as the exponent of the extrapolating exponential function was varied. The generic quantity extrapolated with this model is a function of the type

$$f(x) \propto e^{-\frac{x}{\lambda}}$$

where x is the coordinate in the radial direction taken from the outer boundary (so $x = 0$ on the boundary) and λ the parameter that the user can specify, which is the object of the analysis here. λ has the meaning of representing the characteristic length of variation of the physical quantities of the plasma at the edge. One falls back into the case of nearest projection if it sets $\lambda = \infty$.

In the figure we start from the leftmost case, the one with $\lambda = \infty$ until to the case with $\lambda = 0.1cm$. As one might expect, we see that as λ varies, the effectiveness with which the exponential function causes the data to decrease beyond the SOLPS-ITER mesh also varies. In the case where $\lambda = \infty$ we see an extension of the data up to the wall, taken constantly

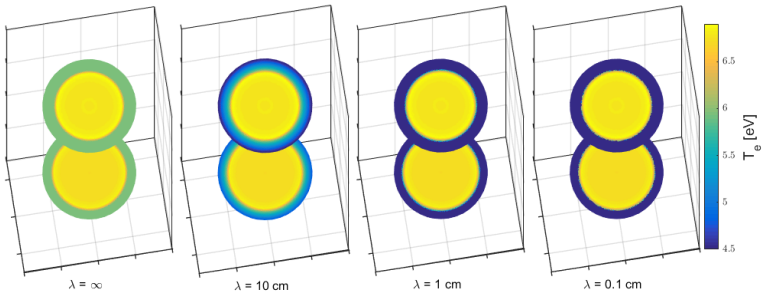

Figure 5.32: Electron temperature T_e $[eV]$ on the GyM bases, comparison among four different extrapolations varying the exponent of the exponential extrapolating function outside SOLPS-ITER mesh.

starting from the outermost cell. In the case of $\lambda = 0.1cm$ the data is set to null almost immediately after the last cell of SOLPS-ITER. Starting from these boundary conditions, the erosion analysis was carried out similarly to what was done in the previous parts of the chapter. Carbon was used as the material, as the electron temperature decreased further and this appeared to be the most sensitive material to low electron temperatures. The result of the erosion of the bases is reported in Figure 5.33.

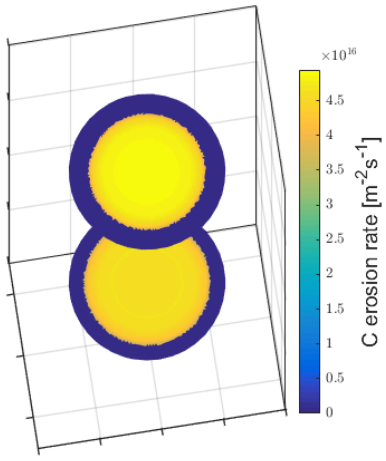

Figure 5.33: Erosion rate on GyM bases $[m^{-2}s^{-1}]$ using carbon as structure material and the restricted plasma.

The figure is only one because the erosion pattern is the same regardless the used extrapolation method. It was not possible to see any change in the pattern because changes in the electron temperature depending on the choice of the extrapolation length do not result in overcoming of the sputtering threshold for the material. This erosion pattern is similar to the one in Figure 5.25, we see that the area affected by erosion is smaller due to the reduced extension of the plasma compared to the previous case.

5.5 Limits of this modelling

As already pointed out at the beginning of Section 5.4, the constraint of being able to use only two dimensions for the definition of the reference geometry of SOLPS-ITER leaves some open questions. First of all is that of identifying which is the best direction if you wanted to go for example in the direction of simulating the operating conditions of GyM as faithfully as possible. But then, if we talked about issues related to the limits of the use of cylindrical symmetry we would have to open a whole other series of questions that in this thesis we have not even mentioned, for

example the pumping surfaces for the vacuum or the radiofrequency source. If one looked only at this question of the bushings, wanting to model a close-to-real-situation of GyM, there would be the risk of trying to improve something that perhaps has a truly negligible weight in the overall limits of the model.

Always connecting to this, we can also discuss an equally important question: what is the weight of impurities in determining the behavior of plasma? In this work we have taken care to give ERO2.0 the plasma conditions for the calculation of the erosion and the transport of the eroded particles. The plasma, in all this work, has never been updated starting from the data obtained with ERO2.0. Understanding the importance of this question is certainly just as important as the earlier discussions on cylindrical geometry.

Furthermore, even the SOLPS-ITER equations, not having been created with the intention of being applied to cylindrical geometry, have some limitations if applied in these cases. First of all the issues we had already mentioned in Section 3.1, where important aspects related to the reference system were underlined.

The question of the material of which GyM is made is also another question of fundamental importance. For a precise model of GyM operating conditions it would be necessary to have the sputtering yields of the stainless steel, which as we have already said in Section 4.2 is not trivial.

These are just examples of the important limitations of this model, if we went into the specifics of each issue there would be many more issues to talk about. But it is very important before doing it, to have an overview to understand which issues are priority and which are not.

5.6 Summary

Now let us briefly summarize the main results that have been obtained in this chapter. We first analyzed the background plasma constructed from the results of Chapter 3. We started with the volume averaged quantities and then moved on to the analysis of the radial trends of the main plasma quantities: population density profiles, particle fluxes and thermal fluxes at the machine bases were analyzed. Here we have found elements already analyzed previously, such as the activation of friction forces due to charge exchanges or the increase in thermal exchanges due to the excitations of the neutrals. We also stressed the importance of having an accurate plasma model by performing a sensitivity analysis that did not include charge exchange reactions. It was found that at low temperatures, the sputtering thresholds are very sensitive and the plasma reactions' setup must be carefully considered.

After the plasma, we analyzed the internal surfaces of GyM one at a time. We have observed that the bases are affected by erosion only in some places and that it would be useful to have more refined data about the copper sputtering yield at low temperatures. The erosion of the bushings and of the lateral walls seems to be orders of magnitude lower than that of the bases and therefore negligible in the first place. The contribution to the total erosion is mainly due to the plasma while the

self-sputtering erosion under normal operating conditions of GyM is negligible compared to this. If, on the other hand, it is decided to apply a bias potential to the bushings, it is seen that the contribution of erosion increases considerably and that the erosion due to the impurities begins to be important.

We have studied the effect that the application of the bias has on the degree of ionization of the impurities, on the energy distributions and on the incidence angle distributions at the impact with the structure. The formation of peaks in the energy distributions at energies equal to the sheath potential was observed. By varying the material, it was also possible to observe how the different masses and the different ionization energy of each material affected the degree of ionization of the impurities and their behavior. In particular, it has been observed that if a bias potential is applied, the eroded species tend to arrive much more on the walls, a sign of the fact that the greater energy of the sputtered particles decreases the probability of being ionized by the plasma. We have also seen how the application of bias, in the case of copper, mainly serves to increase the energy of the ions returning to the bases, while for carbon it increases the energy that neutrals receive when leaving the surfaces. We have also observed how the sputtering varies as the angle of incidence varies, taking as an example the pattern of erosion by the plasma on the bushings. We observed an increase in the maximum sputtering angle of incidence as the mass of the target atom decreased.

Finally, a restricted plasma was generated with SOLPS-ITER with the intention of studying a situation where the bushings were not neglected a priori in the plasma generation. This plasma was used to study the effect of changing the extrapolation model on the results calculated with ERO2.0. We have seen that the model is correctly implemented by the code but that there are no differences in the erosion pattern due to the extrapolation model. This study was done in the most sensitive case, carbon, which ensures that the result would also be similar for the other two materials, copper and tungsten.

6 Conclusions and Perspectives

The final goal of this thesis was to study the erosion and the migration of the eroded impurities in the context of helium plasmas in linear plasma devices. This aim has been achieved by coupling the SOLPS-ITER plasma edge code with the ERO2.0. We recall that a coupled simulation of this type in the context of linear plasma devices has not yet been published in the literature.

This work was divided into three steps. First, presented in Chapter 3 it was addressed the issue of evaluate the adequacy of the reaction setup for the application of SOLPS-ITER to helium plasmas in linear machines. Changes were suggested regarding the choice of databases for the calculation of ionization reactions. Then the effects of elastic scattering and charge exchange reactions were analyzed. Finally, the contribution of neutrals excitations by electron collisions was also analyzed. The main results of this first part were:

- As for the ionization reactions, it was found that results obtained using the database chosen by default differed from those provided by more recent databases. Greater precision in the results was achieved by interpolating the reaction rate data not only on the basis of the electronic temperature, but also on the density.
- For the elastic scattering reactions, it was found that they do not play a significant role in the balance if we are in a too low temperature situation.
- Charge exchange reactions between neutral and ion populations has the effect of activating a collisional drag for the ions. This has a particularly relevant effect on the plasma and so it is recommended to include this reaction in the balance.
- The effect of including in the balance the excitations of neutral atoms has also a significant repercussions on the behavior of the system and it is recommended to include this possibility within the framework of the electron impact ionization reactions with neutral species.

The results of this work were reported to the SOLPS-ITER developers and included in subsequent code changes.

In the second step, in Chapter 4, a work was done to convert the SOLPS-ITER data into the format readable by the ERO2.0 code, using routines and scripts appropriately modified for linear geometry machines. Here, particular attention was paid to the method of extrapolation of the data between the narrower mesh of SOLPS-ITER and the extended one of ERO2.0.

In addition to this, other issues concerning purely the ERO2.0 side has been addressed. One of these was to justify the choice of copper as the material with which to simulate the GyM chamber. A second issue was the identification of the most important parameters for the construction

of a simulation with ERO2.0 that would satisfy our analysis needs. In this work, the main results obtained were:

- The importance of using a sufficiently refined mesh in the areas of greatest interest to the study of phenomena such as erosion and deposition.
- The computational cost associated with the mesh refining is not an issue in our case. The increase in computational time is not unreasonable in the face of the better quality of the result obtained. Furthermore, by using a single time step, computational times are considerably reduced but this strong approach must be verified *a posteriori*.
- The number of test particles chosen (50.000) is sufficient to guarantee a good statistical representation of the real particles.
- The use of the single time step for the simulation guarantees the achievement of an equilibrium situation, the results do not change even if you take many more time steps.

In the third and last step, in Chapter 5, a first simulation coupled between the two codes has been performed. After analyzing the results of the simulations on the plasma side, some aspects of the erosion phenomena and transport of the eroded particles inside the linear machine were analyzed. After this, other modeling possibilities available from ERO2.0 code were explored. Among these, we analyzed the characteristics of erosion and impurity transport when a bias potential is applied to some surfaces, or when the chamber material is changed. It was observed how the different properties of the materials affected the results. Finally, we faced the problem of understanding how much the different extrapolation of the plasma data coming from SOLPS-ITER influenced the results of the simulations made with ERO2.0. The main results that have been obtained in this sense were:

- The coupling between the two codes has been successfully achieved. The erosion profiles were obtained in a particular operating condition of GyM that was sufficiently representative of the experimental activities. From the simulation results, the presence of the phenomenon of erosion of the machine bases due to plasma is highlighted. However, the simulation presents modeling limits due to the absence of steel erosion data and the conclusions that can be drawn from the copper results therefore have no absolute value.
- The accuracy with which the helium plasma model is constructed is very important. In fact, variations in the electron temperature even of fractions of eV have important repercussions on the erosion results. This therefore constitutes a posteriori confirmation of the importance of the work done in Chapter 3.
- The application of a bias potential has the effect of enhance the overall erosion of the surfaces to which it is applied. It increases the presence of impurities and lowers the degree of ionization. It also modifies the energy distributions of the incident particles with the GyM structure. The effect of the bias is visible both on the energy distributions at the start, affecting the maximum energy they can reach, and on arrival, suitably shifting and creating peaks.
- The energy of the first and second ionization, together with the mass of the atom which constitutes the material of the structure of the GyM chamber, determine in an important way the behavior of

the eroded particles. In the case of carbon, the greater ionization energy threshold is reflected in the greater presence of neutral charge states. In the case of tungsten, the presence of different ionized charge states following the magnetic field lines is observed.
- The effect of the variation of the data extrapolation model from SOLPS-ITER to ERO2.0 is not appreciable in our operating condition. This is due to the fact that the temperature variations due to the variation of the extrapolation model are too small to be appreciated in the erosion pattern. The evaluation was made in the most sensitive case observed, namely that of carbon. This ensures that even if we changed the model in the case of copper or tungsten, there would be no impact here either.

In light of these results and what is written in Section 5.5 on the limits of the model, we can say that future developments with respect to this work can go in these directions:

- Understand a strategy to generate databases of materials such as stainless steel with ERO2.0, which can represent materials more used in constructing linear machines. Having stainless steel databases would certainly be of great interest as it would allow us to understand if the simulations with copper were reliable and confirm the copper results.
- Understand from both the modelling and the experimental point of view which is the best approach if we want to include in the simulations with SOLPS-ITER three-dimensional objects such as the protrusions that enter the plasma and disturb its behavior.
- Understand how much the presence of eroded impurities can modify the background plasma, both from an experimental and modeling point of view. The ideal would be to be able to carry out at least some coupled iterations between the two codes in order to evaluate whether there are important effects on the background plasma by impurities. Then to address if this leads to further modification of the erosion and transport patterns of the eroded particles.
- Achieve the simulation of the presence of a sample holder inside the GyM chamber. The presence of the sample holder is certainly a disturbing element for the plasma, as well as the particles eroded by the walls or the structure of the sample holder. It would be interesting to evaluate the influence that the particles eroded from the chamber walls have on the plasma-surface interaction experiments.

Appendix

Bibliography

Here are the references in citation order.

[1] Hannah Ritchie and Max Roser. 'Energy'. In: *Our World in Data* (2020). https://ourworldindata.org/energy (cited on pages 1, 3).

[2] Thomas R. Anderson, Ed Hawkins, and Philip D. Jones. 'CO2, the greenhouse effect and global warming: from the pioneering work of Arrhenius and Callendar to today's Earth System Models'. In: *Endeavour* 40.3 (2016), pp. 178–187. DOI: https://doi.org/10.1016/j.endeavour.2016.07.002 (cited on page 2).

[3] Nuclear Energy Agency. 'Nuclear energy in a sustainable development perspective. Technical report'. In: (2000) (cited on page 2).

[4] M Lung. 'Energy: nuclear energy; Energies: l'energie nucleaire'. In: (2000) (cited on page 3).

[5] Bull.n°62 Foratom. 'ExternE Study of the European Commission'. In: (1999) (cited on page 3).

[6] Francis Chen. *Introduction to Plasma Physics and Controlled Fusion*. 2016 (cited on page 6).

[7] Nuclear Regulatory Commission. *Backgrounder on Tritium, Radiation Protection Limits, and Drinking Water Standards*. 2016. URL: https://www.nrc.gov/reading-rm/doc-collections/fact-sheets/tritium-radiation-fs.html (cited on page 10).

[8] P-H Rebut et al. 'ITER: the first experimental fusion reactor'. In: *Fusion engineering and design* 30.1-2 (1995), pp. 85–118 (cited on pages 12, 45).

[9] R. Betti and O. A. Hurricane. 'Inertial-confinement fusion with lasers'. In: *Nature Physics* 12 (2016), pp. 435–448. DOI: 10.1038/nphys3736 (cited on page 13).

[10] Mordecai D. Rosen. 'The physics issues that determine inertial confinement fusion target gain and driver requirements: A tutorial'. In: *Physics of Plasmas* 6.5 (1999), pp. 1690–1699. DOI: 10.1063/1.873427 (cited on page 13).

[11] Andrei D. Sakharov. 'SPECIAL ISSUE: Theory of the magnetic thermonuclear reactor, part II'. In: *Soviet Physics Uspekhi* 34.5 (May 1991), pp. 378–382. DOI: 10.1070/PU1991v034n05ABEH002493 (cited on page 16).

[12] *ITER*. URL: https://www.iter.org (cited on page 18).

[13] Peter C Stangeby. *The Plasma Boundary of Magnetic Fusion Devices*. 2000 (cited on pages 20, 25–28, 81).

[14] J Rapp et al. 'Reduction of divertor heat load in JET ELMy H-modes using impurity seeding techniques'. In: 44.2 (Jan. 2004), pp. 312–319. DOI: 10.1088/0029-5515/44/2/013 (cited on page 20).

[15] Juergen Rapp. 'Addressing research and development gaps for plasmamaterial interactions with linear plasma devices. Technical report'. In: (2018) (cited on page 20).

[16] B de Groot et al. 'Magnum-psi, a new linear plasma generator for plasma-surface interaction studies in ITER relevant conditions'. In: *Fusion engineering and design* 66 (2003), pp. 413–417 (cited on page 21).

[17] Arkadi Kreter et al. 'Linear plasma device PSI-2 for plasma-material interaction studies'. In: *Fusion science and technology* 68.1 (2015), pp. 8–14 (cited on pages 21, 44).

[18] N Ohno et al. 'Static and dynamic behaviour of plasma detachment in the divertor simulator experiment NAGDIS-II'. In: *Nuclear Fusion* 41.8 (2001), p. 1055 (cited on pages 21, 44).

[19] Y Hirooka et al. 'A new plasma-surface interactions research facility: PISCES-B and first materials erosion experiments on bulk-boronized graphite'. In: *Journal of Vacuum Science & Technology A: Vacuum, Surfaces, and Films* 8.3 (1990), pp. 1790–1797 (cited on pages 21, 44).

[20] Cormac Corr et al. 'MAGPIE: A new linear plasma device for studying fusion relevant plasma-surface interactions'. In: *APS Annual Gaseous Electronics Meeting Abstracts*. 2012, DT2–006 (cited on pages 21, 44).

[21] G Granucci et al. 'The new linear plasma device GyM at IFP-CNR'. In: *36th EPS Conference on Plasma Physics*. 2009 (cited on pages 21, 44).

[22] Michele Sala et al. 'Simulations of Argon plasmas in the linear plasma device GyM with the SOLPS-ITER code'. In: *Plasma Physics and Controlled Fusion* 62.5 (2020), p. 055005 (cited on pages 21, 22, 45).

[23] B.D. Wirth et al. 'Fusion materials modeling: Challenges and opportunities'. In: *MRS Bulletin* 36.3 (2011), pp. 216–222. DOI: 10.1557/mrs.2011.37 (cited on page 24).

[24] BD Wirth et al. 'Fusion materials modeling: Challenges and opportunities'. In: *MRS bulletin* 36.3 (2011), pp. 216–222 (cited on page 25).

[25] Lewi Tonks and Irving Langmuir. 'A general theory of the plasma of an arc'. In: *Physical Review* 34 (1929), pp. 876–922 (cited on page 25).

[26] R. Chodura. 'Plasma Flow in the Sheath and the Presheath of a Scrape-Off Layer'. In: 1986 (cited on page 26).

[27] Juri Romazanov. *3D simulation of impurity transport in a fusion edge plasma using a massively parallel Monte-Carlo code*. FZJ-2019-01018. Plasmaphysik, 2018 (cited on pages 29, 39, 42, 43, 45).

[28] Heinrich Hora. 'D. R. Nicholson, Introduction to Plasma Theory, John Wiley & Sons, New York, 1983, XII, 292 pp.' In: *Laser and Particle Beams* 2 (1984), pp. 127–127 (cited on page 30).

[29] L. Boltzmann. In: *Weitere Studien über das Wärmegleichgewicht unter Gasmolekülen*. 1872 (cited on page 30).

[30] Chris N. Lashmore-Davies. 'Collisional Transport in Magnetized Plasmas, by Per Helander and Dieter J. Sigmar, Cambridge Monograph on Plasma Physics, Cambridge University Press (2002)'. In: *Journal of Plasma Physics* 70 (2004), pp. 501–502 (cited on page 31).

[31] E.M. LIFSHITZ and L.P. PITAEVSKI. 'Physical Kinetics'. In: *Course of Theoretical Physics*. Ed. by E.M. LIFSHITZ and L.P. PITAEVSKI. Vol. 10. Course of Theoretical Physics. Amsterdam: Pergamon, 1981. DOI: https://doi.org/10.1016/B978-0-08-026480-6.50007-2 (cited on page 31).

[32] R. Balescu. '5 - The classical transport theory'. In: *Classical Transport*. Ed. by R. Balescu. Transport Processes in Plasmas. Amsterdam: North-Holland, 1988, pp. 211–276. DOI: https://doi.org/10.1016/B978-0-444-87091-9.50009-9 (cited on page 31).

[33] S. I. Braginskii. 'Transport Processes in a Plasma'. In: *Reviews of Plasma Physics 1* (1965), p. 205 (cited on pages 33, 35).

[34] M. Baelmans. 'Code improvements and applications of a two-dimensional edge plasma model for toroidal fusion devices. PhD thesis. Katholieke Universiteit Leuven'. In: (1993) (cited on pages 33, 35).

[35] Bastiaan Johan Braams. 'Computational studies in tokamak equilibrium and transport'. In: (1986) (cited on page 35).

[36] S. Wiesen et al. 'The new SOLPS-ITER code package'. In: *Journal of Nuclear Materials* 463 (2015). PLASMA-SURFACE INTERACTIONS 21, pp. 480–484. DOI: https://doi.org/10.1016/j.jnucmat.2014.10.012 (cited on page 35).

[37] A.S. Kukushkin et al. *SOLPS-ITER User Manual* (cited on page 36).

[38] D. Reiter. *The EIRENE Code User Manual*. 1992 (cited on pages 36, 38, 57).

[39] X. Bonnin et al. 'Presentation of the New SOLPS-ITER Code Package for Tokamak Plasma Edge Modelling'. In: *Plasma and Fusion Research* 11 (2016). DOI: 10.1585/pfr.11.1403102 (cited on pages 36, 37).

[40] R. Marchand and M. Dumberry. 'CARRE: a quasi-orthogonal mesh generator for 2D edge plasma modelling'. In: *Computer Physics Communications* 96.2 (1996), pp. 232–246 (cited on page 36).

[41] *Atomic Data and Analysis Structure*. URL: http://www.adas.ac.uk/documentation.php/ (cited on page 37).

[42] Wolfgang Eckstein. 'Sputtering yields'. In: *Sputtering by particle bombardment* (2007), pp. 33–187 (cited on pages 40, 66, 82, 85, 86).

[43] Michael Warwick Thompson. 'II. The energy spectrum of ejected atoms during the high energy sputtering of gold'. In: *Philosophical Magazine* 18.152 (1968), pp. 377–414 (cited on page 41).

[44] Jay P Boris and Ramy A Shanny. *Proceedings: Fourth Conference on Numerical Simulation of Plasmas, November 2, 3, 1970*. Naval Research Laboratory, 1972 (cited on page 41).

[45] Hong Qin et al. 'Why is Boris algorithm so good?' In: *Physics of Plasmas* 20.8 (2013), p. 084503 (cited on page 41).

[46] John Wesson and David J Campbell. *Tokamaks*. Vol. 149. Oxford university press, 2011 (cited on page 41).

[47] AA Ware. 'Pinch effect for trapped particles in a tokamak'. In: *Physical Review Letters* 25.1 (1970), p. 15 (cited on page 41).

[48] M Miyamoto et al. 'Systematic investigation of the formation behavior of helium bubbles in tungsten'. In: *Journal of Nuclear Materials* 463 (2015), pp. 333–336 (cited on page 44).

[49] Kay Song et al. 'Temperature dependence of retarded recrystallisation in helium plasma-exposed tungsten'. In: *Nuclear Fusion* 59.9 (2019), p. 096031 (cited on page 44).

[50] Ryuichi Sakamoto et al. 'Surface morphology of tungsten exposed to helium plasma at temperatures below fuzz formation threshold 1073 K'. In: *Nuclear fusion* 57.1 (2016), p. 016040 (cited on page 44).

[51] Shuichi Takamura et al. 'Formation of nanostructured tungsten with arborescent shape due to helium plasma irradiation'. In: *Plasma and fusion research* 1 (2006), pp. 051–051 (cited on page 44).

[52] MJ Baldwin and RP Doerner. 'Helium induced nanoscopic morphology on tungsten under fusion relevant plasma conditions'. In: *Nuclear Fusion* 48.3 (2008), p. 035001 (cited on page 44).

[53] Shin Kajita et al. 'Sub-ms laser pulse irradiation on tungsten target damaged by exposure to helium plasma'. In: *Nuclear Fusion* 47.9 (2007), p. 1358 (cited on page 44).

[54] Jun Wang et al. 'Fuzz nanostructure and erosion on tungsten–vanadium alloys exposed to helium plasma in the STEP linear plasma device'. In: *Nuclear Fusion* 59.8 (2019), p. 086038 (cited on page 44).

[55] G De Temmerman, T Hirai, and RA Pitts. 'The influence of plasma-surface interaction on the performance of tungsten at the ITER divertor vertical targets'. In: *Plasma Physics and Controlled Fusion* 60.4 (2018), p. 044018 (cited on page 44).

[56] GM Wright et al. 'Tungsten nano-tendril growth in the Alcator C-Mod divertor'. In: *Nuclear Fusion* 52.4 (2012), p. 042003 (cited on page 44).

[57] Guang-Hong Lu et al. 'Development and optimization of STEP—a linear plasma device for plasma-material interaction studies'. In: *Fusion Science and Technology* 71.2 (2017), pp. 177–186 (cited on page 44).

[58] Yue Xu et al. 'Plasma-surface interaction experimental device: PSIEC and its first plasma exposure experiments on bulk tungsten and coatings'. In: *Fusion Engineering and Design* 164 (2021), p. 112198 (cited on page 44).

[59] Gabriele Alberti. 'Exposure of nanostructured tungsten coatings to helium-plasmas in the GyM linear device'. MA thesis. Milano: Politecncico di Milano, 2019 (cited on page 44).

[60] Michael Reinhart et al. 'Diffusion model of the impact of helium and argon impurities on deuterium retention in tungsten'. In: *Nuclear fusion* 59.4 (2019), p. 046004 (cited on page 44).

[61] Shin Kajita et al. 'Impact of arcing on carbon and tungsten: from the observations in JT-60U, LHD and NAGDIS-II'. In: *Nuclear Fusion* 53.5 (2013), p. 053013 (cited on page 44).

[62] DL Youchison et al. 'Plasma exposures of a high-conductivity graphitic foam for plasma facing components'. In: *Nuclear Materials and Energy* 17 (2018), pp. 123–128 (cited on page 44).

[63] A Eksaeva et al. 'ERO modeling of Cr sputtering in the linear plasma device PSI-2'. In: *Physica scripta* 2017.T170 (2017), p. 014051 (cited on page 45).

[64] J Romazanov et al. 'First ERO2. 0 modeling of Be erosion and non-local transport in JET ITER-like wall'. In: *Physica scripta* 2017.T170 (2017), p. 014018 (cited on page 45).

[65] PH Rebut, RJ Bickerton, and Brian Edgar Keen. 'The Joint European Torus: installation, first results and prospects'. In: *Nuclear fusion* 25.9 (1985), p. 1011 (cited on pages 45, 85).

[66] Gabriele Alberti et al. 'ERO2. 0 modelling of nanoscale surface morphology evolution'. In: *Nuclear Fusion* (2021) (cited on pages 45, 81).

[67] Alina Eksaeva et al. 'ERO2. 0 modelling of the effects of surface roughness on molybdenum erosion and redeposition in the PSI-2 linear plasma device'. In: *Physica Scripta* 2020.T171 (2020), p. 014057 (cited on page 45).

[68] A Eksaeva et al. 'Surface roughness effect on Mo physical sputtering and re-deposition in the linear plasma device PSI-2 predicted by ERO2. 0'. In: *Nuclear materials and energy* 19 (2019), pp. 13–18 (cited on page 45).

[69] M Sala et al. 'SOLPS-ITER simulations of the GyM linear plasma device'. In: *46th European Physical Society Conference on Plasma Physics, EPS 2019*. Vol. 43. European Physical Society (EPS). 2019, pp. 1–4 (cited on page 45).

[70] Michele Sala. 'Numerical and experimental studies of plasma-material interaction in linear plasma devices'. In: (2021) (cited on pages 45, 47).

[71] E Tonello et al. 'A point plasma model for linear plasma devices based on SOLPS-ITER equations: application to helium plasma'. In: *Nuclear Fusion* 61.6 (2021), p. 066036 (cited on page 45).

[72] CJ Beers et al. 'RF sheath induced sputtering on Proto-MPEX part 2: Impurity transport modeling and experimental comparison'. In: *Physics of Plasmas* 28.10 (2021), p. 103508 (cited on page 45).

[73] Juergen Rapp et al. 'Operational domain of Proto-MPEX'. In: *Fusion Engineering and Design* 136 (2018), pp. 712–716 (cited on page 45).

[74] 'Grant Agreement Number-633050-EUROfusion, Periodic Reporting, Period 01/2016 – 12/2016'. In: (2017) (cited on page 45).

[75] Juri Romazanov et al. 'First Monte-Carlo modelling of global beryllium migration in ITER using ERO2. 0'. In: *Contributions to Plasma Physics* 60.5-6 (2020), e201900149 (cited on pages 45, 46, 62, 65).

[76] Elena Tonello. 'Numerical investigation of nuclear fusion relevant plasmas in linear devices through the SOLPS-ITER code'. MA thesis. Milano: Politecncico di Milano, 2018 (cited on page 47).

[77] *MATLAB version 9.5 (R2018b)*. The Mathworks, Inc. Natick, Massachusetts, 2018 (cited on pages 62–64).

[78] I. Borodkina et al. 'An Analytical Expression for the Electric Field and Particle Tracing in Modelling of Be Erosion Experiments at the JET ITER-like Wall'. In: *Contributions to Plasma Physics* 56.6-8 (2016), pp. 640–645. DOI: https://doi.org/10.1002/ctpp.201610032 (cited on page 72).

[79] A. Widdowson et al. 'Overview of the JET ITER-like wall divertor'. In: *Nuclear Materials and Energy* 12 (2017). Proceedings of the 22nd International Conference on Plasma Surface Interactions 2016, 22nd PSI, pp. 499–505. DOI: https://doi.org/10.1016/j.nme.2016.12.008 (cited on page 85).

[80] G. Janeschitz et al. 'The ITER divertor concept'. In: *Journal of Nuclear Materials* 220-222 (1995). Plasma-Surface Interactions in Controlled Fusion Devices, pp. 73–88. DOI: https://doi.org/10.1016/0022-3115(94)00447-1 (cited on page 85).